ANALYSIS OF OPTIMAL MATCHING BETWEEN A DC MOTOR AND PHOTOVOLTAIC MODULES VIA DC-DC POWER CONVERTERS

by

Jesús David González-Llorente

A thesis submitted in partial fulfillment of the requirements for the degree of

MASTER OF SCIENCE

in

ELECTRICAL ENGINEERING

University of Puerto Rico
Mayagüez Campus

December, 2009

Approved by:

_____   _____
Gerson Beauchamp-Báez, Ph.D.   Date
Member, Graduate Committee

_____   _____
K. Venkatesan, Ph.D.   Date
Member, Graduate Committee

_____   _____
Eduardo I. Ortiz-Rivera, Ph.D.   Date
President, Graduate Committee

_____   _____
Karen R. Rios-Soto, Ph.D.   Date
Representative of Graduate Studies

_____   _____
Jaime Seguel, Ph.D.   Date
Associate Dean for Academic Affairs
College of Engineering

Abstract of Dissertation Presented to the Graduate School
of the University of Puerto Rico in Partial Fulfillment of the
Requirements for the Degree of Master of Science

**ANALYSIS OF OPTIMAL MATCHING BETWEEN A DC MOTOR
AND PHOTOVOLTAIC MODULES VIA DC-DC POWER
CONVERTERS**

By

Jesús David González-Llorente

December 2009

Chair: Eduardo Ortiz-Rivera, PhD
Major Department: Electrical and Computer Engineering

Due to the nonlinear behavior of the photovoltaic (PV) cells, dc-dc power converters are added for matching the load to the photovoltaic generators; thus, maximum power can be reached. In this thesis, mathematical models were used to examine the behavior of the off-grid photovoltaic system composed by: PV generator, dc-dc converter and dc motor. Different converter topologies (step-up, step-down and step-down/step-up) are compared, evaluating their feasibility to be used as interface to attain operation around the maximum power point (MPP). The analysis found the relationships between the optimal duty ratio and the maximum motor speed, which are used to select the simplest topology to meet the requirement as interface. Moreover, several maximum power point tracking (MPPT) methods including model-based MPPT methods and MPPT searching algorithms are implemented on a microcontroller and tested in real weather conditions. MPPT searching algorithms are recommended for real applications, such algorithms do not require tuning due to parameter variations by aging or dusty environment of the PV module and the fluctuation of the PV voltage has little effect on the motor speed.

ANALISIS DEL ACOPLE ÓPTIMO ENTRE MOTORES DE CORRIENTE CONTINUA Y MÓDULOS FOTOVOLTAICOS USANDO CONVERTIDORES DE POTENCIA

Por

Jesús David González-Llorente

Diciembre 2009

Consejero: Eduardo Ortiz-Rivera, PhD
Departamento: Ingeniería Eléctrica y Computadoras

Debido al comportamiento no lineal de los módulos fotovoltaicos, es necesario usar convertidores de corriente continua para extraer más potencia por medio del acople de carga. Se utilizan modelos matemáticos para estudiar el comportamiento de un sistema fotovoltaico compuesto de: generador fotovoltaico, convertidor de potencia y motor de corriente continua. Diferentes topologías de convertidores de potencia (reductora, elevadora y reductora-elevadora) son comparadas, evaluando la viabilidad de ser usadas como interfaces para obtener operación alrededor del punto de máxima potencia. Se deriva la relacion entre el ciclo útil del convertidor y la velocidad máxima del motor; la cual permite seleccionar la topología más simple que cumple los requerimientos como interface. Además, métodos basados en modelo y métodos de búsqueda para el seguimiento del punto de máxima potencia son implementados en un microcontrolador y probados bajo condiciones climáticas reales. Los métodos de búsqueda son recomendados para aplicaciones prácticas, ya que no requieren ajuste debido al cambio de parámetros de los módulos fotovoltaicos y del poco efecto de la variación del voltaje sobre la velocidad del motor.

A mis padres, Jesús y Yolanda

A mis hermanos, José Eduardo, Jairo Luis y María Paz

Acknowledgments

This thesis would not be possible without several contributions. I would like to thank my advisor, Dr. Eduardo I. Ortiz-Rivera for his direction, motivation, and for providing me with a pleasant working environment.

I am grateful to my thesis committee members Dr. K. Venkatesan and Dr. Gerson Beauchamp-Báez for their review and helpful criticisms. Special thanks to Dr. Gerson Beauchamp-Báez for letting me work under your supervision in the Control and Instrumentation Laboratory. I will always admire you as a professor and as an excellent person.

Also, I thank to Dr. Ramon Vazquez, Dean of the UPRM's College of Engineering, and all the members that belong to the Mathematical Modeling and Control of Renewable Energies for Advance Technology and Education ($M_{inds}{}^2$ CREATE) Research Team at UPRM for all the support they gave me.

Table of Contents

List of Tables

List of Figures

List of Abbreviations

ADC	Analog to Digital Converter.
ANN	Artificial Neural Networks.
DC	Direct Current.
DSP	Digital signal processor.
INC	Incremental Conductance.
ISR	Interrupt Service Routine.
LRCM	Linear Reoriented Coordinates Method.
MPP	Maximum Power Point.
MPPT	Maximum Power Point Tracker.
MSE	Mean Squared Error.
P&O	Perturbation and Observation.
PV	Photovoltaic.
PVM	Photovoltaic Module.
PWM	Pulse Width Modulation.
STC	Standard Test Conditions.
USART	Universal Synchronous/Asynchronous Receiver Transmitter.

List of Symbols

b	Characteristic constant of photovoltaic module.
C	Capacitance.
D	Duty ratio.
e	Induced electromotriz force.
E_i	Irradiance.
I	Current.
i_a	Armature current of DC motor.
I_{ap}	Approximated current at maximum power point.
i_L	Inductance current.
I_{mp}	Current of photovoltaic module at MPP at STC.
I_{MPP}	Current at maximum power point or optimal current.
I_{sc}	Short-circuit current of photovoltaic module at STC.
I_x	Short-circuit current of photovoltaic module.
K_e	Back electromotive force constant of DC motor.
K_v	Voltage factor in Linear Reoriented Coordinates Method.
L	Inductance.
L_a	Armature inductance of DC motor.
M_v	Voltage factor in fractional open-circuit voltage.
M_c	Current factor in fractional short-circuit current.
P_{max}	Maximum power of photovoltaic module at STC.
P_{MPP}	Maximum power of photovoltaic module.
P_{PVM}	Output power of the photovoltaic module.
P_{ap}	Approximated maximum power of photovoltaic module.
R_a	Armature resistance of DC motor.
T	Temperature.
T_S	Sampling time.
u_{av}	Averaged control input.
$u(t_k)$	Controller output.
$u(t_{k-1})$	Controller output in the previous instant.
V	Voltage.
V_a	Armature voltage of DC motor.
V_{ap}	Approximated voltage at maximum power point.
v_C	Capacitor voltage.
V_{mp}	Voltage of photovoltaic module at MPP at STC.
V_{MPP}	Voltage at maximum power point or optimal voltage.

V_{oc} Open-circuit voltage of photovoltaic module at STC.

V_x Open-circuit voltage of photovoltaic module.

η_{MP} Tracking efficiency of the MPPT method.

ω_m Rotational speed of DC motor.

Chapter 1

Introduction

There are many applications today in which photovoltaic (PV) modules can be used, in particular small off-grid loads, such as basic lighting, refrigeration, telecommunications and water pumping [1]. In some of these cases, a Direct Current (DC) motor is connected to a PV module (PVM) as load [2]; hence, these PV systems must be studied to improve their efficiency and to increase their growth.

The power delivered by a PVM is a function of environment conditions, as well as of the load the PVM is supplying [2]. For most of the DC motors directly connected to a PVM, the operating point is very far from the maximum power point (MPP) of the PVM [3]; the operating point is given by intersection of PV and DC motor I-V curves [2–4].

In order to improve the performance, the equilibrium operating point must be closer to MPP of PVM via matching of DC motor to PVM. The matching could be reached in two ways: First, without interfacing circuit, selecting carefully a DC motor according to motor I-V curve, mechanical load characteristics and PVM parameters [5–7]. Second, by including an electronic control device, known as maximum power point tracker (MPPT), which continuously matches the output characteristics of the PVM to the input characteristics of the motor [3, 4, 8, 9].

This research only addresses the second way, which uses an interfacing circuit in order to match photovoltaic modules to a DC motor. In addition, since the batteries have a short lifetime and their use increases the cost of renewable energy the system

studied has no a battery storage, thus the interfacing circuit only connects the PV module to the motor.

The interfacing circuit consists of DC to DC (DC-DC) power converters because they can vary the current coming from the PV array [10]. Step-down and step-up topologies such as nonisolated Buck and Boost DC-DC converters, are widely used as photovoltaic interfaces due to their advantages of simplicity and efficiency [11].

The power converter duty ratio must be adjusted to a constant value until optimal matching is achieved [12, 13]. Since the PVM response changes continuously with the environmental conditions, the duty ratio adjustment must be carried out automatically; consequently, different MPPT methods to control the duty ratio are also analyzed.

1.1   Motivation

The purpose is to develop a comparative study about the performance of the off-grid photovoltaic system. This system consists of a direct current motor fed from a photovoltaic generator. In addition, application of dc-dc power converter as interface to load matching will be studied; maximum power point tracking algorithm will also be studied.

The following points show the importance of this work:

- By stimulating the growth of photovoltaic projects, there is are a way to increase the generation capacity and to reduce greenhouse gas emissions; moreover, they can be utilized in remote areas where the utility grid is not available.
- The evaluation of the feasibility of different kinds of dc-dc power converters as interface between a photovoltaic generator and a direct current motor.
- The analysis of maximum power point tracking algorithms, which are required for maximum photovoltaic energy utilization according to the weather condition or type of connected load.

- The validation of models by means of software simulation, implementation, experimentation and testing over an actual system.

1.2   Objectives

To study step-down, step-up and step-down/step-up DC-DC converter topologies as interface between a photovoltaic generator and a direct current motor, considering photovoltaic maximum power extraction.

The specific objectives of this work include:

- To identify and to implement models that represent the behavior of both the photovoltaic generator and direct current motor.

- To evaluate the effectiveness of step-down, step-up and step-down/step-up topologies in matching a direct current motor to a photovoltaic generator.

- To consider several maximum power point tracking methods for photovoltaic generator that supplies a direct current motor and selecting the method that is more practical.

1.3   Summary of Contributions

- For several topologies, including step-down, step-up and step-down/step-up, a relationship between optimal duty ratio and maximum power has been derived, as well as the relationship between optimal duty ratio and motor speed.

- Determination of necessary conditions for matching DC motor to the PVM, attaining operation around the maximum power point using dc-dc converter as interface.

- The Linear Reoriented Coordinates Method (LRCM) is implemented and experimentally validated as a maximum power point tracking method.

- A low-cost and easily implementable MPPT is developed in order to extract the maximum power of a photovoltaic module feeding a DC motor.

1.4 Thesis Outline

This thesis is divided into six chapters. The first chapter has briefly introduced the main problem on most of the photovoltaic systems. The motivations and the objectives of this thesis have also been discussed. Below, a brief summary of the following chapters is presented.

Chapter 2 This chapter gives an overview of the photovoltaic modules, the DC-DC converters and the DC motor with their mathematical models. A brief explanation of the problem of tracking the maximum power point is presented, as well as a classification of different methods. Finally, previous publications that studied a DC motor fed from a photovoltaic generator through power converters are summarized.

Chapter 3 The photovoltaic system studied is shown; the specifications of the DC motor and photovoltaic modules are listed, and the problem of the motor directly connected to the photovoltaic generator is discussed. The chapter also includes the derivations of the input resistance of the Buck-Boost converter and the optimal duty ratios for each one of the basic topologies.

Chapter 4 The design and implementation of the maximum power point tracking (MPPT) methods are described. The circuits, software routines and configurations developed for operations of the MPPT methods are explained. These methods are: Linear Reoriented Coordinates Method (LRCM), Perturbation and Observation (P&O), Incremental Conductance (INC) and Positive feedback of DC motor speed.

Chapter 5 The relationships: optimal duty ratio vs. maximum power and optimal duty ratio vs motor-speed are used to compare the power converters as interface, making topology selection easier. The MPPT methods are tested and verified, showing simulations and experimental results.

Chapter 6 Finally, conclusions on the obtained results are presented; this chapter also includes suggestions for future work.

Chapter 2

Literature Review

This chapter introduces the components of the photovoltaic system analyzed, which consists of a photovoltaic module (PVM), a Direct-Current (DC) motor, a DC-DC power converter and a maximum-power controller. The basic concepts and the mathematical models of each component are presented.

Furthermore, the chapter gives an overview of some publications where a DC motor is fed by a photovoltaic generator through a DC-DC power converter. This review shows the topologies used and the different methods to extract the maximum power.

2.1 The Photovoltaic Module

The elementary PV device is the PV cell, which is basically a semiconductor p-n junction that converts sunlight into electricity. A set of connected cells in a serial, or in a parallel manner, form a panel or module. A PV array may be either a panel or a set of panels connected in series or parallel [14, 15].

Some of the models are based on the physics of semiconductors and require several parameters such as the temperature coefficients, photon current, series/shunt resistance of the device, among others [15, 16]. These models can be impractical and too complex for tasks such as power flow, load matching or simulation of power electronic conversion systems [14, 16].

However, all the PVM datasheets give information about electrical characteristics of PV devices in Standard Test Conditions (STC), i.e. irradiance of $1000W/m^2$

and temperature of 25°C. The main parameters provided at STC are: the nominal open-circuit voltage (V_{oc}), the nominal short-circuit current (I_{sc}), the voltage at MPP (V_{mp}), the current at MPP (I_{mp}), the temperature coefficient of I_{sc} (TC_i), the temperature coefficient of V_{oc} (TC_v) and the maximum power (P_{max}).

Instead of using equations from the theory of semiconductors, the analytical model for a PVM proposed by Ortiz-Rivera in [17] will be used. This model is based on the electrical characteristics provided by the manufacturer datasheet and describes the relationship of Current-Voltage ($I - V$) in any practical PV array as is shown in (2.1).

$$I(V) = \frac{p \cdot I_x}{1 - \exp\left(\frac{-1}{b}\right)} \left[1 - \exp\left(\frac{V}{b \cdot s \cdot V_x} - \frac{1}{b}\right)\right] \tag{2.1}$$

Where, I_x and V_x are the short-circuit current and the open-circuit voltage at any given irradiance level (E_i) and temperature (T), respectively; s is the number of serial-connected modules with the same electrical characteristics; p the number of parallel-connected module with the same electrical characteristics; b is the PVM characteristic constant, which can be calculated using an algorithm based on the Fixed Point Theorem. The algorithm is shown in (2.2), where ξ is the maximum permitted error.

$$\text{while} |b_{n+1} - b_n| > \xi$$
$$b_{n+1} = \frac{V_{mp} - V_{oc}}{V_{oc} \cdot \ln\left[1 - \frac{I_{mp}}{I_{sc}} \cdot \left(1 - \exp\frac{1}{b_n}\right)\right]} \tag{2.2}$$

The Equation (2.1) represents the $I - V$ characteristic when the open-circuit voltage and the short-circuit current are known. Then, the model is completed with the Equations (2.3) and (2.4), which describe the behavior of I_x and V_x considering the irradiance (E_i) and the temperature (T).

$$I_x = \frac{Ei}{E_{in}} \left[I_{sc} + TC_i(T - T_N)\right] \tag{2.3}$$

$$V_x = \frac{E_i}{E_{in}} TC_v(T - T_N) + V_{max} - (V_{max} - V_{min}) \exp \frac{E_i}{E_{in}} \ln \frac{V_{max} - V_{min}}{V_{max} - V_{oc}} \tag{2.4}$$

where, E_{in} and T_N are the irradiance and temperature at STC, V_{max} is the open-circuit voltage at $25°C$ and more than $1200W/m^2$ (Usually, V_{max} is close to $1.03V_{oc}$), V_{min} is the open-circuit voltage at $25°C$ and less than $200W/m^2$ (Usually, V_{min} is close to $0.85V_{oc}$).

2.2   Maximum Power Point Tracking

Figure 2–1 shows the characteristic curves for a PVM under a given temperature and irradiance. This figure also shows that there is an unique point for the maximum power(P_{MPP}). This point is known as the maximum power point (MPP) and consists of the optimal voltage (V_{MPP}) and the optimal current (I_{MPP}) [10].

Maximum Power Point Tracking (MPPT) is an essential part of any photo-voltaic system, which ensures the optimal use of the available solar energy [10, 18, 19]. The problem considered by MPPT techniques is to find the voltage or current at which a PVM should operate to extract the maximum power output, as well as, to adjust a photovoltaic interface so that the operating characteristic of the load and the PVM match at the maximum power point [10, 20].

Many MPPT methods have been developed and implemented, which vary in complexity, sensors required, convergence speed, cost, range of effectiveness, implementation hardware, among other aspects [10]; however, most of these methods can be classified into three main categories: model-based algorithms, training based algorithms and searching algorithms [21].

2.2.1   Model-based MPPT algorithms

These methods refer to those using any mathematical model or look up table model when calculating the maximum power point(MPP); as well as, methods that approximate the MPP according to the characteristics of the PV array. Among these methods we have: Linear Reoriented Coordinates Method (LRCM) [17, 22, 23], Fractional Open-circuit voltage and Fractional Short-circuit current [24].
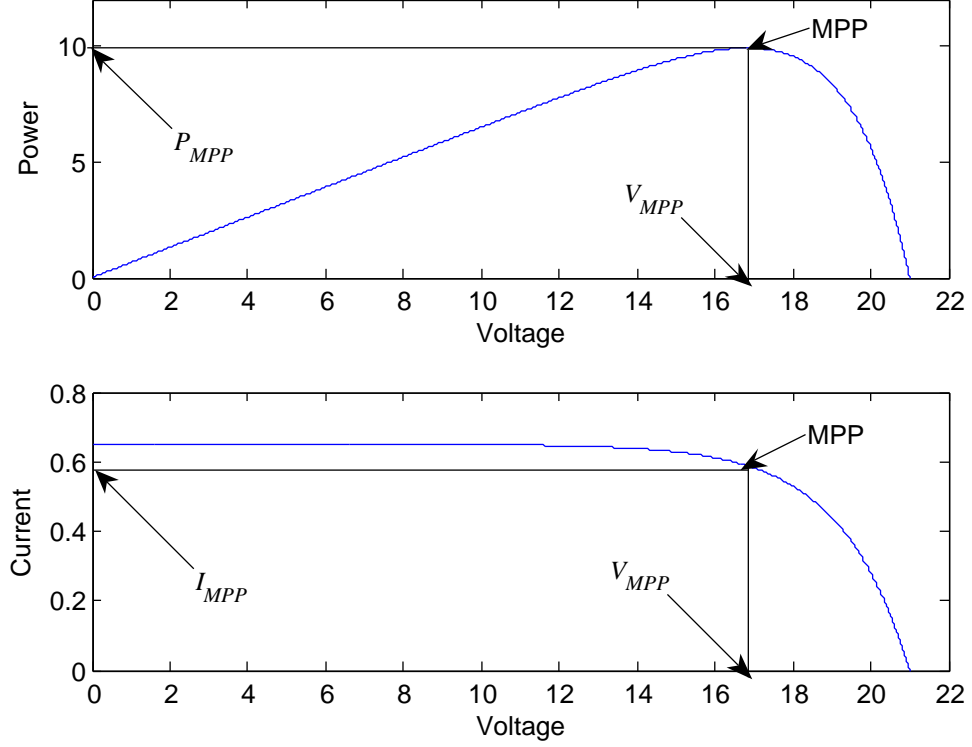
Figure 2–1: Characteristic Curves of PVM

The Linear Reoriented Coordinates Method proposed in [17] obtains the approximations of I_{MPP}, V_{MPP} and P_{MPP}. The equations of the approximated optimal voltage (V_{ap}) and the approximated optimal current (I_{ap}) are given by (2.5) and (2.6). Then, the approximated maximum power (P_{ap}) is obtained by multiplying V_{ap} and I_{ap} as is demonstrated in (2.7).

$$V_{ap} = V_x + b \cdot V_x \ln \left(b - b \cdot \exp \left(-\frac{1}{b} \right) \right) \leq V_{MPP} \tag{2.5}$$

$$I_{ap} = I_x \frac{1 - b + b \cdot \exp \left(-\frac{1}{b} \right)}{1 - \exp \left(-\frac{1}{b} \right)} \tag{2.6}$$

$$P_{ap} = I_x \cdot V_x \frac{\left[1 - b + b \cdot \exp \left(-\frac{1}{b} \right) \right] \left[1 + b \cdot \ln \left(b - b \cdot \exp \left(-\frac{1}{b} \right) \right) \right]}{1 - \exp \left(-\frac{1}{b} \right)} \tag{2.7}$$

Fractional open-circuit voltage method proposes that there is a linear relationship between the optimal voltage (V_{MPP}) and V_x, which is known as voltage factor (M_v) [24]. This relationship is given by a constant of proportionality, which is computed empirically and has been reported to be between 0.71 and 0.78 [10].

Likewise, the Fractional short-circuit current determines that there is a linear dependence between the optimal current (I_{MPP}) and I_x; this dependence is given by the constant of proportionality called current factor (M_c) [24, 25], which is generally found to be between 0.78 and 0.92 [10].

Both in the Fractional open-circuit voltage and in the Fractional short-circuit current, the constant of proportionality has to be determined empirically according to the PVM in use. Then, the approximation of the maximum power point is given through Equations (2.8) and (2.9).

$$V_{MPP} \approx M_V \cdot V_x \qquad (2.8)$$

$$I_{MPP} \approx M_c \cdot I_x \qquad (2.9)$$

When the model-based MPPT methods find the optimal voltage or the optimal current, a voltage or current feedback control loop is used to force the PVM to operate at the maximum power point.

2.2.2   Training-based MPPT algorithms

The Training-based MPPT algorithms are those based on artificial intelligence such as fuzzy logic and artificial neural networks (ANN) [21]. These techniques have the advantages of handling nonlinearity and the ability to learn.

The inputs to a MPPT fuzzy logic controller are usually an error and a change in error, generally this error is given by dP/dV. The output of the fuzzy logic controller is typically a change in the duty ratio of the power converter, and is looked up in a rule based table [10].

The ANN input variables can be PVM parameters like V_{oc} and I_{sc}, as well as atmospheric data like irradiance and temperature. The output is usually the duty ratio of the power converter to force the PVM operation at, or close to the MPP [10, 26].

The artificial intelligence techniques have several disadvantages for their application such as: necessity of a large memory microcontrollers/DSPs for their implementation, thus increasing the cost. The effectiveness of Fuzzy Logic controller depends a lot on knowledge of the control engineer in choosing the right error computation and the rule based table; the ANN has to be specifically trained for the PVM in use [10, 21].

2.2.3 Searching MPPT algorithms

These algorithms are based on measurements of the PVM output voltage and current. They use the measurements to calculate the PVM power and determine whether to increase or decrease a control parameter; this parameter can be a reference signal for a controller or can be the duty ratio of the power converter [21].

In addition to the ease of implementation, the searching MPPT methods have the advantage that they do not require previous knowledge of the PVM characteristics. However, the performance of the algorithm may be affected by the DC link capacitor, the switching frequency and the step size used in changing the control variable [21].

The searching MPPT algorithms include the Perturbation and Observation (P&O) method and the Incremental Conductance (INC) method. Among MPPT algorithms, the P&O is the most popular technique due to its simplicity [27]. However, the INC method offers better performance during system transients [21, 28].

Perturbation and Observation

The perturbation and observation (P&O) method is based on the Power-Voltage characteristic of the PVM. If the operating voltage of PVM is perturbed in a given direction and the power drawn of PVM increases, the subsequent perturbation must be kept in the same direction. Otherwise, if the power drawn of PVM decreases, the perturbation must be reversed [29].

Incremental Conductance

The INC method is also based on the observation of the Power-Voltage charac-
teristic of the PVM. The derivative of the power with respect to the voltage (dP/dV)
is zero at MPP; furthermore, to the left of MPP the power is increasing with the
voltage, whereas to the right of MPP the power is decreasing with the voltage [30].
These relationships can be written in terms of current and voltage as:

$$\frac{dP}{dV} = \frac{d(IV)}{dV} = I + V\frac{dI}{dV} \approx I + V\frac{\Delta I}{\Delta V} \tag{2.10}$$

Therefore, the direction of the control variable can be known by comparing the
instantaneous conductance (I/V) to the incremental conductance ($\Delta I/\Delta V$) as is
described in (2.11).

$$\begin{cases} \frac{\Delta I}{\Delta V} = -\frac{I}{V} & \text{at the MPP} \\[2mm] \frac{\Delta I}{\Delta V} > -\frac{I}{V} & \text{to the left of the MPP} \\[2mm] \frac{\Delta I}{\Delta V} < -\frac{I}{V} & \text{to the right of the MPP} \end{cases} \tag{2.11}$$

2.3   DC-DC Power Converter

The DC-DC converters are commonly used in applications requiring regulated
DC power as in DC motor drive applications [31, 32]. However, in this work the
DC-DC converters are used as interface between photovoltaic modules (PVM) and
a DC motor, matching the load to the PVM.

The most commonly used DC-DC power converters correspond to the SISO
(Single-Input Single-Output) second order converters. These are: Step-down (Buck)
converter, Step-up (Boost) converter and Step-down/step-up (Buck-Boost) con-
verter [33]. In order to maintain generality, these are the only topologies considered
in this study.

The DC-DC converters are generally controlled using a switching concept; specially, Pulse Width Modulation (PWM), which involves a constant switching frequency (switching period, T_s) and an adjustable on-time, t_{on}. The ratio between t_{on} and T_s is known as duty ratio D, i.e. $D = \frac{t_{on}}{T_s}$ [31].

The methodology for the derivation of the models of the basic converters have been widely discussed in [32–34]. However, an overview of the average model converter in continuous conduction mode will be presented below. Analysis in discontinuous conduction mode as well as output voltage ripple can be found in [31, 32, 34, 35]

2.3.1 Step-down Converter

The main applications of step-down (Buck) converters are voltage regulation and DC motor speed control. The basic circuit is shown in Figure 2–2. The diode avoids that the switch absorbs or dissipates the inductive energy; the inductor and the capacitor constitute a filter that diminishes the output voltage fluctuations [32].

In continuous-conduction mode, the averaged-output-voltage of the Buck converter is the product of the duty ratio and the DC input voltage (i.e. $D = \frac{V_o}{V_i} = \frac{I_i}{I_o}$), their average model is represented by Equation (2.12), where, u_{av} is the average control input or duty ratio that takes values in the interval [0,1] [32, 33].
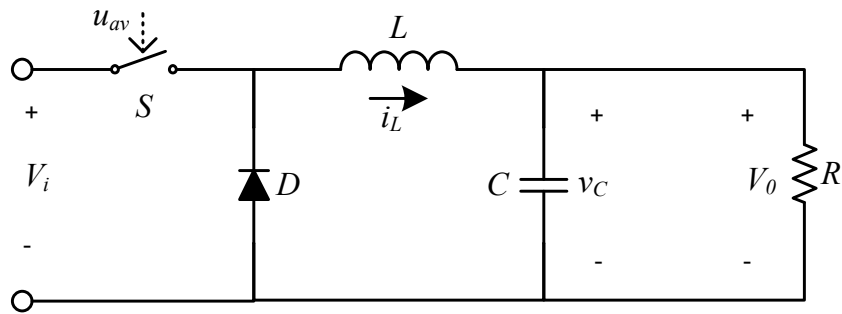
Figure 2–2: Basic circuit of step-down converter

$$L\frac{di_L}{dt} = -v_C + u_{av}V_i$$

$$C\frac{dv_C}{dt} = i_L - \frac{v_C}{R} \tag{2.12}$$

2.3.2 Step-up converter

The step-up (boost) converters are often used in regulated DC power supplies and in regenerative braking of DC motors; Figure 2–3 shows a basic circuit, where the capacitor is large to keep a constant output voltage, and the inductor also provides energy when the switch is open, boosting the voltage across the load [31, 32].

In continuous-conduction mode, the voltage ratio for a Boost converter is equivalent to the ratio of the switching period to the off-time of the switch t_{off}, as is shown in Equation (2.13). The dynamics of the converter is described by (2.14)
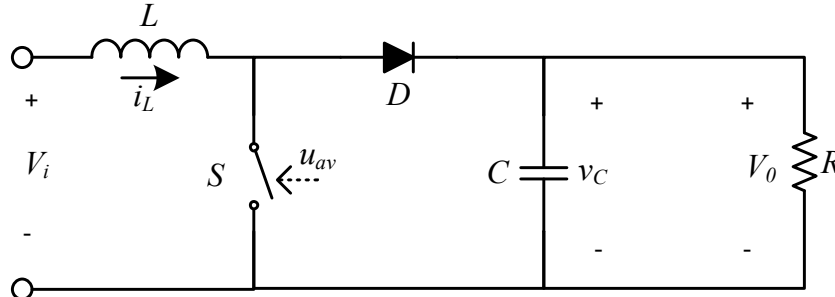
Figure 2–3: Basic circuit of step-up converter

$$\frac{V_o}{V_i} = \frac{T_s}{t_{\text{off}}} = \frac{1}{1-D} \tag{2.13}$$

$$L\frac{di_L}{dt} = -(1 - u_{av})v_C + V_i$$

$$C\frac{dv_C}{dt} = (1 - u_{av})i_L - \frac{v_C}{R} \tag{2.14}$$

2.3.3 Step-down/Step-up Converter

The output voltage of the step-down/step-up (Buck-Boost) converter can be higher or lower than the input voltage; moreover, the output voltage is negative with

respect to the input voltage. The main application of the Buck-Boost converter is in regulated DC power supplies [31, 32].

The circuit diagram of a Buck-Boost converter (Figure 2–4) shows that this converter can be obtained from the Buck converter by interchanging the diode and the inductor. When the switch is closed, the input provides energy to the inductor and when the switch is open, the energy stored in the inductor is transfered to the output [32]. In steady state, the output-to-input voltage conversion ratio is equal to the product of the conversion ratios of the Boost and the Buck converters, as shown in Equation (2.15).

$$\frac{V_o}{V_i} = -\frac{D}{1-D} \tag{2.15}$$
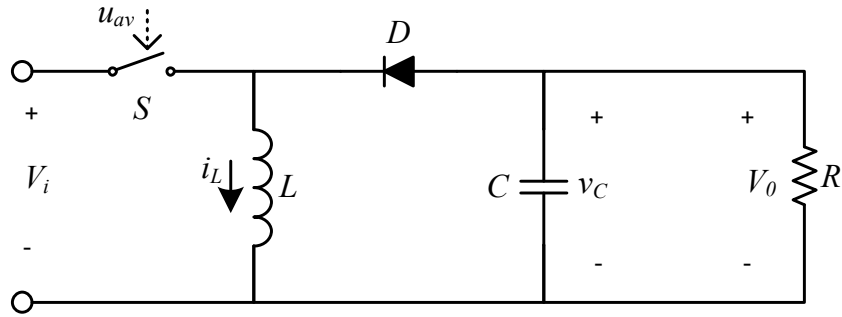
Figure 2–4: Basic circuit of step-down/step-up converter

The differential equations that describe the operation of the Buck-Boost converter in continuous conduction mode are (2.16) and (2.17). These basic averaged equations describe the variations of the inductor current and the capacitor voltage [34].

$$L\frac{di_L}{dt} = (1 - u_{av})v_C + u_{av} \cdot V_i \tag{2.16}$$

$$C\frac{dv_C}{dt} = -(1 - u_{av})i_L - \frac{v_C}{R} \tag{2.17}$$

2.4 Direct Current Motor

The Direct Current (DC) motors convert electrical power into mechanical power. These motors are reliable, durable, inexpensive and use low operation voltages [36]. The description of the operation theory can be found in reference [37]; however, a brief description of the DC motor modeling is presented below.

The equivalent circuit of a DC motor armature is shown in Figure 2–5. The armature winding has a resistance R_a, a self-inductance L_a, and an induced voltage e. The induced voltage is also known as induced electromotriz force (emf), and it is proportional to the rotor speed ω_m and the constant of proportionality K_e (or back emf constant). Then, the electrical side of the DC motor can be described by

$$V_a = R_a \cdot i_a + L_a \frac{di_a}{dt} + K_e \cdot \omega_m \tag{2.18}$$
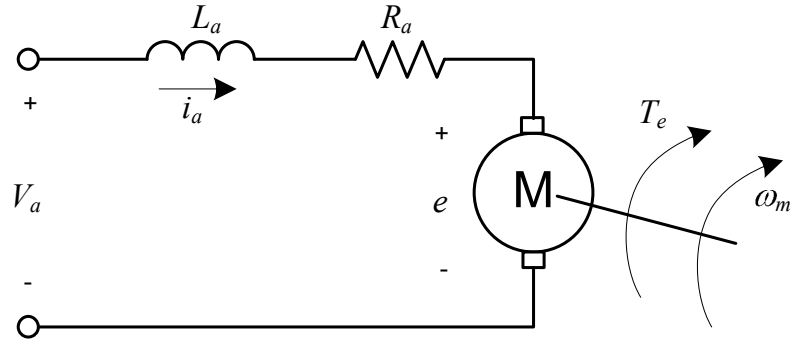
Figure 2–5: Equivalent circuit of a DC motor

The load is modeled as a moment of inertia J, with a viscous friction constant B_m. The sum of the torque gives the torque balance equation

$$T_e = J \frac{d\omega_m}{dt} + B_m \cdot \omega_m + T_L \tag{2.19}$$

where T_e and T_L are the electromagnetic torque and the load torque, respectively. The electromagnetic torque is equal to the product of the torque constant (K_T) and the armature current (i.e. $T_e = K_T i_a$); the torque constant is equal to the back emf constant (K_e) for a constant-flux machine [37].

2.5 Previous work

Step-up DC-DC power converters are used as circuit interface between a PVM and a DC motor in [3, 4, 38, 39]. According to Alghuwainem in [3], the current at maximum power (I_{MP}) is always approximately 84.9% of short circuit current (I_{sc}) at any irradiance level; hereby, it shows that the optimal duty ratio is independent of irradiance, so the step-up converter is driven with constant duty ratio. While in [4], the duty ratio of step-up converter is controlled using a current-locked feedback loop with integral action. The system studied by Alghuwainem is shown in Figure 2–6.

Figure 2–7 shows the scheme analyzed by Hussein *et al.* [38], where the effect of matching the field and/or armature windings on the separately excited DC motor is evaluated. As a result this shows the importance of matching the field circuit for better efficiency.

The system proposed by Akbaba in [39] consists of a PV generator, a step-up DC-DC converter with two filter capacitors at the two ends, and a permanent magnet (PM) DC motor. This is shown in Figure 2–8. In order to maximize energy utilization, a relationship between optimal duty cycle and the solar radiation level were established. This relationship was obtained by a simulation using curve fitting techniques. The results are only shown for 100% solar radiation and these are based on simulation.
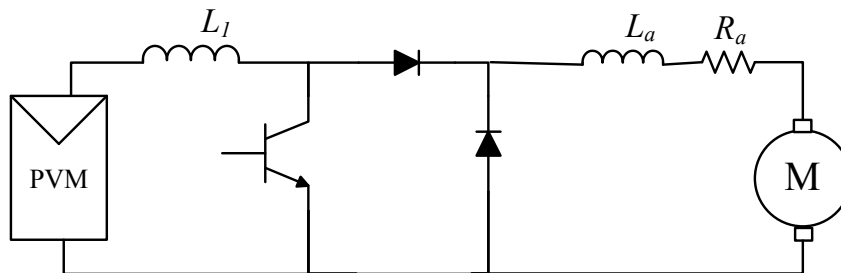
Figure 2–6: System analyzed by Alghuwainem
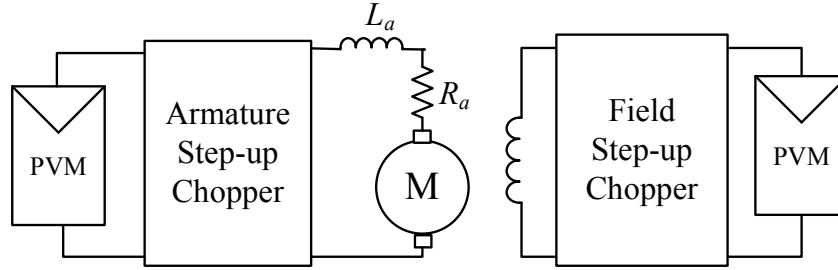
Figure 2–7: System analyzed by Hussein *et al.*
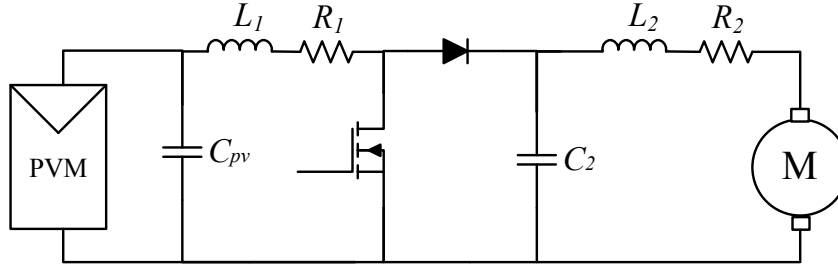
Figure 2–8: System analyzed by Akbaba

In [40–44] step-down DC-DC power converters are used as circuit interface for matching a PVM with a DC motor. In addition, the research [43, 44] asserts that they could match a PVM with a DC motor as well as regulating its speed.

The system analyzed by Shokrolla is shown in Figure 2–9. This system is composed of a photovoltaic array, an input low-pass LC filter, a DC-DC step-down chopper and a separately excited motor driven pump load. The control strategy for ensuring maximum power used by the pump load is given by two proportional-integral (PI) controllers [40]. The master loop operates with the optimal-voltage error, while the supplementary loop operates with the maximum-power error; however, it is not shown how they calculate the voltage and power references. In this work operation at maximum power is achieved for two irradiance levels, 20% and 30%, and for a constant load torque.

The scheme proposed by Venkatesan and Chéverez in [41] has a photovoltaic generator, a separately excited DC motor and a Buck-based converter that is known as chopper. This scheme is shown in Figure 2–10. In order to track the maximum power, a law based on positive feedback of speed control is derived. Their experimental results show maximum power tracking at irradiance values around 30%.
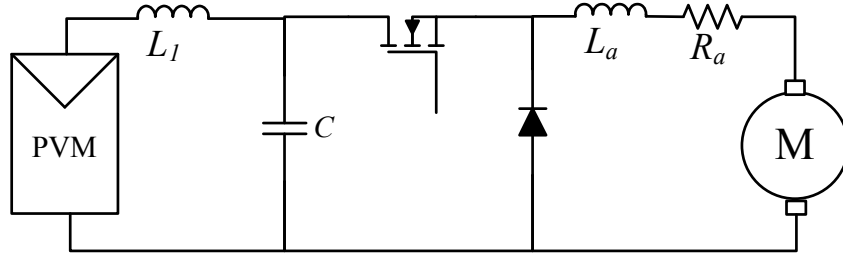
Figure 2–9: System analyzed by Shokrolla *et al.*
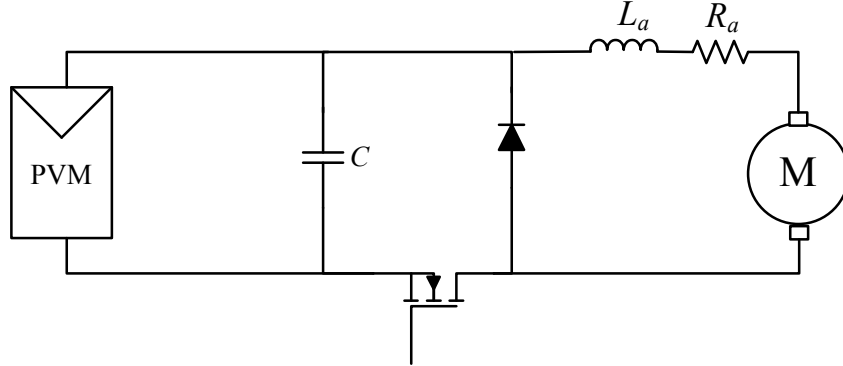
Figure 2–10: System analyzed by Venkatesan and Chéverez

Tariq and Asghar proposed the scheme shown in Figure 2–11. This one consists of a photovoltaic panel, a step-down dc-dc converter and a separately excited DC motor. To operate the panel at MPP, the actual PV array voltage was compared with the reference voltage. The obtained error is then processed by a difference amplifier and an integrator. The reference voltage is a fraction of open-circuit voltage. This is measured from an unloaded pilot PV panel installed along the main PV panel. Their simulation results show that the motor draws maximum power from the PV panel for both centrifugal load (i.e. the load torque $T_L = K_L \omega_m^{1.8}$) and the constant-torque type loads [42].

The proposed system by Sharaf and Yang in [43] is shown in Figure 2–12. This system is composed of a PV array, a blocking diode, an input filter, a four-quadrant PWM converter and a permanent magnet DC motor. In order to ensure reference speed tracking with minimum motor inrush current and maximum photovoltaic energy utilization, a dynamic tri-loop error driven control system was developed. Their digital simulation results show the dynamic response of motor tracking a trapezoidal reference speed trajectory.
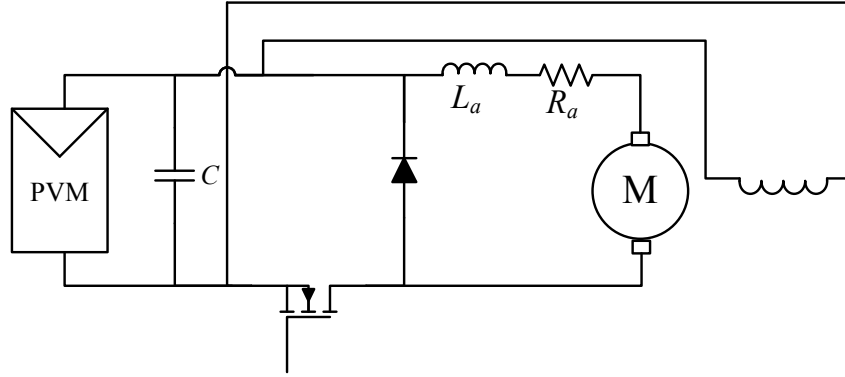
Figure 2–11: System analyzed by Tariq and Asghar
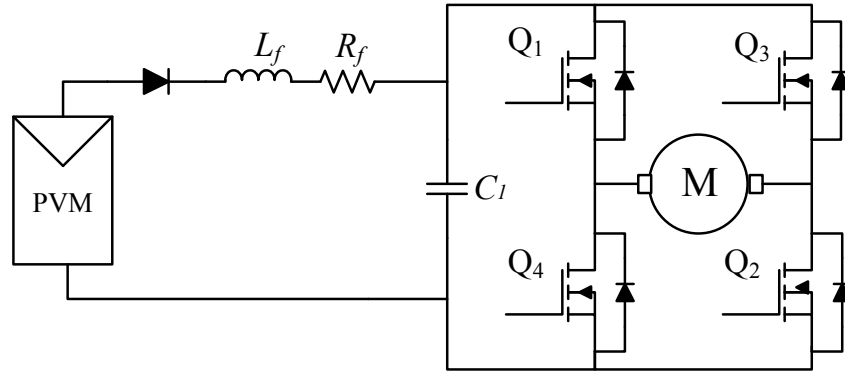
Figure 2–12: System analyzed by Sharaf and Yang

A Buck-Boost power converter was employed as an interface between PVM and DC motor in [26], where an adaptive neural network controller was used to control the speed; however, no results are shown for operation on MPP. In [45] a SEPIC converter has been studied as an interface between a PVM and a battery bus, but this did not consider a DC motor as a load.

In [20], Buck and Boost topologies were compared by way of their dynamic models; these topologies are used as power interface to a battery. There are no studies that compare these power converter topologies interfacing a PVM and a DC motor.

This present research will show a mathematical analysis of a PVM supplying a DC motor through different kinds of DC-DC power converters. Then, it presents a comparative study to evaluate which power converter is more adequate to matching the PVM to the DC motor. Finally, algorithms for controlling power will also be analyzed.

Table 2–1: Summary of previous work with Step-up Converter

Ref	DC Motor	MPPT	Observation
[4]	N/A	Integral controller. Optimal current is a fraction of the short-circuit current	No experimental results are shown
[38]	Separately excited	N/A	Shows the importance of controlling the field.
[39]	Permanent magnet	Relationship between the duty ratio and the irradiance	Variations of temperature are not considered, Irradiance measures are required.

Table 2–2: Summary of previous work with Step-down Converter

Ref	DC Motor	MPPT	Observation
[40]	Separately excited, constant field; constant load torque	Two PI controller for voltage error and power error. The calculation of reference is not shown	Results are only for irradiance: 20% and 30%
[41]	Separately excited, constant field; constant load torque and pump load	Control law relating duty ratio with motor speed	Results are only for irradiance lower than 30%. Temperature is constant.
[42]	Separately excited, shunt; constant load torque and pump load	Optimal voltage is a fraction of open-circuit voltage; error amplifier with integrator	Use a pilot PV panel in order to obatin the open-circuit voltage.
[43]	Permanent magnet	Tri-loop considering speed, motor current and power	Operation around MPP is not shown, but trapezoidal speed reference trajectory.

Chapter 3

Method of Analysis

The photovoltaic system studied is composed of a photovoltaic generator, a direct current motor, a DC-DC power converter and a control subsystem; a block diagram of the system is shown in figure 3–1. This chapter describes the characteristics and actual parameters of the DC motor and the photovoltaic module (PVM) that are used. The problem of direct coupling between the PVM and the DC motor is discussed, showing their current-voltage $(I - V)$ characteristics and the location of the operating point. This chapter also shows how a DC-DC converter can vary its incoming current, through the derivation of an input resistance expression. Finally, the chapter shows an analysis of the power converter as interface between the PVM and the DC motor; this analysis considers step-down, step-up and step-down/step-up topologies, deducing an optimal duty ratio expression for each one of the topologies.
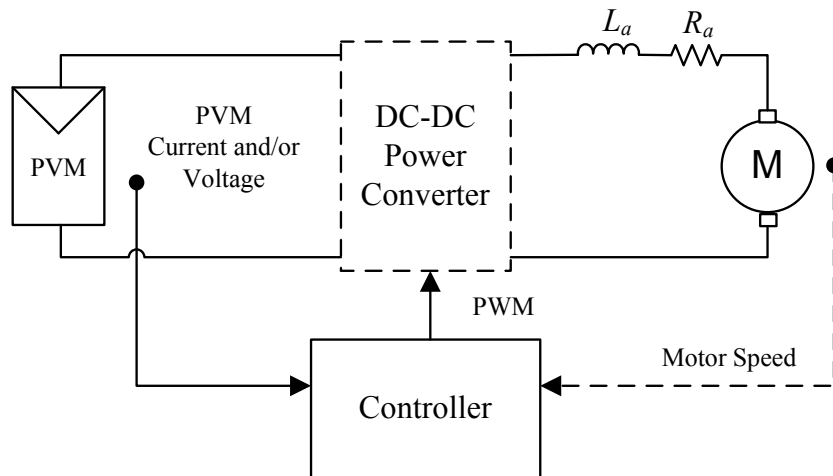
Figure 3–1: Block diagram of the considered system

3.1 Specifications and Requirements

The DC motor parameters and the PVM characteristics are shown below. Appendix A shows information of the PVM such as simulated characteristic curves. Appendix B presents the DC motor specifications in detail and the validation of the DC motor model, showing the current-voltages curves, the power-voltage curves and the torque-speed characteristic.

3.1.1 Specifications of the Direct Current motor

The separately excited DC motor used with a constant field $V_f = 50V$ has the parameter listed in Table 3–1. These parameters are presented in [41] and are validated by comparing real data with simulation data as is described in Appendix B.

The motor is loaded through an eddy current brake, where the position of the braking magnet defines the load torque (T_L) applied (Figure 3–2). In order to determine the load torque characteristics, variations of armature voltage, armature current and motor speed are registered for different positions of the eddy current brake, which allow the torque computation.
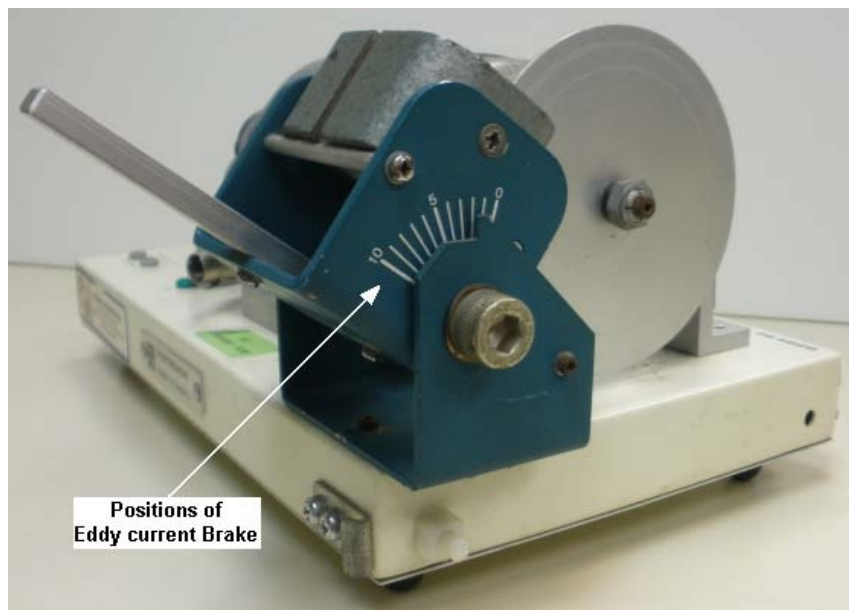
Figure 3–2: Motor loaded through a Eddy current brake

For each position of the braking magnet the load torque, T_L, is computed from (3.1), which is the steady-state solution for T_L from (2.19).

$$T_L = K_T \cdot I_a - B_m \cdot \omega_m \qquad (3.1)$$

The torque T_L is plotted as a function of the motor speed (Figure B–3 in Appendix B). This function follows a linear relationship $T_L = c_1 \omega_m + c_2$. Thus, the constants c_1 and c_2 are calculated using the basic fitting tool from MATLAB® [46]; their values are listed in Table 3–2.

Table 3–1: Parameters for Permanent Magnet DC Motor

Symbol	Parameter	Value	Units
R_a	Armature resistance	8.57	Ω
L_a	Armature inductance	58.7	mH
K_e	Back emf constant	0.1485	$\frac{V}{rad/sec}$
J	Moment of inertia	45.5×10^{-6}	Kgm^2
B_m	Viscous friction coefficient	94.8×10^{-6}	$\frac{Nm}{rad/seg}$

Table 3–2: Load torque characteristic for different positions

Position	Constant c_1 [Nm/(rad/s)]	Constant c_2 [Nm]
0	-0.00006	0.021
2	-0.000029	0.023
3	0.00014	0.024
4	0.00038	0.023
5	0.00055	0.024
6	0.00074	0.023

3.1.2   Specification of the Photovoltaic array

The PV array used for this study consist of two photovoltaic modules BP SX10M connected in series. The electrical characteristics of PVM BP SX10M are presented in Table 3–3. The PVM characteristic constant is $b = 0.084$, which was calculated using the Fixed Point Theorem given in (2.2). The manufacturer datasheet, with more information, can be found in Appendix H.

Table 3–3: PVM BP SX10M Specifications at STC

Symbol	Parameter	Value	Units
I_{sc}	Short-circuit Current	0.65	A
V_{oc}	Open-circuit Voltage	21.0	V
P_{max}	Maximum Power	10.0	W
V_{op}	Voltage at P_{max}	16.8	V
I_{op}	Current at P_{max}	0.59	A
TCi	Temperature coeff. of I_{sc}	(0.065 ±0.015)	$\%/C$
TCv	Temperature coeff. of V_{oc}	-(80 ±10)	mV/C

In order to characterize the PV array, voltage and current measurements are done for different environmental conditions. The PV array is connected directly to a DC electronic load (e.g. BK Precision 8500). In a clear day when the PV array temperature becomes constant, the open-circuit voltage of the PV array is measured and registered by using the voltage constant mode in the DC electronic load. Then, this voltage is decreased by changing the voltage setting until the minimum voltage be achieved, while the voltage and current are registered. This procedure is repeated for different environmental condition.

The environmental condition determines the boundary of the I-V curve; in other words, variations of the open-circuit voltage (V_x) and the short-circuit current (I_x) of the PV array correspond a different irradiance and temperature conditions. Table 3–4 shows the Mean Squared Error (MSE), calculated as the average of the squared of the difference between the measured and calculated PV current.

Table 3–4: Validation of PV model for BPSX10M

Irrandiance (W/m^2)	I_x (A)	V_x (V)	MSE
520	0.303	37.85	6.899×10^{-6}
620	0.393	38.96	3.465×10^{-5}
700	0.469	38.15	7.889×10^{-5}
860	0.562	39.34	9.166×10^{-5}

Figure 3–3 shows the measured and simulated $I - V$ characteristic curves for the PV array; where the markers represent the measured data. The simulated data were obtained using the model given by Equation (2.1). Based on the MSE, it is clear that the model used represents the I-V characteristic with accuracy.

Both for measured data as simulated data the Power (P) is computed by the product the current and voltage. Figure 3–4 shows the measured and simulated $P - V$ characteristic curve for the same environmental conditions.

As can be seen in the $I - V$ characteristic curves, these curves change significantly with the environment variations. Therefore, the output power characteristic is highly dependent on the weather condition. Besides, it is evident that the short-circuit current has more variations than the open-circuit voltage.

Appendix A shows the characteristic curves, current-voltage and power-voltage, for the two PV modules SX10M connected in series. These curves are obtained using the model discussed in previous chapter for a temperature equal to $59°C$ and different irradiance values. These curves can be used to evaluate the correctness of the MPPT methods.
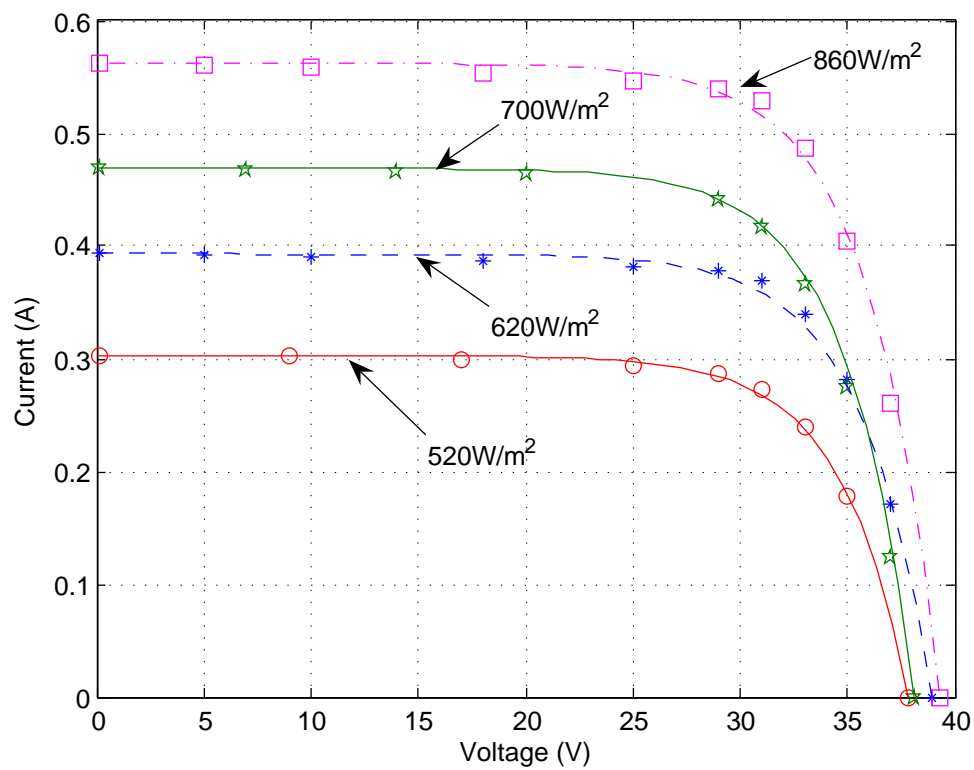
Figure 3–3: I-V Characteristic of PV array
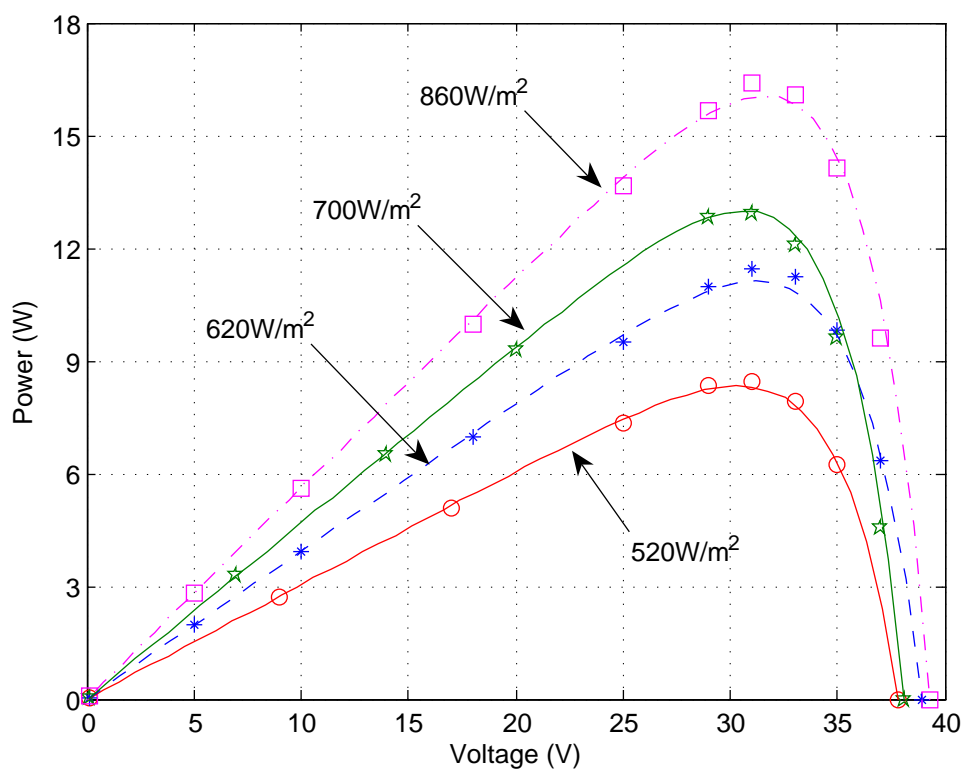
Figure 3–4: P-V Characteristic of PV array

3.2 The Problem of Direct Coupling

Without any interfacing circuitry between the PV array and the DC motor, the operating point can be obtained by solving (3.2) and (3.3), where (3.2) is the electrical equation of a DC motor when the armature voltage is the PVM voltage. The PVM voltage is derived from (2.1).

$$R_a {\cdot} i_a + L_a \frac{di_a}{dt} + K_e {\cdot} \omega_m = V_x + b {\cdot} V_x {\cdot} \ln \left[1 - \frac{i_a}{I_x} + \frac{i_a}{I_x} \exp \left(\frac{-1}{b} \right) \right] \qquad (3.2)$$

$$T_e = J \cdot \frac{d\omega_m}{dt} + B_m \cdot \omega_m + T_L \qquad (3.3)$$

The above equations can be solved by using MATLAB/Simulink$^{®}$ [47] simulation, as shown in Figure 3–5. The details of subsystems: "PVM_Model_volt", "DC motor" and "TL=c1Wm+c2" in Figure 3–5 are shown in Appendix C. In addition to the motor and PV array characteristics, the operating point depends on the temperature and the irradiance values, which determine V_x and I_x according to (2.3) and (2.4).

Then, the stedy-state values of armature current (the same PVM current) and the DC motor speed are obtained by running the simulation of the model shown in Figure 3–5 with the Dormand-Prince numerical integration method. The PVM voltage can be calculated from (2.1); thus the operating point, given by PVM voltage and PVM current, can be finally obtained. Table 3–5 shows some of the results.
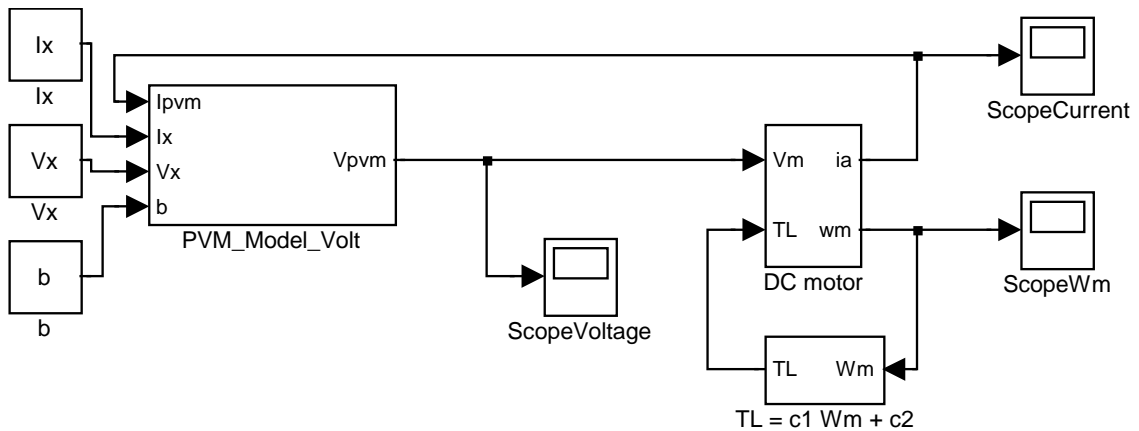
Figure 3–5: Simulink model to find the operating point in direct coupling

Table 3–5: Operating point for Direct Coupling with $T_L = 0.00014\omega_m + 0.024$

$E_i(W/m^2)$	$T°$	$V_x(V)$	$I_x(A)$	$V_{pvm}(V)$	$I_{pvm}(A)$	$P_{pvm}(W)$	$P_{MPP}(W)$
600	59	34.14	0.39	24.35	0.38	9.25	9.88
750	59	35.03	0.49	29.11	0.43	12.51	12.68
900	59	35.94	0.59	31.59	0.45	14.21	15.61
1050	59	36.87	0.69	33.36	0.47	15.67	18.68

If the current-voltage (I-V) characteristics of DC motor are superimposed on a set of photovoltaics I-V curves, the operating point is the intersection between PV and DC motor curves [2, 3]. The DC motor $P - V$ curves for different load characteristics, are superimposed on a set of PV array $P - V$ curves for different irradiance values as shown in Figure 3–6.

The Figure 3–6 shows that for some load characteristics, given by T_L, the motor voltage is always lower that PVM optimal voltage (V_{MPP}); whereas, for the others the motor voltage is greater that the PVM optimal voltage. The MPP is shown for each irradiance value and the horizontal arrows indicate the power and voltage that must be supplied to the DC motor. Table 3–5 shows the maximum power of the PVM (P_{MPP}) for each condition.

In addition, the PVM and the DC motor $I - V$ curves are illustrated in Figure 3–7, where different operating points are shown according to the irradiance conditions and to the load torque. Therefore, there are only few conditions where the operating point is near to the maximum power point in direct coupling.

Using a DC-DC converter as interface, the operating point of the PV array can be moved to the maximum power point. This is possible, because the power converter can change its input resistance. Next section will show the case for the Buck-Boost converter.
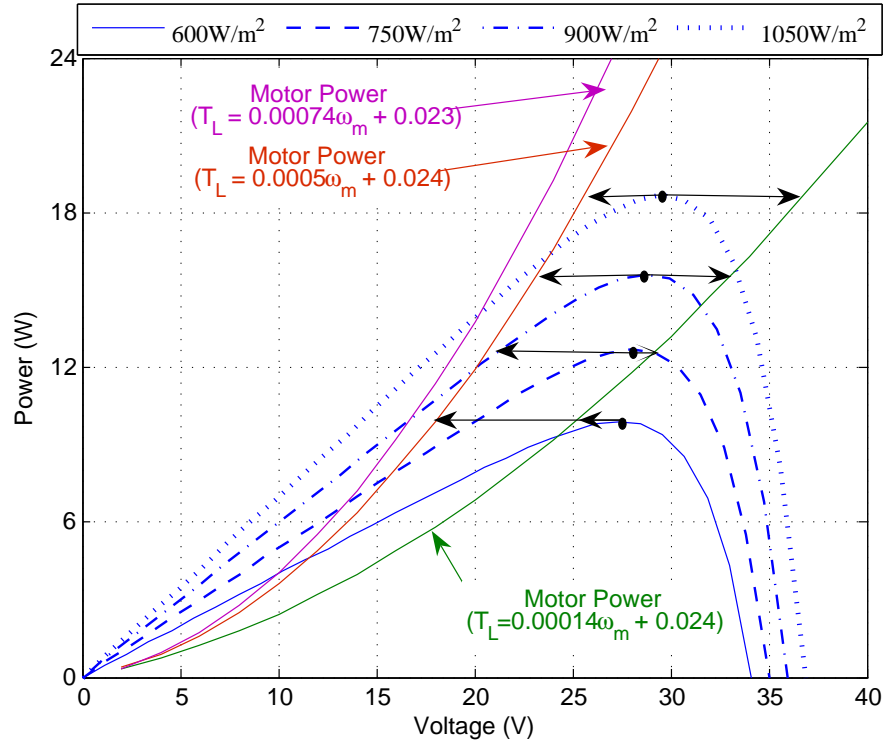
Figure 3–6: Power curves DC motor and PVM
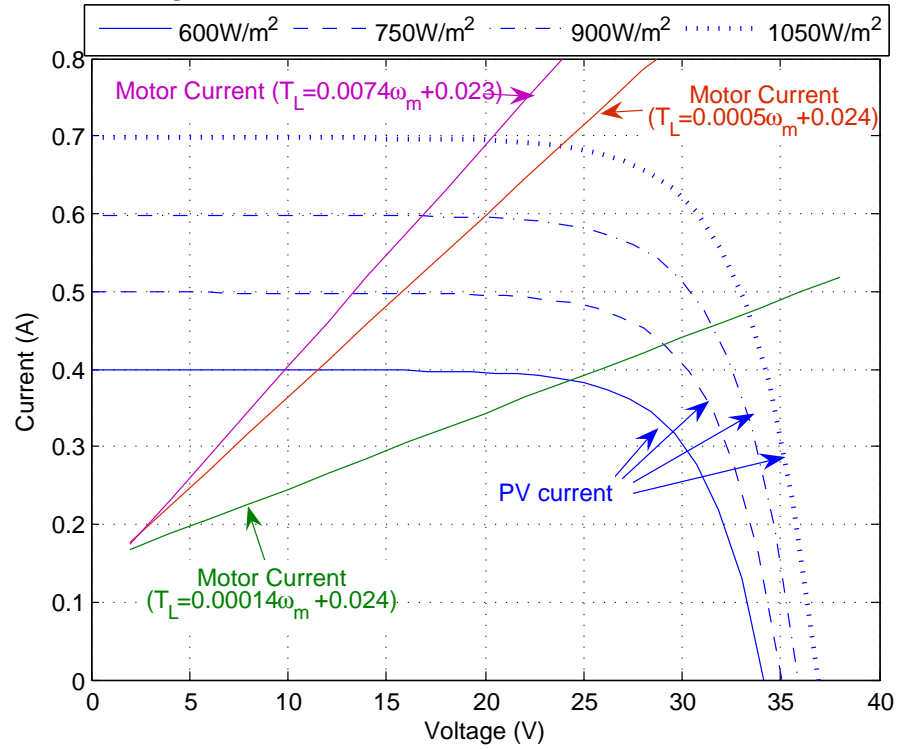
Figure 3–7: PV and DC motor Curves

3.3 Load matching with DC-DC Power converter

The previous section have presented the problem when a DC motor is directly connected to a PVM. This section shows how a DC-DC converter can vary its input resistance; thus, the power converter connected to the PVM can vary its incoming current and the operating point of the PVM.

Figure 3–8 shows a Buck-Boost converter including the inductor copper loss (R_L), while figure 3–9 shows the Buck-Boost during the two switching subintervals. In order to obtain an expression for the input impedance of the Buck-Boost converter, the capacitor current (i_C) and the inductor voltage (v_L) are derived for the switch-on and switch-off states, as in (3.4) and (3.5), respectively.
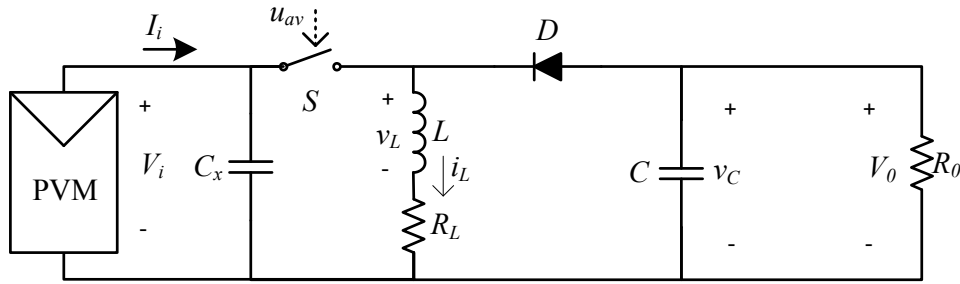
Figure 3–8: Buck-Boost converter connected to a PVM
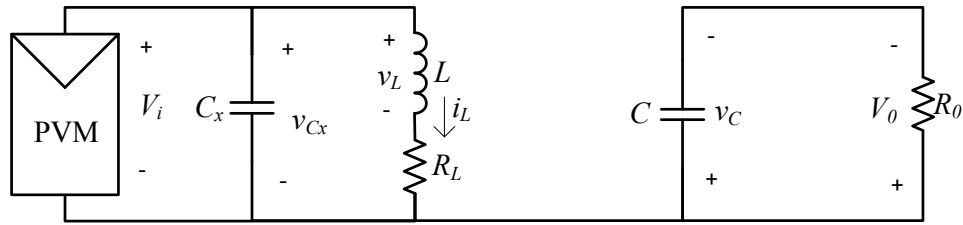
(a) Buck-Boost switch-on state
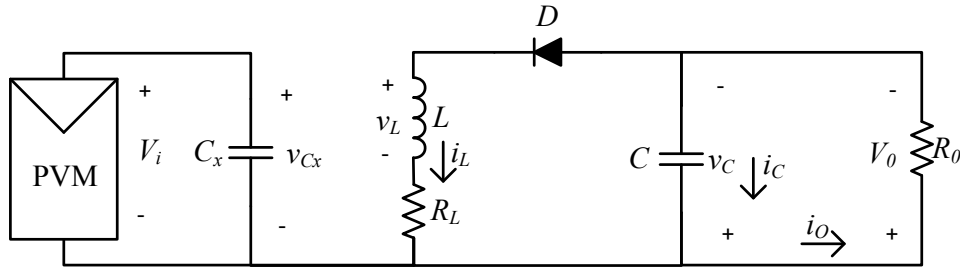
(b) Buck-Boost switch-off state

Figure 3–9: Buck-Boost switch-on state(up), switch-off state(down)

$$i_C = \frac{v_O}{R_0}$$

$$v_L = v_{cx} - i_L \cdot R_L \tag{3.4}$$

$$i_C = i_O - i_L$$

$$v_L = -v_O - i_L \cdot R_L \tag{3.5}$$

In steady-state conditions, the net change in inductor current over one switching period must be zero; therefore, the average value of inductor voltage must have zero dc components (this is called the principle of *inductor volt-second balance*) [34]. Likewise, in equilibrium, the net change over one switching period of the capacitor voltage must be zero; hence, the average value of the capacitor current must be zero (this is called the principle of *capacitor amp-second balance* or *capacitor charge balance*) [34].

Then, applying the principles of inductor volt-second balance and capacitor charge balance, one obtains

$$\frac{v_0}{R_0}D + (\frac{v_0}{R_0} - i_L)(1 - D) = 0 \tag{3.6}$$

$$(v_{cx} - i_L R_L)D - (v_0 + i_L R_L)(1 - D) = 0 \tag{3.7}$$

From Equation (3.6), the inductor current i_L can be expressed as in (3.8), and substituting (3.8) into (3.7), a relationship between v_{cx} and v_O is obtained, which is shown in (3.9)

$$i_L = \frac{1}{1 - D} \cdot \frac{v_O}{R_0} \tag{3.8}$$

$$v_{cx} = \frac{v_O}{D} \cdot \left[\frac{(1 - D)^2 \cdot R_0 + R_L}{(1 - D) \cdot R_0} \right] \tag{3.9}$$

Since the input impedance is defined by $R_i = \dfrac{v_{cx}}{i_i}$ and $i_i = Di_L$, the input impedance can be expressed as

$$R_i = \frac{(1-D)^2 \cdot R_0 + R_L}{D^2} \tag{3.10}$$

The input resistance of a Buck-Boost converter is computed and shown in Figure 3–10 using $R_L = 0.419$ (See datasheet of inductor 1410516C from Murata®in Appendix H), $R_0 = 75\Omega$ (average resistance for a medium load) and D from 0.05 to 0.95.
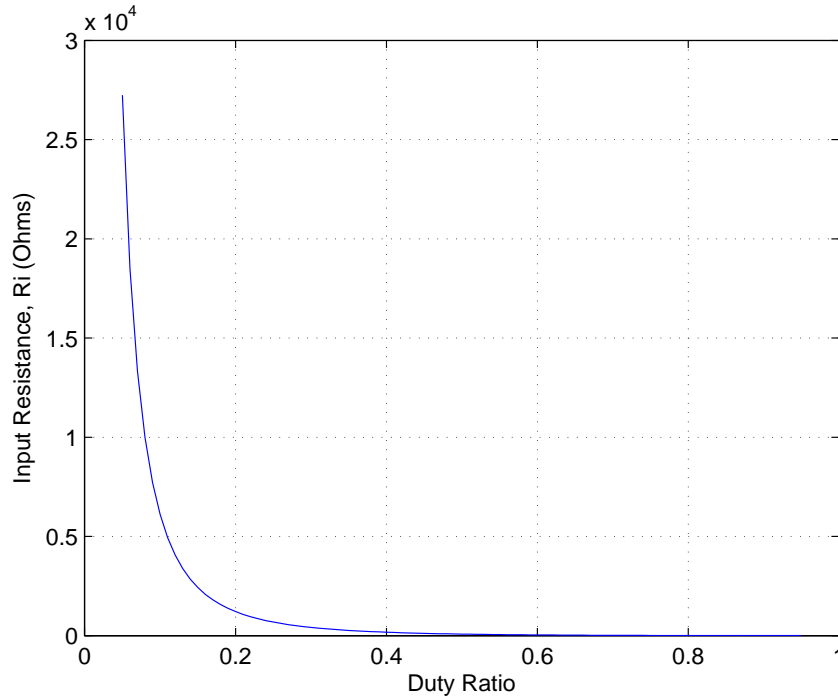
Figure 3–10: Input resistance of Buck-Boost with $R_L = 0.419\Omega$ and $R_0 = 75\Omega$

The above result for R_i is similar to the relationship between input resistance and output resistance, presented in [48], where copper loss were not considered. Figure 3–11 shows the relationship between the normalized input resistance (i.e. R_i/R_0) and the duty ratio when R_L is neglected. The blue line shows the behavior of input resistance for the Buck-Boost converter. The green line shows the characteristic of input resistance of the Boost converter, and the red line illustrates the case for Buck converters.
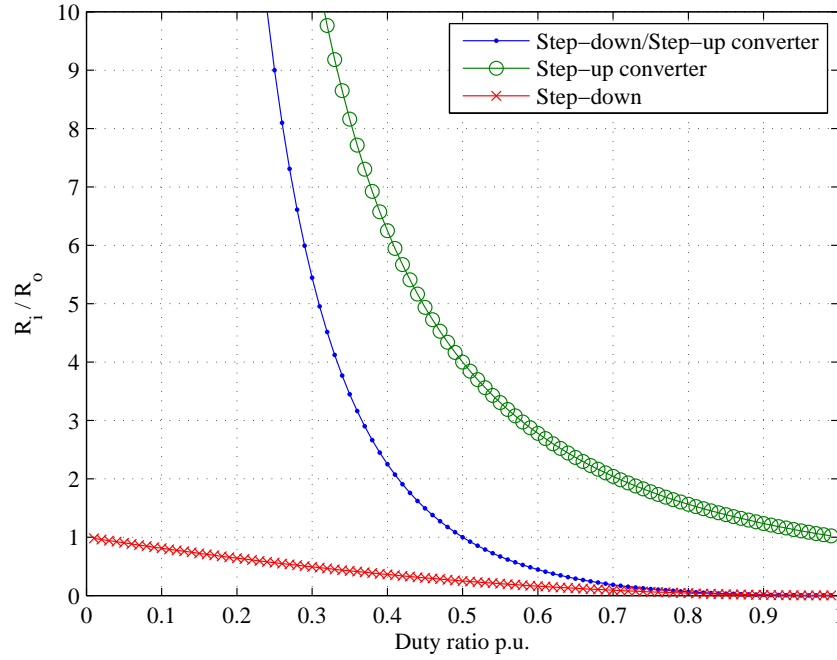
Figure 3–11: Input resistance of Buck-Boost converter

As can be seen from Figure 3–11, the Buck-Boost converters can load a source from open-circuit to short-circuit; whereas the Boost converter has a minimum input resistance (i.e. short-circuit behavior is not possible) and the Buck converter has a maximum input resistance (i.e. open-circuit behavior is not possible).

3.4   Interfacing the Photovoltaic Module to the DC Motor

This section presents the derivation of the optimal duty ratio for a PVM connected to a DC motor through a DC-DC power converter. The optimal duty ratio is the duty ratio that maximizes the PVM power, i.e. if the power converter is driven with the optimal duty ratio, then the PVM operates in the maximum power point.

A Buck converter without the output filter, which is known as a chopper is used as step-down topology, but similar results can be obtained for Buck converters; as step-up topology is analyzed a Boost converter, and as step-down/step-up topology is used a Buck-Boost converter, but these equations can be used for power converter with comparable output-input relation.

3.4.1 Interfacing with Step-down converter
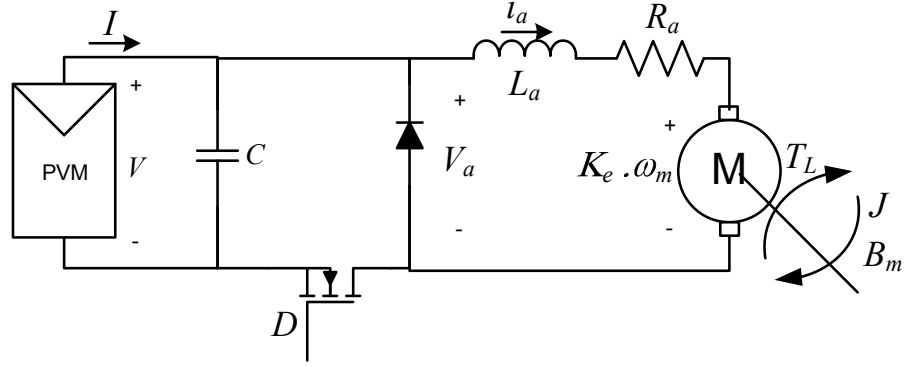
Figure 3–12: PV system supplying a DC motor through step-down converter

Optimal duty ratio of the step-down converter

Using the chopper converter, the duty ratio is expressed as $D = V_o/V_i$. In the system shown in Figure 3–12, the power converter output voltage V_o is equal to the motor armature voltage, V_a. The power converter input voltage V_i is equal to PVM voltage V, or equal to V_{op} if the terminal voltage of the PVM is operating in the maximum power point. Then, the optimal duty ratio is given by (3.11)

$$D = \frac{V_a}{V_{op}} \tag{3.11}$$

The optimal voltage, V_{op} can be derived by means of a maximum power point tracking method, which will be described below. The armature voltage V_a, is given by the steady state solution of (2.18)

$$V_a = R_a \cdot I_a + K_e \cdot \omega_m \tag{3.12}$$

Since $T_e = K_T i_a$, solving for current I_a of (3.3) in steady state condition, yields

$$I_a = (B_m \cdot \omega_m + T_L)/(K_e) \tag{3.13}$$

Therefore, substituting (3.13) into (3.12), yields

$$V_a = R_a \left(\frac{B_m \cdot \omega_m + T_L}{K_e} \right) + K_e \cdot \omega_m \qquad (3.14)$$

So, the optimal duty ratio becomes:

$$D = \frac{V_a}{V_{op}} = \frac{1}{V_{op}} \left[K_e \cdot \omega_m + R_a \left(\frac{B_m \cdot \omega_m + T_L}{K_e} \right) \right] \qquad (3.15)$$

3.4.2 Interfacing with Step-up converter
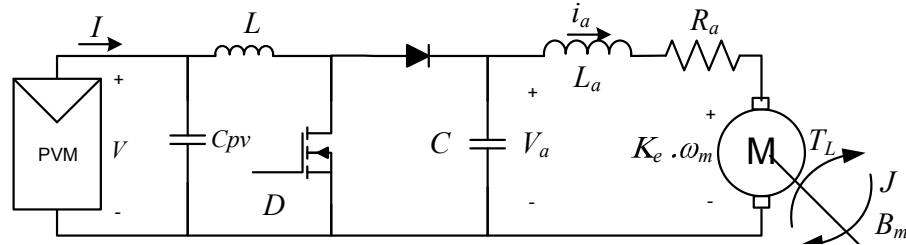
Figure 3–13: PV system supplying a DC motor through step-up converter

Optimal Duty ratio of the Boost converter

Figure 3–13 shows a PVM supplying a DC motor through a Boots converter. For the Boost converters, whose output-to-input voltage conversion ratio is given by (3.16), the similar procedure is done, and from (3.17) optimal duty cycle is derived and shown in (3.18).

$$\frac{V_o}{V_{in}} = \frac{1}{1 - D} \qquad (3.16)$$

$$\frac{1}{1 - D} = \frac{V_a}{V_{op}} = \frac{1}{V_{op}} \left[K_e \cdot \omega_m + R_a \left(\frac{B_m \cdot \omega_m + T_L}{K_e} \right) \right] \qquad (3.17)$$

$$D = 1 - \frac{K_e \cdot V_{op}}{K_e^2 \cdot \omega_m + R_a \cdot B_m \cdot \omega_m + T_L R_a} \qquad (3.18)$$

3.4.3 Interfacing with Step-down/step-up converter
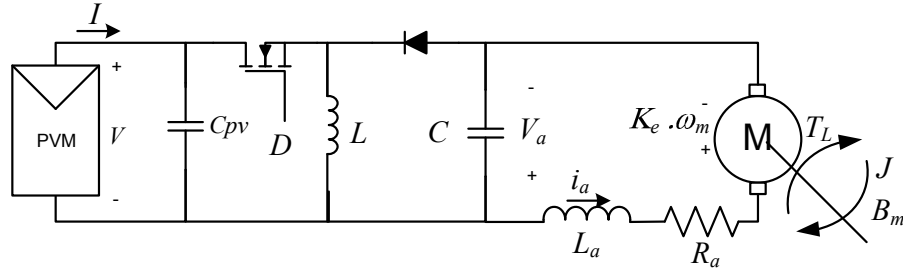
Figure 3–14: PV system supplying a DC motor through step-down/step-up converter

Optimal duty of the step-down/step-up converter

In Figure 3–14 a Buck-Boost converter is used as interface between a PVM and a DC motor. The relationship of input and output voltage of the Buck-Boost, the Cuk and the SEPIC converter is given by (3.19)(Cuk and Buck-Boost reverse the polarity) [34]. If $V_o = V_a$ and $V_{in} = V_{op}$, then, the optimal duty ratio can be derived from (3.20), and is given by (3.21).

$$\frac{V_o}{V_{in}} = \frac{D}{1-D} \tag{3.19}$$

$$\frac{D}{1-D} = \frac{V_a}{V_{op}} = \frac{1}{V_{op}} \left[K_e \cdot \omega_m + R_a \left(\frac{B_m \cdot \omega_m + T_L}{K_e} \right) \right] \tag{3.20}$$

$$D = \frac{R_a \cdot B_m \cdot \omega_m + K_e^2 \cdot \omega_m + R_a \cdot T_L}{R_a \cdot B_m \cdot \omega_m + K_e^2 \cdot \omega_m + V_{op} \cdot K_e + R_a \cdot T_L} \tag{3.21}$$

Table 3–6 summarizes the relationship between the optimal duty ratio and the motor speed for each topology. These results are used in Chapter 5 in order to compare the topologies as interface between a PVM and a DC motor.

Power converter	Optimal Duty Ratio
Step-down	$D = \dfrac{1}{V_{op}} \left[K_e \omega_m + R_a \left(\dfrac{B_m \omega_m + T_L}{K_e} \right) \right]$
Step-up	$D = 1 - \dfrac{K_e V_{op}}{K_e^2 \omega_m + R_a B_m \omega_m + T_L R_a}$
Step-down/Step-up	$D = \dfrac{R_a B_m \omega_m + K_e^2 \omega_m + R_a T_L}{R_a B_m \omega_m + K_e^2 \omega_m + V_{op} K_e + R_a T_L}$

Table 3–6: Summary of optimal duty ratio

Chapter 4

Design and Implementation of MPPT

An analysis of the system has been done in the previous chapter when a DC-DC power converter is used as interface between the photovoltaic generator and the DC motor. In addition, it has been shown that an optimal duty ratio can be found, attaining operation around the maximum power point. This section describes different methods for managing the duty ratio of the power converter automatically; thus, to track the maximum power point. These methods, whose theory has been explained in Section 2.2, are: Linear Reoriented Coordinates Method (LRCM), Perturbation and Observation (P&O) and INcremental Conductance (INC); as well as, a method based on positive speed feedback. Schematic diagrams, circuits and algorithms developed are detailed for each of the methods.

4.1   MPPT using Linear Reoriented Coordinates Method

An MPPT must perform two tasks: first, to find the maximum power point, and second to keep the PVM operation at that point. Many methods have been proposed in order to find the MPP, in this case the Linear Reoriented Coordinates Method (LRCM) is analyzed. This method estimates the approximated optimal voltage (V_{ap}) using the open-circuit voltage V_{oc}; as well as, the approximated optimal current (I_{ap}) using the short-circuit current I_{sc}, as has been shown in Section 2.2.1.

Because the maximum power point given by V_{ap} and I_{ap} is unique under a given temperature and irradiance, either the optimal voltage or the optimal current can be used as the set point for a controller. However, the ideal controlled variable that

characterizes the MPP should be constant or should change slowly within a certain range; accordingly, the photovoltaic voltage is preferred as control variable [10, 11]. Therefore, a voltage control loop is designed.

Since the approximated optimal voltage must be calculated by a microcontroller, it is desirable to simplify the equation for V_{ap} shown in (2.5). Thus, the execution time and the program memory are minimized. Then, the Equation (2.5) can be simplified in the following way:

$$V_{ap} = V_x + bV_x \ln \left(b - b \exp \left(-\frac{1}{b} \right) \right) \leq V_{MPP}$$

$$V_{ap} = V_x \left[1 + b \ln \left(b - b \exp \left(-\frac{1}{b} \right) \right) \right] \tag{4.1}$$

$$V_{ap} = V_x \cdot K_v \tag{4.2}$$

in this manner, the set point for the voltage control loop can be calculated by Equation (4.2), where the constant K_v that only depends on the characteristic constant b of the PV module, is given by

$$K_v = 1 + b \cdot \ln \left(b - b \cdot \exp \left(-\frac{1}{b} \right) \right) \tag{4.3}$$

A DC-DC power converter can vary the current coming from the PVM [10]; thus, the operating point is changing according to the duty ratio. Therefore, a controller adjusts the power converter duty ratio in order to maintain the PVM voltage at its set point (i.e. V_{ap}); then, the duty ratio will be the manipulated variable.

Figure 4–1 shows a simplified diagram of the proposed system using LRCM. This system includes a PV array or PVM, a DC-DC converter, a DC motor and a control subsystem. The control subsystem includes an ATMEL's ATmega88 8-bit microcontroller; interface circuits that includes sensors and signal conditioners

connected to the analog-to-digital converter of the microcontroller, and a driver for the power MOSFET.
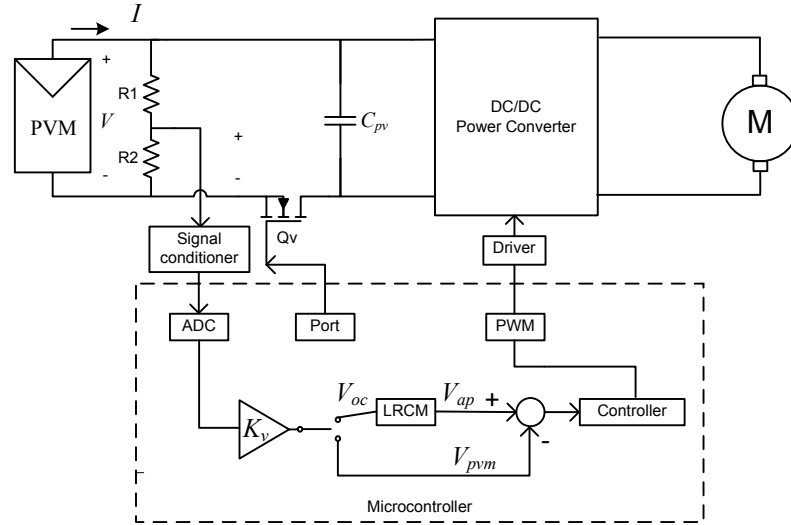
Figure 4–1: Digital MPPT with LRCM

The voltage divider composed of R_1 and R_2 is used to sense the PVM voltage V; moreover, the voltage divider can sense the open-circuit voltage when the transistor Q_v disconnects the PVM. The microcontroller reads the PVM voltage through its internal ADC, and drives the Q_v in order to connect or disconnect the PVM. The PWM signal that drives the power converter is generated by the microcontroller by using its internal timer. The microcontroller also implements the LRCM and the control algorithm.

4.1.1 System Operation

Figure 4–2 describes the executed operation by the microcontroller, this one uses its internal timer to control the sampling time for the controller and the time to update the set point. First, the initial ADC, ports and timers parameters are established (See Appendix D). Then, the microcontroller disconnects the PVM, senses the open-circuit voltage (V_{oc}) and calculates the optimal voltage (V_{ap}) using LRCM.

Main Program: Interrupt routine:

```
   ┌─────────┐                      ┌─────────┐
   │  Start  │                      │  Enter  │
   └────┬────┘                      └────┬────┘
        │                                │
  ┌─────▼──────┐               ┌─────────▼────────┐
  │Init ADC,   │               │ Increment CountA │
  │Timer, PWM  │               └─────────┬────────┘
  └─────┬──────┘                         │
        │                           ╱────▼────╲        Yes   ┌──────────┐
  ┌─────▼──────┐                   ╱ CountA=nTs ╲──────────▶ │ Control  │
  │Init USART, │                   ╲            ╱            │algorithm │
  │Port        │                    ╲──────────╱             └────┬─────┘
  └─────┬──────┘                         │ No                     │
        │                                │                  ┌─────▼────┐
  ┌─────▼──────┐                         │                  │ CountA=0 │
  │   LRCM     │                         │                  └─────┬────┘
  └─────┬──────┘               ┌─────────▼────────┐◀──────────────┘
        │                      │Increment CountB=0│
  ┌─────▼──────┐               └─────────┬────────┘
  │  Enable    │                         │
  │ Interrupt  │                    ╱────▼────╲        Yes    ┌────────┐
  └─────┬──────┘                   ╱ CountB=nTu ╲───────────▶ │  LRCM  │
        │                          ╲            ╱             └───┬────┘
   ╱────▼────╲                      ╲──────────╱                  │
  ╱ Wait for  ╲                          │ No               ┌─────▼────┐
  ╲ interrupt ╱                          │                  │ CountB=0 │
   ╲─────────╱                           │                  └─────┬────┘
        │                          ┌─────▼────┐◀──────────────────┘
        └──loop                    │  Return  │
                                   └──────────┘
```
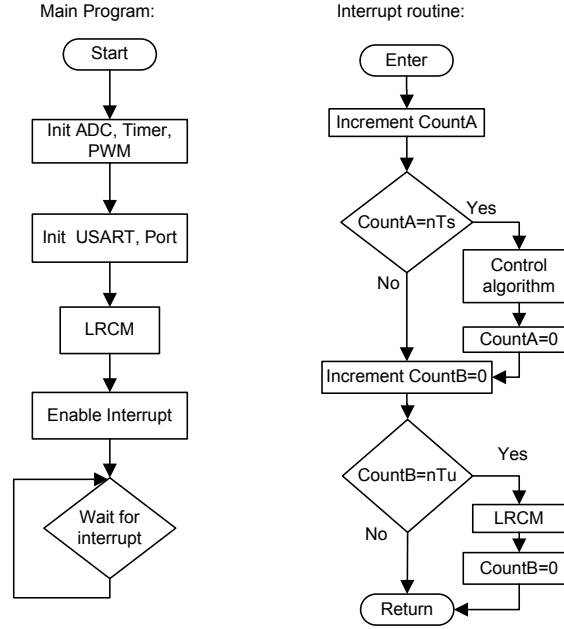
Figure 4–2: MPPT with LRCM flowchart

On every event that the timer OVerFlow (OVF) interruption is called, the sampling time and the time to update the set point are checked by the microcontroller. If the sampling time is accomplished, the control subroutine is carried out; this subroutine includes reading the PVM voltage, calculating the error, calculating the control signal and updating the duty ratio. In like manner, if the time to update the set point finishes, the optimal voltage (V_{ap}) is calculated again using LRCM.

4.1.2   Hardware and Software design

The components and tasks required for successful operation of the system are detailed below. This description includes the way to obtain a constant sampling period, the procedure to implement the controller, the method to generate the PWM signal that drives the MOSFET, and the circuit to sense the voltage of the PVM.

Synchronization

During system operation, the PVM voltage is sampled at regular intervals. The time between intervals is constant and is known as the sampling time (T_S). In order to obtain an exact sampling time, the internal timer of the microcontroller is

used, specifically, the Timer Overflow interrupt. This technique is one of the most commonly used, because it has the advantage of accurate implementation [49].

In this manner, the control algorithm is written inside the timer Interrupt Service Routine (ISR), but this algorithm is not executed on each interrupt because the sampling time must be controlled. Then, a interrupt counter is used in order to obtain the synchronization as is describe below.

The Timer Overflow interrupt occurs every time the content of the timer transitions from maximum to zero. The maximum content of an n-bits timer is equal to $2^n - 1$. If the microcontroller is externally clocked by an F MHz crystal oscillator, and the timer has no preescaler, the number of INTerrupts per SECond (INTXSEC) is given by

$$\text{INTXSEC} = \frac{F \times 10^6}{2^n} \tag{4.4}$$

where F is the clock frequency in MHz and n is the bit number of the timer.

After calculating the number of interrupts per second, this values is multiply by the sampling time in seconds (T_S), i.e. $\text{TIMEOK} = \text{INTXSEC} T_S$. This result is used for indicating when the control algorithm must be executed as shown in the following sequence of steps:

Algorithm 1 Pseudo-code to synchronization using Timer Overflow Interruption
---
  1: Interrupt Service Routine(Timer_Overflow){
  2: Increment counter
  3: **if** counter = TIMEOK **then**
  4:     Execute control algorithm
  5:     Set counter to zero
  6: **end if**
  7: }

Control Algorithm

The control algorithm is a set of instructions that runs at start of every sampling time. With these instructions the value of the optimal values is read, the actual

voltage of the PVM is also read and the error is calculated. Then, the controller output for this sampling instant is calculated, and the output is sent to the PWM generator. The algorithm is summarized in the following steps:

Algorithm 2 Control algorithm executed at every sampling time
---
1: Read the value of the optimal voltage
2: Read the actual voltage of the PVM
3: Calculate the error
4: Calculate the output of the controller
5: Update the variables for the next sample
6: Update the duty cycle of the power converter

The controller implemented is a Proportional-Integral (PI) controller, which is currently one of the most used controller in the process industry and is capable to provide an acceptable performance for the majority of the process control tasks [49, 50]. The control action of a PI is given by its ideal representation

$$u(t) = K_p \left[e(t) + \frac{1}{T_i} \int_0^\infty e(t)dt \right] \tag{4.5}$$

where $u(t)$ is the output of the controller and $e(t) = r(t) - y(t)$ is the error, in which $r(t)$ is the optimal voltage and $y(t)$ is the actual voltage of the PVM. K_p and T_i are known as proportional gain and integral time respectively and are parameters of the controller that need to be determined.

To implement the PI controller on a digital computer, the equation must be converted from continuous to discrete representation. The simplest method for doing this is approximated the integral term by the trapezoidal rule, which is also known as Bilinear transform or Tustin's method[51]. Then, (4.5) becomes

$$u(t_k) = K_p \cdot e(t_k) + K_i \left(\frac{e(t_k) + e(t_{k-1})}{2} \right) T_S + u(t_{k-1}) \tag{4.6}$$

In this manner, the control variable $u(t_k)$ at the time t_k is computed from its value at the previous time instant $u(t_{k-1})$, the error and the error at time t_{k-1}. The algorithm to be implemented on the microcontroller is described below

Algorithm 3 Digital PI controller subroutine

1: Read the error $e(t_k)$
2: Calculate proportional term, $u_p(t_k) \leftarrow K_p e(t_k)$
3: Calculate the integral term, $u_i(t_k) \leftarrow u_i(t_{k-1}) + K_i \left(\frac{e(t_k) + e(t_{k-1})}{2} \right) T_S$
4: **if** $u_i(t_k) > \text{MAX}$ **then**
5:    $u_i(t_k) \leftarrow u_i(t_{k-1})$
6: **else**
7:    $u_i(t_{k-1}) \leftarrow u_i(t_k)$
8: **end if**
9: Calculate the controller output $u(t_k) \leftarrow u_p(t_k) + u_i(t_k)$
10: **if** $u(t_k) > \text{MAX}$ **then**
11:    $u(t_k) \leftarrow \text{MAX}$
12: **else if** $u(t_k) < \text{MIN}$ **then**
13:    $u(t_k) \leftarrow \text{MIN}$
14: **end if**
15: **return** $u_(t_k)$

In the algorithm that implements (4.6) (Algorithm 3), from line 4 to 8 the algorithm eliminates the integral wind-up from the controller stopping the integration when the action integral is saturated. This method is known as conditional integration [49]. Between lines 10 and 8, the algorithm saturates the controller output fixing a MAX value and a MIN value.

PWM generation

The output of the controller adjusts the duty ratio D of the switch control signal. The switch control signal, is also know as PWM signal, its switching frequency must be constant while the duty ratio is varied according to the controller output.

The PWM signal is generated using the internal modules of the microcontroller; these modules are a counter, a comparator, logic switches and special-purpose registers. When the microcontroller is set-up in PWM mode, the counter increments until the counter value matches with the special-purpose register value or the counter reach the top values. When a match occurs, the PWM output is cleared and is set when the counter transitions from top to bottom [52, 53]. The value for the special-purpose register (REGPWM) is calculated using the controller output, this values

specifies the on duration in terms of the counter value. This value is given by

$$\text{REGPWM} = \frac{U_{\text{MAX}} - u(t_k)}{U_{\text{MAX}}} 2^{n_c} - 1 \qquad (4.7)$$

where, U_{MAX} is the maximum value for the controller output, $u(t_k)$ is the controller output and n_c is the bit number of the counter.

Voltage and Current sensing

In order to sense the voltage of the PVM a voltage divider is used, their output voltage is connected to a voltage buffer, which avoids loading the PVM. Because a single supply buffer is designed, the operational amplifier must be carefully selected for proper operation, allowing common-mode input-voltage down to the negative supply. The chosen amplifiers is CA3130 from Intersil®, whose datasheet can be found in Appendix H.

A MOSFET has been added to the negative terminal of the PVM. This MOSFET connects and disconnects the PVM when the open circuit voltage is required. The MOSFET gate is driven by the microcontroller.

A Hall effect-based current sensor (ACS712) is used as solution to the current sensing. This measurement is only required for searching MPPT methods. The Hall effect integrated circuit provides a proportional voltage when the current flow through its conduction path. This output voltage is conditioned by an instrumentation amplifier (AD620) in order to adjust the zero and the span to the desired level. In addition an RC low pass filter is added in the final stage.

The conditioner circuit for sensing of the voltage and the current is shown in figure 4–3. The output voltage of the CA3130 is a proportional voltage to the PVM voltage and the output voltage of the AD620 is a proportional voltage to the current. Both outputs are connected to the analog to digital converter of the microcontroller.
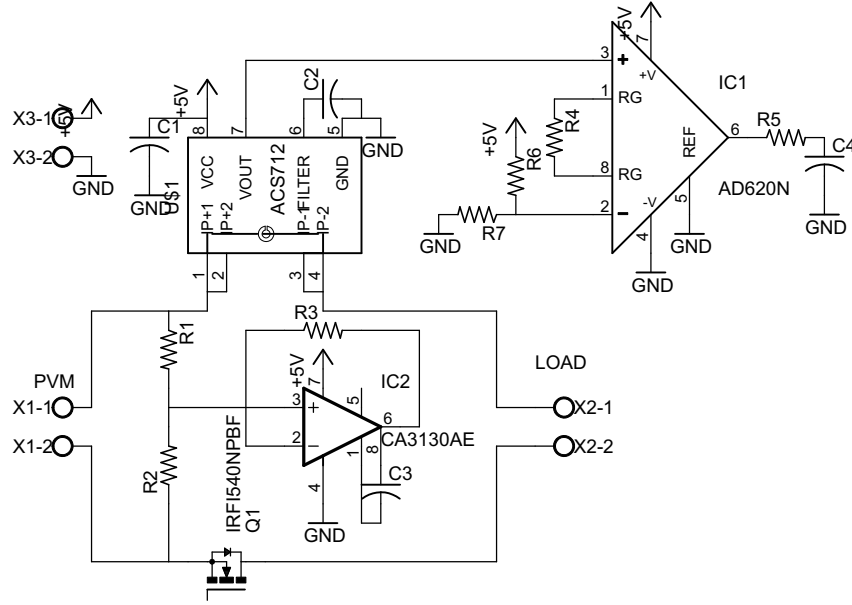
Figure 4–3: Conditioner circuit for voltage and current sensing

4.2 MPPT using Positive speed feedback

This method is based on the relationship between the optimal duty ratio and the motor speed, which was derived in the previous chapter for a step-down converter. By substituting $T_L = c_1\omega_m + c_2$ into equation (3.15) and reorganizing terms, we can note that the optimal duty ratio can be written as:

$$D = A + B \cdot \omega_m \tag{4.8}$$

where A and B are given by (4.9) and (4.10).

$$A = \frac{R_a \cdot c_2}{V_{op} \cdot K_e} \tag{4.9}$$

$$B = \frac{K_e}{V_{op}} + \frac{R_a(B_m + c_1)}{V_{op} \cdot K_e} \tag{4.10}$$

Since the optimal duty ratio has the form $D = A + B\omega_m$, this control law can be implemented using an analog circuit as shown in Figure 4–4 [41]. This configuration uses a tachometer, which generates a voltage, V_{tach}, proportional to speed given by $V_{tach} = K_{th}\omega_m$. For a PWM generator, the duty ratio is given by $D = K_D v_c$, with

$K_D = \frac{1}{V_{max}}$ and $v_c = V_{adj} + K_a V_{tach}$. The variables V_{adj} and K_a are adjusted to obtain the A and B values according to (4.11); from which $A = K_D V_{adj}$ and $B = K_D K_a K_{th}$

$$D = K_D \cdot V_{adj} + K_D \cdot K_a K_{th} \cdot \omega_m \tag{4.11}$$
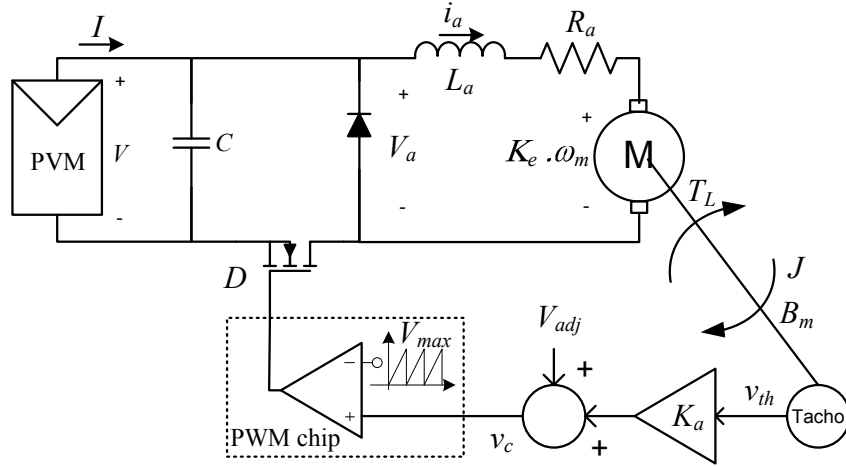
Figure 4–4: Analog implemetation of positive feedback of speed

If the optimal duty ratio vs maximum motor speed can be plotted for several values of irradiance, The constants A and B can be calculated, using least square method. Once A and B are known, V_{adj} and K_a, can be calculated.

In order to obtain a relationship between the optimal duty ratio and the maximum motor speed, we derive the last one from the power balance equation under steady state condition. This is:

$$P = I_a^2 \cdot R_a + E_a \cdot I_a \tag{4.12}$$

Knowing that $E_a I_a$ is the power in rotational motion, which is equal to the product of the torque and angular velocity, then the Equation (4.12) becomes:

$$P = I_a^2 \cdot R_a + T_L \cdot \omega_m \tag{4.13}$$

Substituting (3.13) into (4.13) we can get the Equation (4.14), which is used to calculate the DC motor speed when the power is known. If we assume that

efficiency of power converter is 100%, the motor power is equal to PVM power, which is obtained using the MPPT method.

$$P = B_m \cdot \omega_m^2 + T_L \cdot \omega_m + \left(B_m^2 \cdot \omega_m^2 + 2B_m \cdot \omega_m T_L + T_L^2\right) \frac{R_a}{K_e^2} \qquad (4.14)$$

For different irradiance values, we can use the PVM model and the MPPT method described above, to find the maximum power, P_{max}, and the optimal voltage, V_{op}. Then, we calculate the motor speed using (4.14) and the armature voltage from (3.12). Afterwards, optimal duty ratio is calculated from (3.11). Finally, we must graph the optimal duty ratio against the motor speed, and the constants A and B can be calculated using curve fitting techniques.

Figure 4–5 shows a digital way for implementing this method, where a microcontroller evaluates the Equation (4.11), using its analog-to-digital converter to read the tachometer voltage, and using its timer to generate the PWM signal.
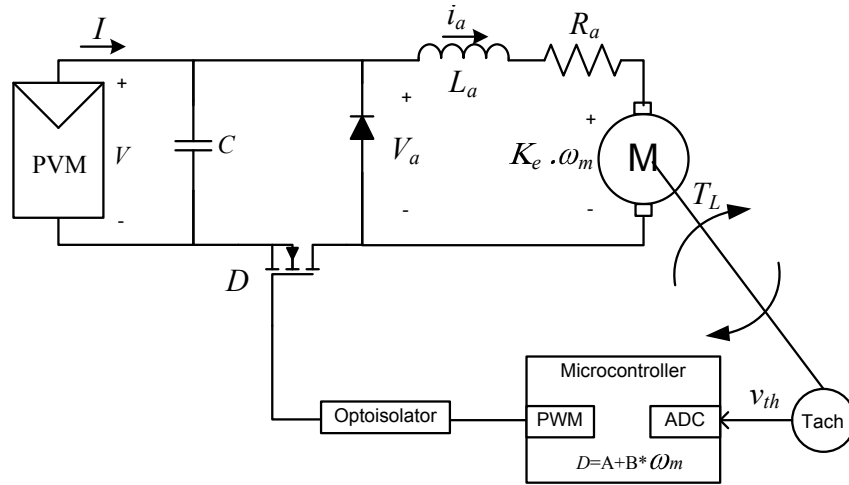
Figure 4–5: Digital Implementation of positive feedback of speed

4.3 Searching MPPT methods

Both the Perturbation and Observation (P&O) and the INcremental Conductance (INC) require measurements of the voltage and the current of the PVM, a

DC-DC converter and a microcontroller. The measurements allow to know the operating point of the PVM, the DC-DC converter can change the operating point, and the microcontroller, based on the measurements, decides how to move the operating point until the Maximum Power Point (MPP) of the PVM be reached.

Figure 4–6 shows the scheme of the designed system, which can be used with either P&O or INC method. The conditioner circuit used in LRCM, shown in figure 4–3, can be reused for obtaining the measurements of the PVM voltage and the PVM current. Likewise, the DC-DC converter and the microcontroller can be also reused. In this way, the developed board is flexible and allows the implementation of several MPPT methods, only updating the main program of the microcontroller.
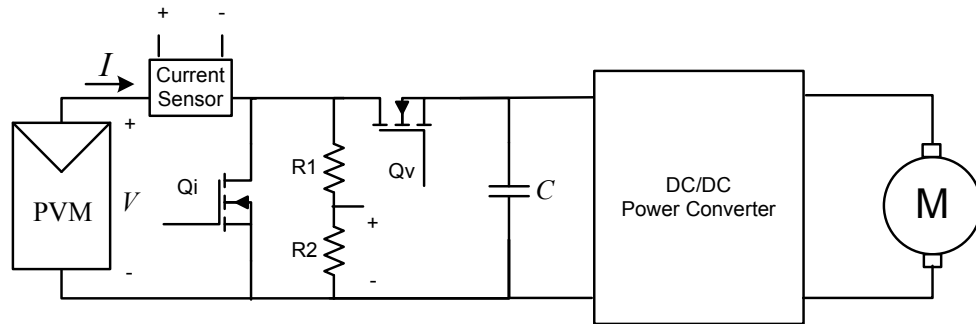
Figure 4–6: Implementation of searching MPPT methods as P&O or INC

For the searching MPPT methods, the main program of the microcontroller initializes the variables and configure the internal components: defining the port directions; initializing the Analog to Digital Converter (ADC), the Universal Synchronous/Asynchronous Receiver Transmitter (USART), the timers; setting up the PWM generator; initializing the duty ratio; and activating the output to connect the PVM to the power converter.

After the initializations, the program begins an infinite loop, waiting for the timer overflow interruption be called. This interruption routine is responsible for the synchronization of the sampling time, executing the control algorithm at constant intervals(as in the Algorithm 1). The control algorithm can be either the P&O or the INC method, which are described below.

4.3.1 Operation of INC MPPT method

As was previously shown in Section 2.2.3, the region of the operating point can be determined by comparing the instantaneous conductance (I/V) to the incremental conductance $(\Delta I/\Delta V)$, as is described by Equation (2.11), which is shown below for convenience:

$$
\begin{cases}
\frac{\Delta I}{\Delta V} = -\frac{I}{V} & \text{at the MPP} \\[2mm]
\frac{\Delta I}{\Delta V} > -\frac{I}{V} & \text{to the left of the MPP} \\[2mm]
\frac{\Delta I}{\Delta V} < -\frac{I}{V} & \text{to the right of the MPP}
\end{cases}
\tag{4.15}
$$

Once the region of the operating point is known, the control variable must be modified to move the operating point toward the MPP. The control variable can be a voltage reference or the duty ratio directly [21]. In this case the duty ratio has been chosen as the control variable.

Since, it was shown that reducing the duty ratio increases the input resistance (Section 3.3, figure 3–11), then to decrease the duty ratio moves the operating point to the right in the PVM characteristic curve, increasing the PVM voltage whereas the PVM current reduces. Conversely, to increase the duty ratio move the operating point to the left in the PVM characteristic curve, because of the input resistance decreases and the PVM supplies more current.

Therefore, considering the effect of the duty ratio on the operating point of the PVM and the comparisons between instantaneous conductance and incremental conductance (Equation (4.15)), the INC MPPT method can be summarized by Algorithm 4.

Algorithm 4 Incremental conductance MPPT method

1: Read the PVM voltage, $V(t_k)$
2: Read the PVM current, $I(t_k)$
3: Calculate increments: $\Delta I = I(t_k) - I(t_{k-1})$, $\Delta V = V(t_k) - V(t_{k-1})$
4: **if** $\Delta V \neq 0$ **then**
5:     Calculate incremental conductance $\Delta G = \Delta I / \Delta V$
6:     Calculate instantaneous conductance $G = I(t_k)/V(t_k)$
7:     **if** $\Delta G \neq -G$ **then**
8:       **if** $\Delta G > -G$ **then**
9:         Decrement duty ratio: $D(t_k) = D(t_{k-1}) - \Delta D$
10:       **else**
11:         Increment duty ratio: $D(t_k) = D(t_{k-1}) + \Delta D$
12:       **end if**
13:     **end if**
14: **end if**
15: Update variables: $D(t_{k-1}) = D(t_k)$, $I(t_{k-1}) = I(t_k)$, $V(t_{k-1}) = V(t_k)$

4.3.2   Operation of P&O MPPT method

The Perturbation and Observation (P&O) method is also implemented with the microcontroller, reusing the conditioner circuit shown in figure 4–3. Then, by measuring the PVM voltage and current, the PVM output power is calculated and compared to the previous PVM output power; according to the result of this comparison, the duty ratio is adjusted, as was explained in Section 2.2.3, moving the operating point toward the maximum power point (MPP).

The P&O method is summarized in Algorithm 5, which is repeated at regular intervals, using the internal timer of the microcontroller, in a similar manner that the sampling time was configured for the LRCM. However, the selection of the sampling time depends on each method; for searching methods, it is necessary that the time between two consecutive samples is long enough to allow the PVM output power reach its steady-state value [29].

Algorithm 5 Perturbation and Observation MPPT method

1: Read the PVM voltage, $V(t_k)$
2: Read the PVM current, $I(t_k)$
3: Calculate the power: $P(t_k) = V(t_k)I(t_k)$
4: **if** $P(t_k) < P(t_{k-1})$ **then**
5:    Reverse the perturbation: $\Delta D = -\Delta D$
6: **end if**
7: Calculate duty ratio: $D(t_k) = D(t_{k-1}) + \Delta D$
8: Update variables: $D(t_{k-1}) = D(t_k)$, $P(t_{k-1}) = P(t_k)$

Chapter 5

Results

In this chapter the results of the comparison among power converters as interfaces are shown; several figures illustrate the relationship between the duty ratio and the maximum power for each topology at different loads. Then, an overview of the developed system using a buck-boost converter and a microcontroller is presented, summarizing the interconnection of each component. Moreover, this chapter also presents the results of each MPPT method, showing both experimental and simulation results. Some simulations were done using MATLAB/Simulink® [47], while in other simulations were done using Synopsys's Saber® Simulator [54].

In the comparison of power converters as interface and in the experimental results, positions 0, 2, 3, 4, 5, and 6 indicate the position of the braking magnet of an eddy current brake. The corresponding braking torque values are shown in Table 5–1. The procedure for calculating the load torque characteristics has been described in Section 3.1.1.

Table 5–1: Characteristics of load torque for each position of the braking magnet

Position	Load torque T_L (Nm)
0	$-0.00006\omega_m + 0.021$
2	$-0.000029\omega_m + 0.023$
3	$0.00014\omega_m + 0.024$
4	$0.00038\omega_m + 0.023$
5	$0.00055\omega_m + 0.024$
6	$0.00074\omega_m + 0.023$

5.1 Comparison of power converter as interface between PVM and DC motor

In Section 3.4, optimal duty ratio expressions for each power converter have been derived. The relationship between optimal duty ratio and maximum power, as well as, the relationship between optimal duty ratio and maximum motor speed can be calculated for each studied topology by the procedure shown in Figure 5–1. This procedure is also repeated for each load condition.

Therefore, for each topology it is possible evaluate the optimal duty ratio in order to determine if the topology is suitable to extract the maximum power; while different loads and different irradiance values are considered. The irradiance have been varied from $200W/m^2$ to $1200W/m^2$, and the procedure have been repeated for the positions 0, 2, 4 and 6 of the braking magnet.

Figures 5–2(a), 5–2(b) and 5–2(c) show the relationship between optimal duty ratio and maximum power at different irradiance values for step-down, step-up and step-up/step-down converters respectively. Figs. 5–3(a), 5–3(b) and 5–3(c) show the relationship between optimal duty ratio and maximum speed for step-down, step-up and step-up/step-down converters respectively.

As the duty ratio must be between 0.0 and 1.0 p.u., careful topology selection should be done according to the kind of load; for example, if the load is set up to the position 4, a step-down converter is suitable to match the PVM and the DC motor. In contrast, a step-down converter is not suitable with the load in position 0, because in this case it would require a duty ratio greater than 1 in order to extract the maximum power, as shown in figure 5–2(a).

```
                        ┌──────────┐
                        │  Start   │
                        └──────────┘
                             │
                             ▼
              ┌──────────────────────────────┐
              │   Read DC motor parameters    │
              │   Read PV array parameters    │
              └──────────────────────────────┘
                             │
                             ▼
              ┌──────────────────────────────┐
              │   Select a temperature value  │
              └──────────────────────────────┘
                             │
                             ▼
         ┌────────────────────────────────────────┐
         │  Select a minimum Irradiance (Ei_o)      │
         │  Select a maximum irradiance (Ei_max)    │
         └────────────────────────────────────────┘
                             │
                             ▼
     ┌──────────────────────────────────────────────┐
     │  Calculate Ix, Vx, from (2.3) and (2.4)        │
     │  Calculate Iap, Vap and Vap, using LRCM         │
     │  Calculate ωmax, from (4.14)                    │
     └──────────────────────────────────────────────┘
                             │
                             ▼
         ┌────────────────────────────────────────┐
         │   Calculate duty ratio for each power    │
         │   converter, using Table (3.5)           │
         └────────────────────────────────────────┘
                             │
                             ▼
              ┌──────────────────────────────┐
              │   Increment irradiance Ei     │
              └──────────────────────────────┘
                             │
                             ▼
                  ╱───────────────────╲
        True     ╱    Ei < Ei_max       ╲
        ◄────────┤                       │
                  ╲───────────────────╱
                             │
                           False
                             ▼
         ┌────────────────────────────────────────┐
         │   Plot D vs ωmax and D vs Pap            │
         └────────────────────────────────────────┘
                             │
                             ▼
                        ┌──────────┐
                        │   End    │
                        └──────────┘
```

Calculate I_x, V_x, from (2.3) and (2.4)
Calculate I_{ap}, V_{ap} and V_{ap}, using LRCM
Calculate ω_{max}, from (4.14)

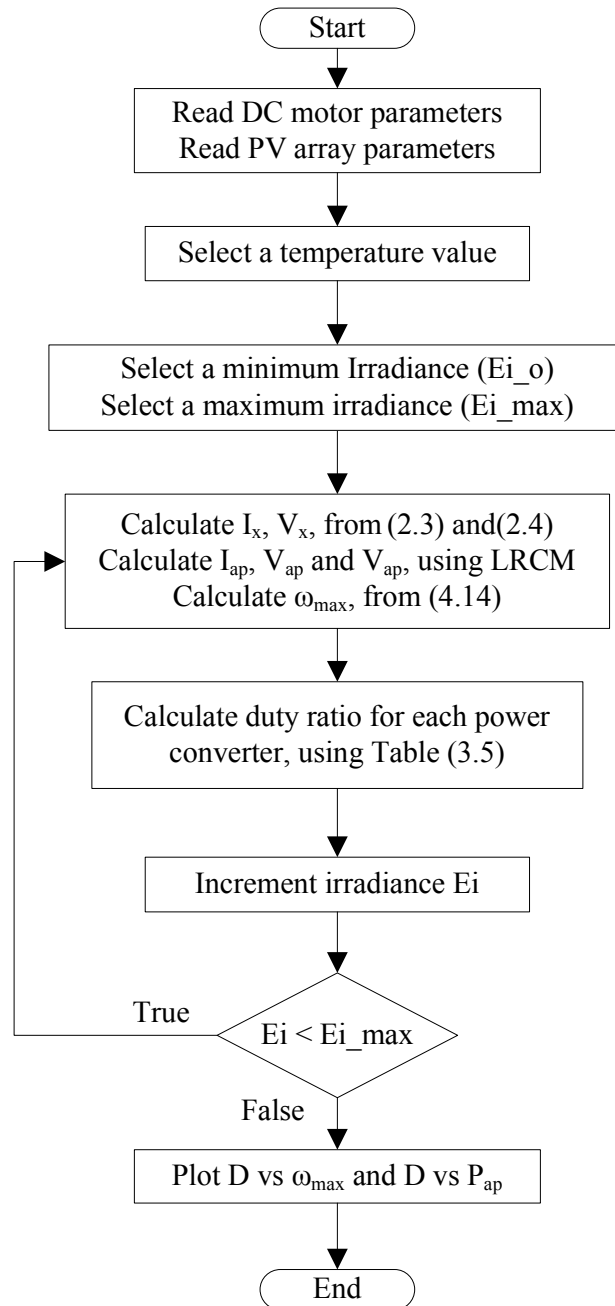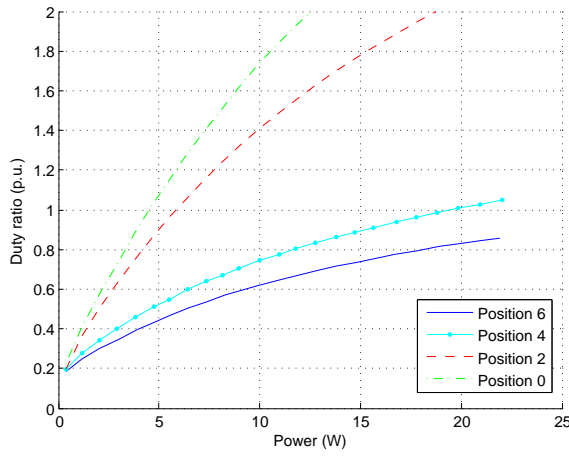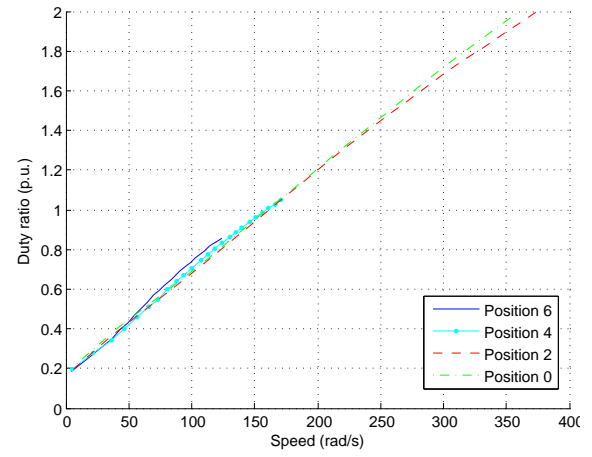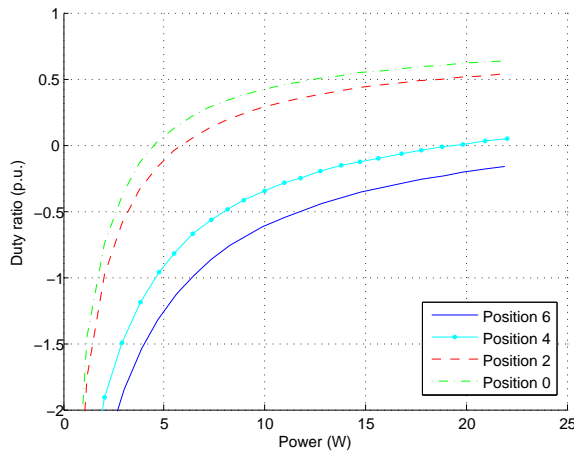$Ei < Ei\_max$

Plot D vs ω_{max} and D vs P_{ap}

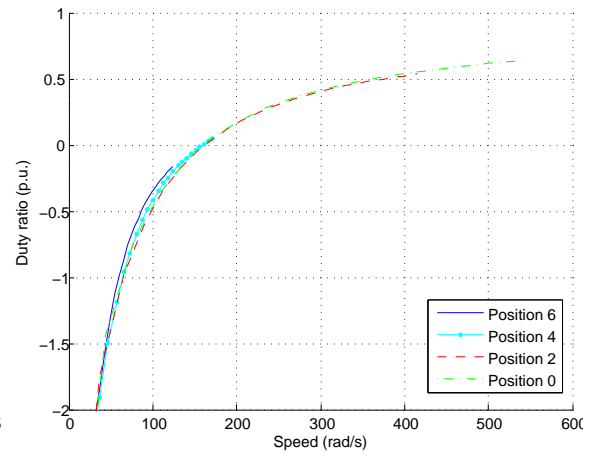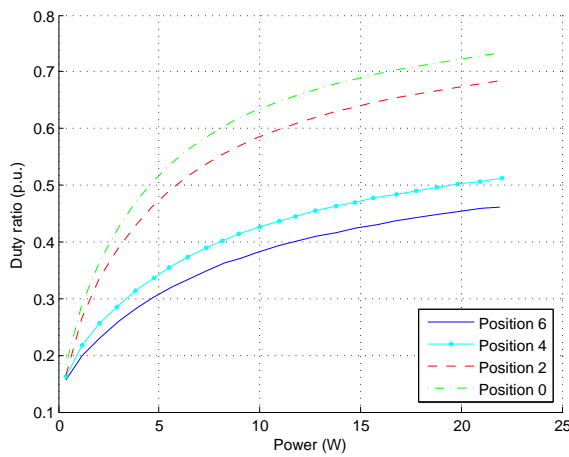Figure 5–1: Calculation of the duty ratio for irradiance variations
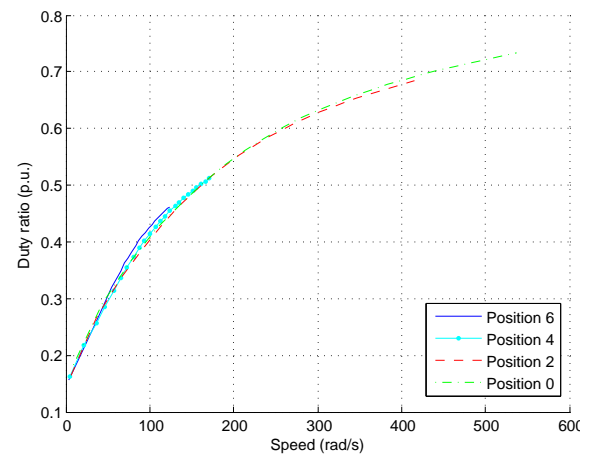
(a) step-down topology

(b) step-up topology

(c) step-down/step-up

Figure 5–2: Duty ratio vs Power for each studied topology

Figure 5–3: Duty ratio vs Speed for each studied topology

5.2 Tracking of maximum power with positive speed feedback

The previous section have described the procedure to obtain the relationship between the optimal duty ratio and the maximum motor speed, when a step-down converter is used. Also, it has been shown that the step-down converter is only suitable as an interface in an MPPT systems for the positions greater than position 4.

Then, we chose the position 5 of the braking magnet, whose torque-speed characteristic is given by $T_L = 0.00055\omega_m + 0.024$ (Position 5). For a temperature of $59°C$ and a set of irradiance values, we obtained V_{ap}, I_{ap} and P_{max} by LRCM for each irradiance values; also, the motor speed, ω_m, at P_{max} was calculated using (4.14) and the optimal duty ratio from (3.15). Figure 5–4 shows the variations of the optimal duty ratio D with ω_m, which describes the control law, it is given by $D = 0.0052\omega_m + 0.2$.
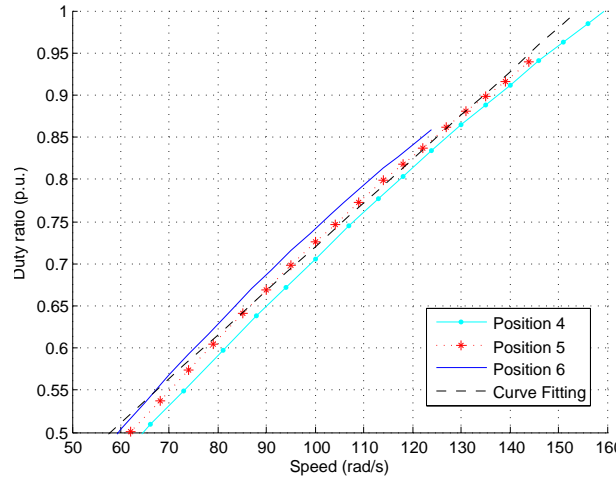

Figure 5–4: Duty Cycle vs Maximum Motor Speed

As was shown in Section 4.2 the control law $D = A + B\omega_m$ can be implemented using either analog or digital circuits. Then the simulation of this MPPT method is based on analog circuit using Synopsys's Saber® Simulator [54], where changes on irradiance can be executed [14], and switching models can be also used.

5.2.1 Simulation results

The PV array and the DC motor were modeled using the equations described in Chapter 2 and the parameters listed in Tables 3–1 and 3–3; while, the power converter was simulated using semiconductor switches.

The control law $D = 0.0052\omega_m + 0.2$ has been implemented using operational amplifiers, selecting the resistance values to attain the specified gains. A PWM chip, with $K_D = 1/3$ is used to generate the signal to activate the MOSFET according to the output operational amplifiers. A tachometer with constant $K_{th} = 0.0191\frac{V}{rad/seg}$ is used to sense the motor speed.

The system has been built in Synopsys's Saber$^{\circledR}$ Simulator [54] as shown in Figure 5–5. The simulation has been done during $0.8s$ for irradiance values of 600 W/m^2, $1050W/m^2$ and $900W/m^2$. Figure 5–6 shows the simulated DC motor speed and power of PVM, and Figure 5–7 shows simulated voltage and current of PVM. Table 5–2 summarizes the results comparing control and direct coupling.
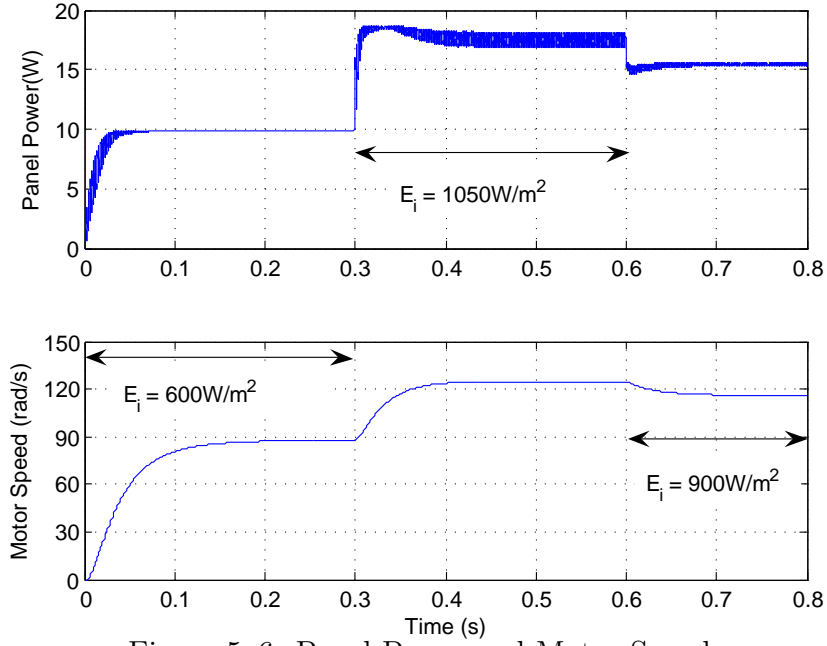

Figure 5–5: Circuit implemented

Figure 5–6: Panel Power and Motor Speed
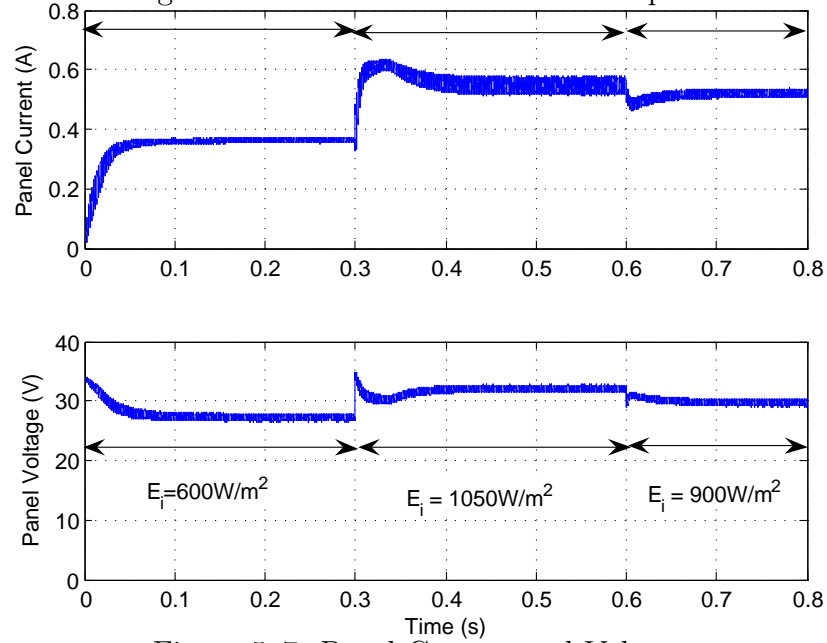

Figure 5–7: Panel Current and Voltage

Table 5–2: Summary of results of MPPT with feedback of speed

E_i	PVM Power [W]		
$[W/m^2]$	in MPP	With Control	With Direct Coupling
600	9.88	9.83	4.86
900	15.61	15.49	12.52
1050	18.68	18.57	17.14

5.2.2 Experimental results

The experiment setup is similar to the simulated scheme, so this consists of the DC motor and the PVMs specified in Tables 3–1 and 3–3. The control law was implemented through an operational amplifier chip (LM324) and a regulating pulse width modulator (PWM) chip (UC3526). Datasheets of LM324 and UC3526 can be found in Appendix H. The switching frequency has been fixed as 10 kHz with the external components connected to the PWM chip. The experiment setup is shown in figure 5–8.

In the test condition the PVM open-circuit voltage, $V_{oc} = 39.35V$ and the PVM short-circuit current, $I_{sc} = 0.71$; hence, the estimated maximum power is $P_{max} = 20W$. Figures 5–9, 5–10 and 5–11 are snapshots of the oscilloscope screen and show the experimental waveforms using a 10X probes.

Figure 5–9 shows the PWM signal applied to the MOSFET gate, its duty ratio is $D = 0.73$, the measured DC motor speed is $\omega_m = 104.18 rad/s$; this result agrees with the control law shown in figure 5–4. The DC motor armature voltage and the PVM voltage are shown in figure 5–10 and figure 5–11, respectively. The last one is $33.42V$ and the measured PVM current is $0.536A$; then, the PVM power is $17.91W$.
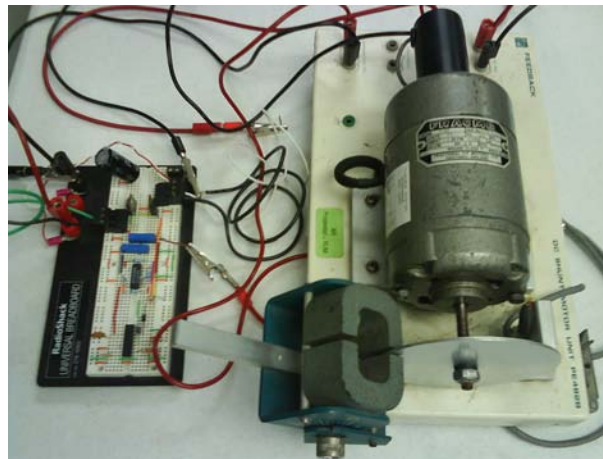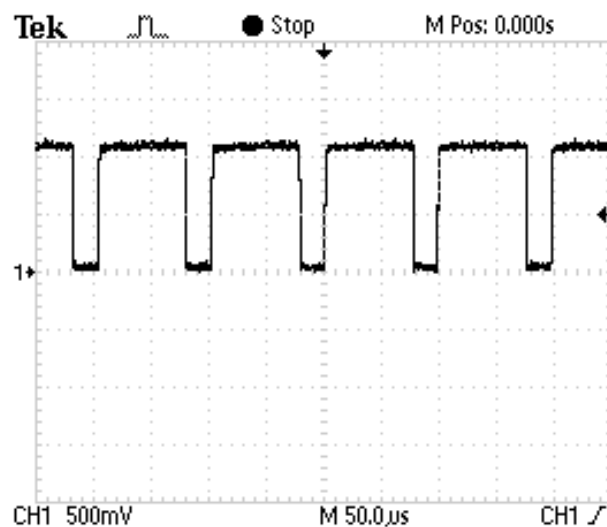

Figure 5–8: Experiment Setup

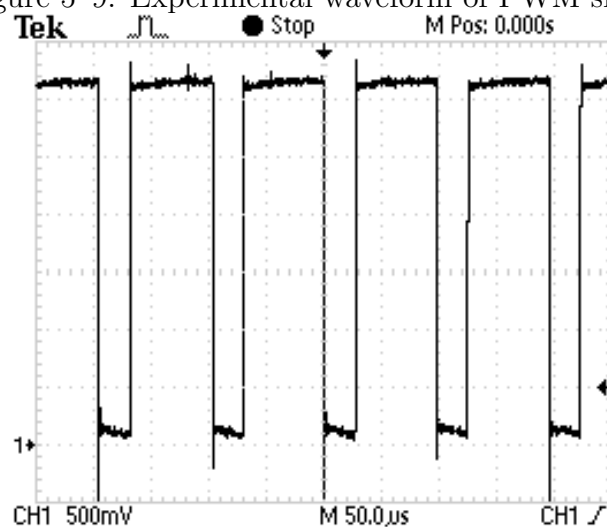Figure 5–9: Experimental waveform of PWM signal

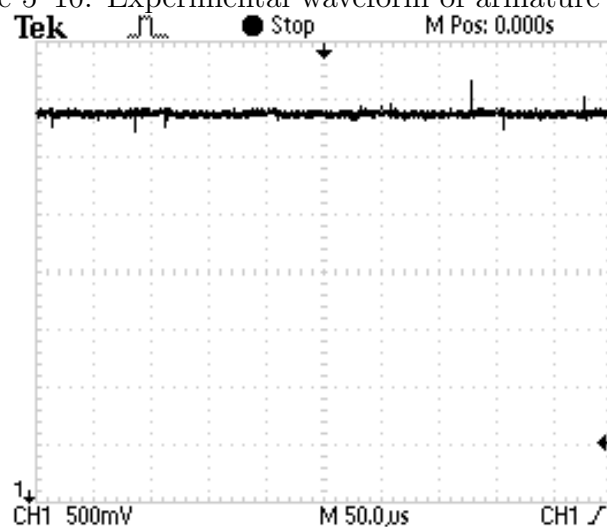Figure 5–10: Experimental waveform of armature voltage

Figure 5–11: Experimental waveform of PVM voltage

5.3 Developed system based on microcontroller and Buck-Boost converter

A block diagram of the fully developed system is shown in figure 5–12. In addition to the PV array and the DC motor, the system consists of three boards, whose design have been described in the previous chapter. The architecture with three boards gives flexibility and versatility; with the update of the microcontroller program the MPPT method can be changed; likewise, the power converter can be substituted by another circuit with a different topology.

The PV sensing board (Figure 5–13(c)) includes the sensing circuits and a MOSFET; this MOSFET disconnects the PV array from the power converter to measure the open-circuit voltage. The microcontroller board (Figure 5–13(a)) contains the ATmega88 and an interface to send data to a serial port. The converter board (Figure 5–13(b)) is composed of the power converter and the MOSFET driver.

In order to avoid restriction on both the load connected to the motor and environmental conditions, a Buck-Boost converter has been chosen. Previous results have demonstrated that a Buck-Boost converter can always reach the maximum power, without relying on the kind of the load or the irradiance value.
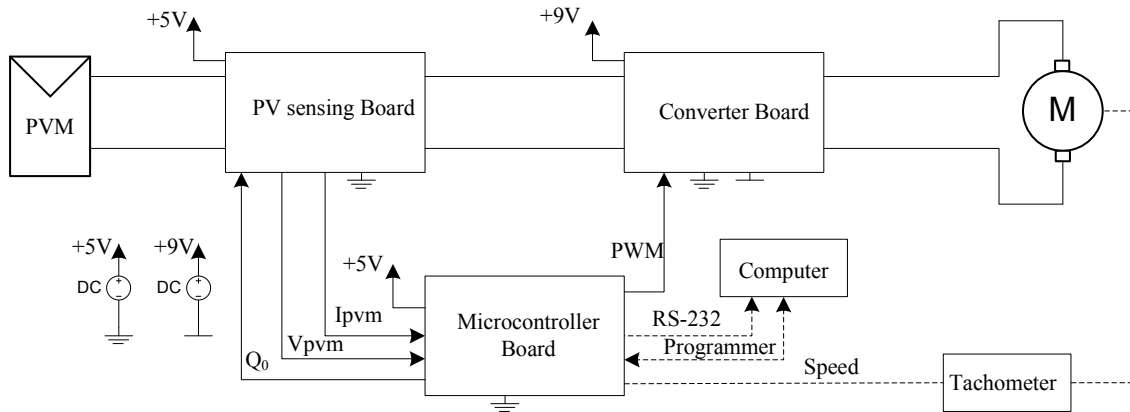
Figure 5–12: Block Diagram of the developed system
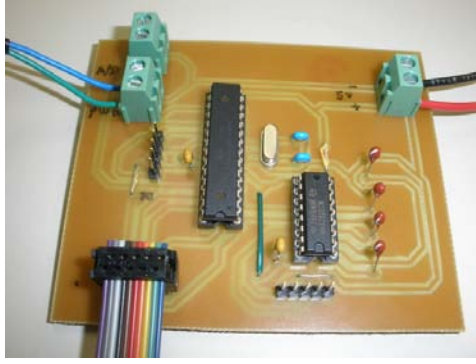
(a) Microcontroller board
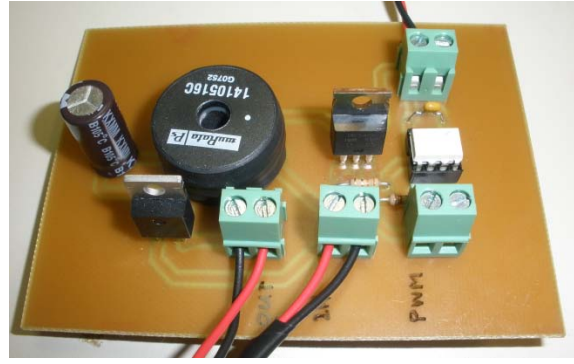
(b) DC-DC converter board

(c) PV sensing board

Figure 5–13: Picture of built board

The experimental setup is shown in Figure 5–14 and the PV array is shown in Figure 5–15. This setup is used to implement the studied MPPT methods: Linear Reoriented Coordinated Method (LRCM), Perturbation and Observation (P&O), and INcremental Conductance (INC).

All the methods have been tested in real environment conditions. The irradiance have been measured with a pyranometer LI-200 from LI-COR®and the PVM temperature have been measured with a multimeter FLUKE®289 through its type K thermocouple.

Load torque variations have been considered for each MPPT method. The load torque have been modified by changing the position of the braking magnet of an eddy current brake. The corresponding braking torque values for the positions 3, 4, 5, and 6 are giving in Table 5–1.
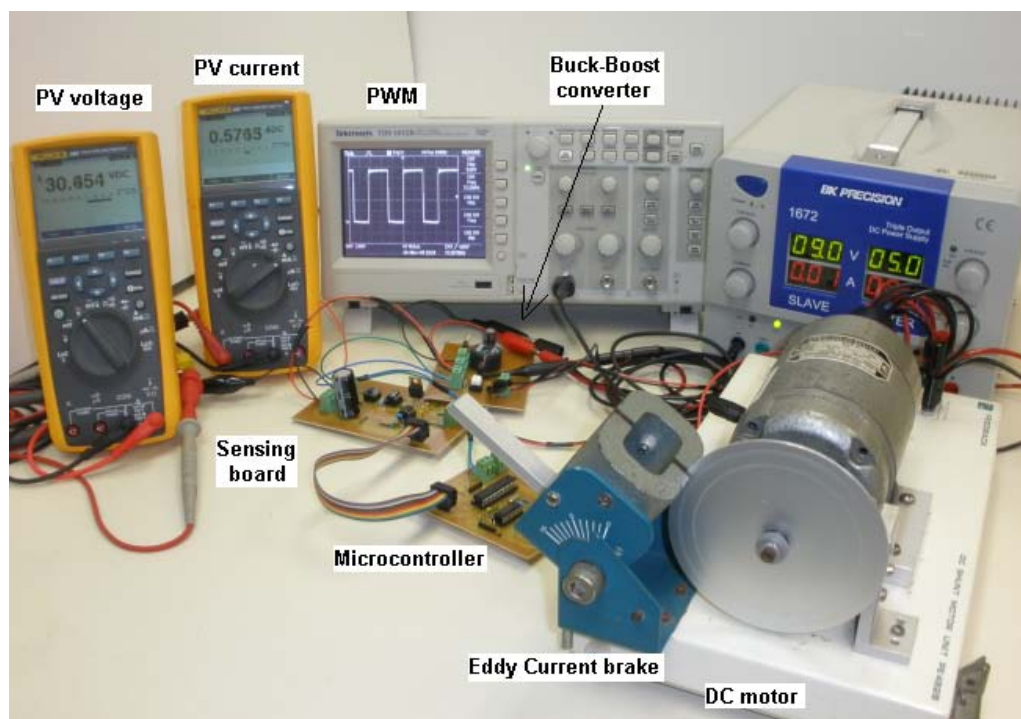
Figure 5–14: Experiment setup

Figure 5–15: PV array

5.4 Tracking of maximum power with LRCM

As was described in previous chapters, the LRCM can derive an approximated optimal voltage (V_{ap}), which is used as set point in a control loop. A PI controller adjusts the duty ratio of a power converter until the PVM voltage becomes V_{ap}. Therefore, the PVM will operate around the maximum power point.

5.4.1 Simulation results

The simulation of the system was developed using MATLAB/Simulink® [47] as shown in Figure 5–16; where the PVM, the DC motor and the power converter has been modeled using the mathematical models described in Chapter 2. Likewise, The LRCM method has been modeled using Equation (2.5).

The simulation was run by running the *mfile*: `PVBuckBoostMotorSim.m` (Appendix E) from the MATLAB command line. This *mfile* loads the simulations parameters and sets the simulation time. One of the options of the Simulink® models is the numerical integration algorithm; all the simulation results have been done using the Dormand-Prince method.
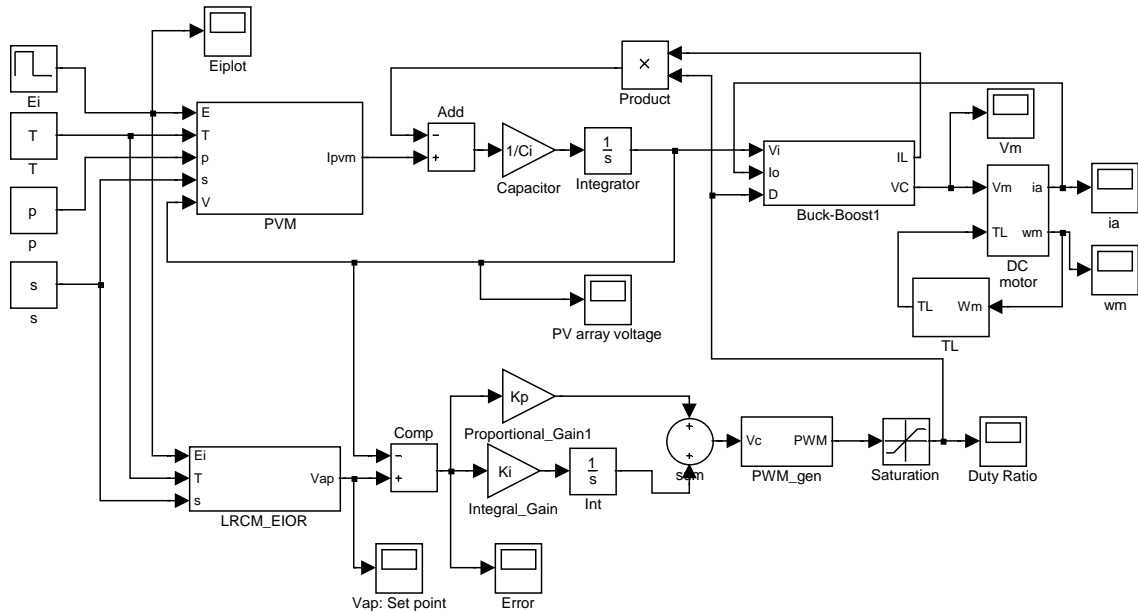
Figure 5–16: Simulink model of MPPT using LRCM

Because of the difficulty for finding the constant K_p and K_i of the controller, variations of each constant are tested in order to obtain a stable response with zero error in steady-state. Thus, the values of K_p and K_i can be set in the *mfile*: PVBuckBoostMotorSim.m (Appendix E).

In Figure 5–17 is shown the response of the PV array voltage for different K_p values; the values of K_p are 0.5(blue), 1(green) and 10(magenta). The set point (red) changes according to irradiance variations. Increasing K_p, the PV array voltage approximates to the set point. The error is shown in upper part of figure 5–18, while the duty ratio is shown in lower part of the same figure.

The response of the PV array voltage for different K_i values is shown in Figure 5–19; the values of K_i are 1(green), 5(yellow) and 10(magenta). Likewise the K_p variations, the set point (red) changes according to irradiance variations. The response is slow with $K_i = 1$, while the response oscillates with $K_i = 10$. Therefore, the response with $K_i = 5$ has smaller error, as can be seen in upper part of figure 5–20. The duty ratio for each case is shown in the lower part of figure 5–20.
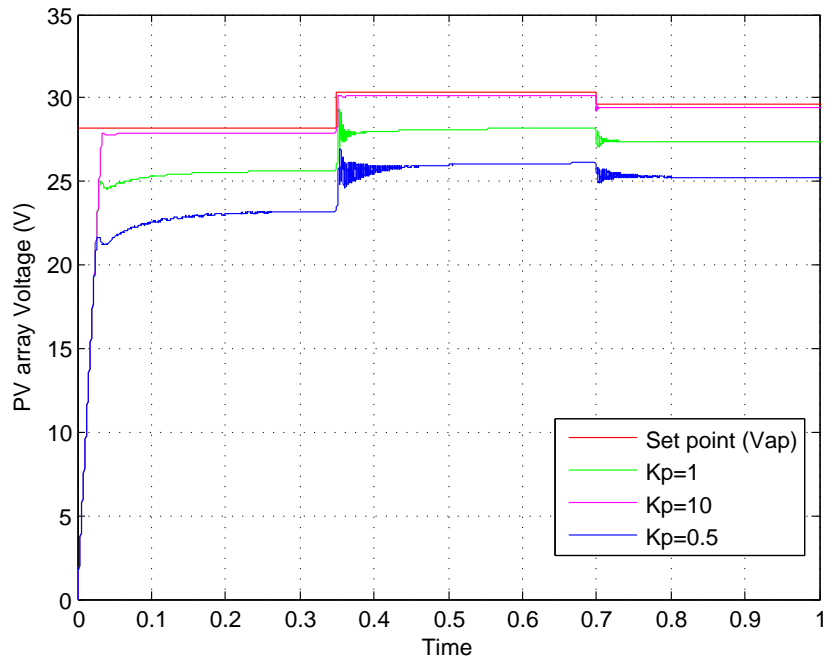
Figure 5–17: Tracking of Optimal Voltage (red) for different K_p values
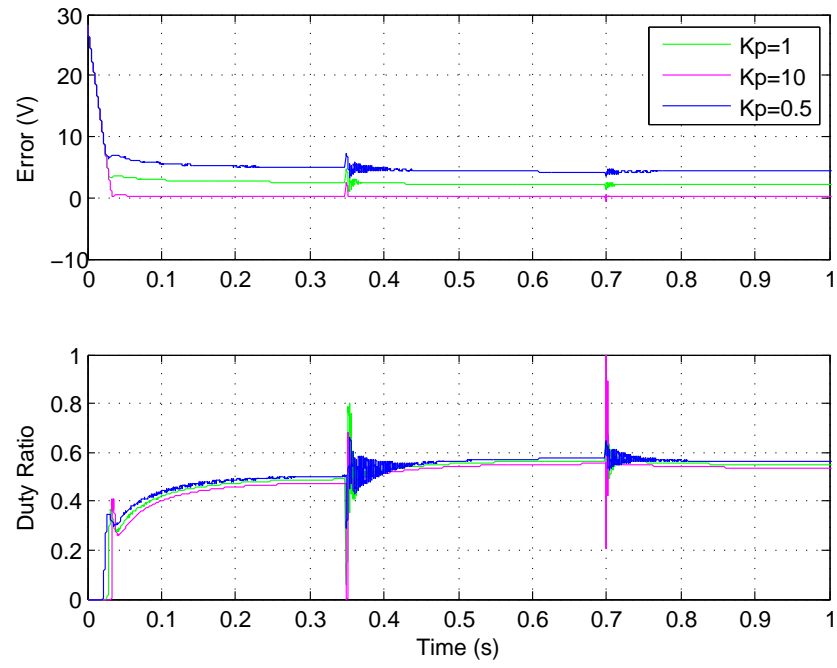
Figure 5–18: Tracking error and duty ratio for different K_p values
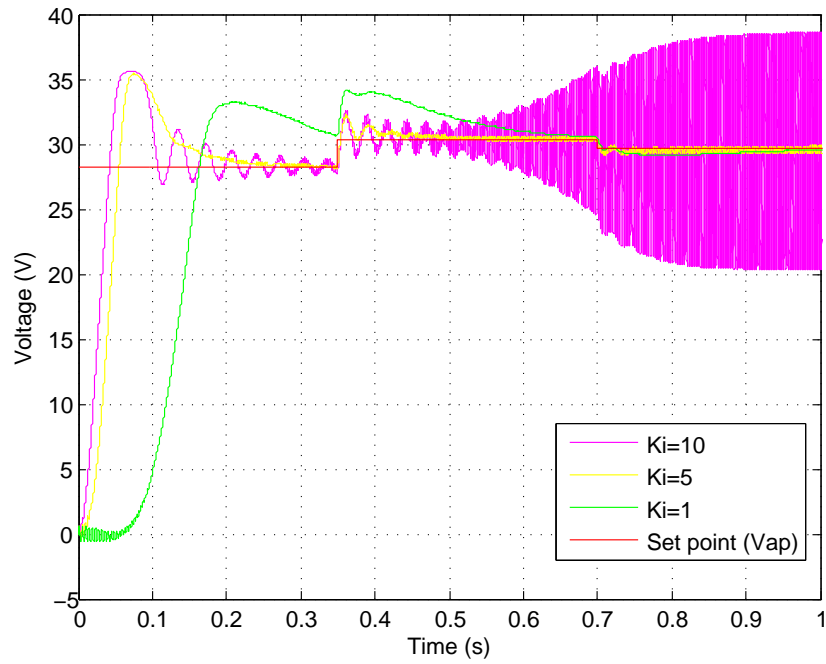
Figure 5–19: Tracking of Optimal Voltage (red) for different K_i values
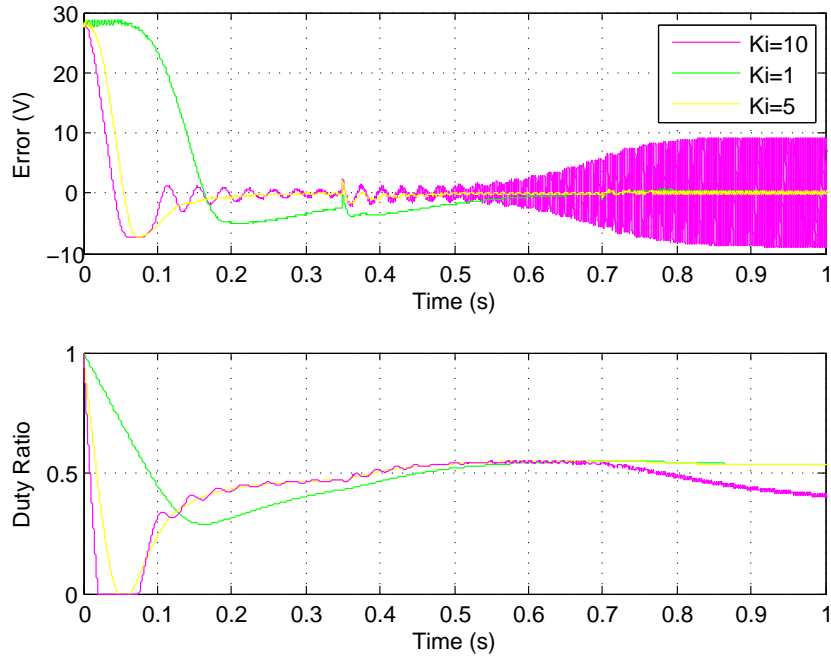
Figure 5–20: Tracking error and duty ratio for different K_i values

5.4.2 Experimental results

The experimental setup for LRCM is similar to the setup previously shown in Figure 5–14. The LRCM have been tested for environmental variations and for load variations. The environmental variations affect the open-circuit voltage and the short-circuit current of PVM. The load variations are carried out by changing the position of the braking magnet as has been explained previously.

Figure 5–21 shows the PVM power for different values of short-circuit current and open-circuit voltage (i.e. different irradiance and temperature values). This figure allows to compare the measured value with the theoretical value for each condition.

The method was also tested in real weather conditions under load variations. The position of the braking magnet was changed in order to modify the load characteristics. The systems started with the braking magnet in the position 3; the
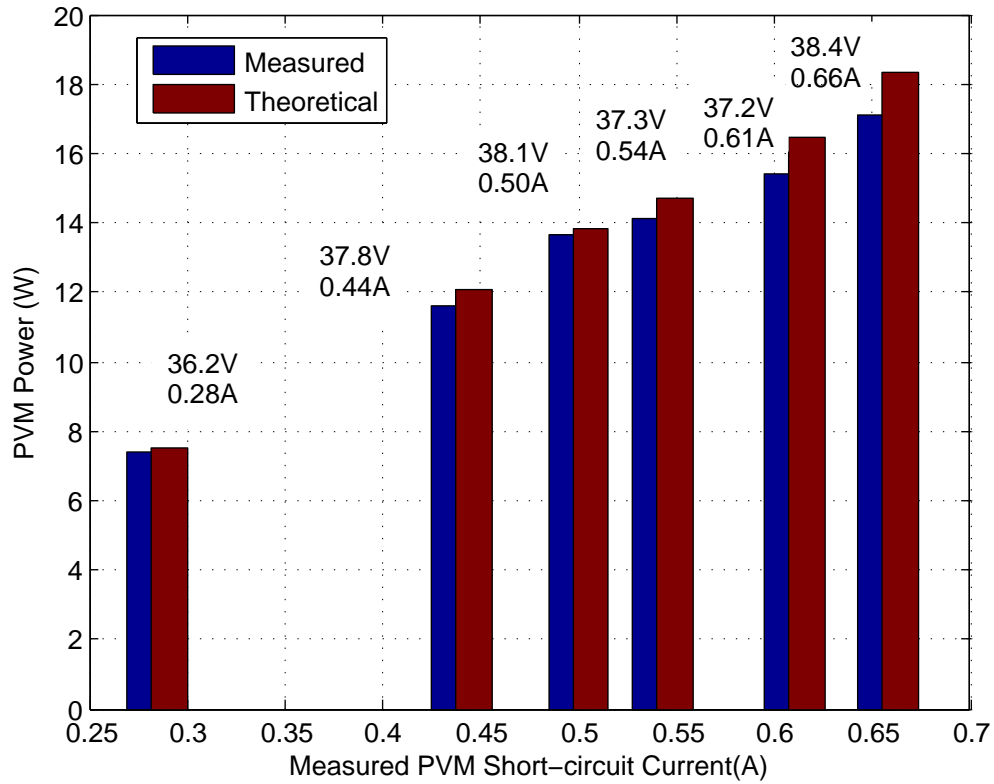
Figure 5–21: Digital MPPT with LRCM

position was modified each 25 seconds approximately, following the sequence: Position 3, position 5, position 4 and position 6.

Figures 5–22, 5–23 and 5–24 show the experimental results with an average value of irradiance equals to $1134W/m^2$. In spite of the variations of the load, the PV array kept providing the same power ($15.6W$). The controller adjusted the duty ratio, keeping the PV array operating around of the maximum power point; while the motor speed changed according to the load characteristics.

Figure 5–24 shows the PV array voltage and the PV array current; where the effect of the disconnection of the PV array can be seen each 2 seconds in order to measure the open-circuit voltage. This effect is also shown in the power graph.
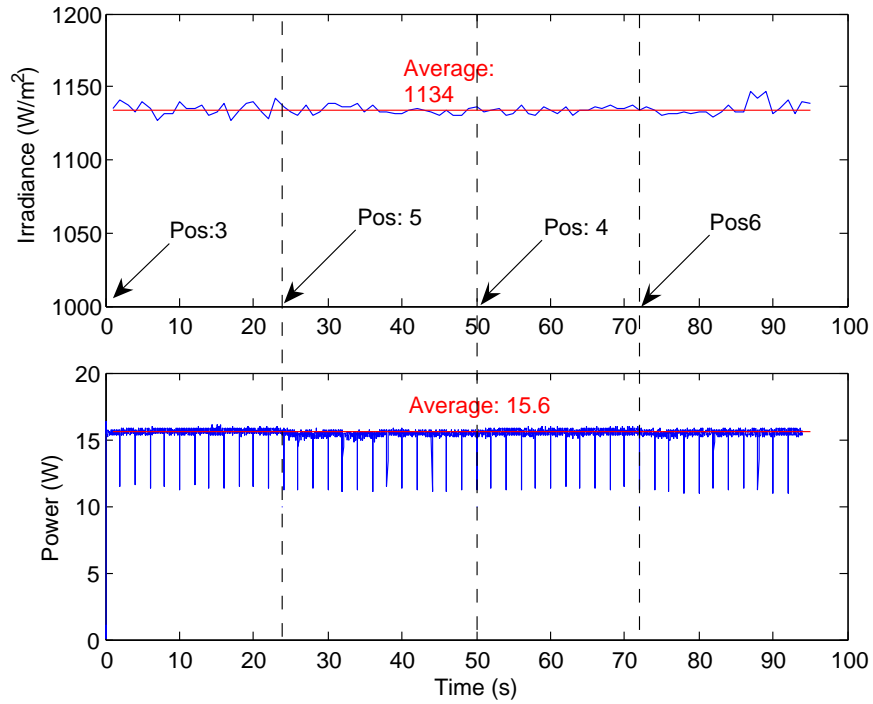
Figure 5–22: Experimental Irradiance and PVM power for LRCM
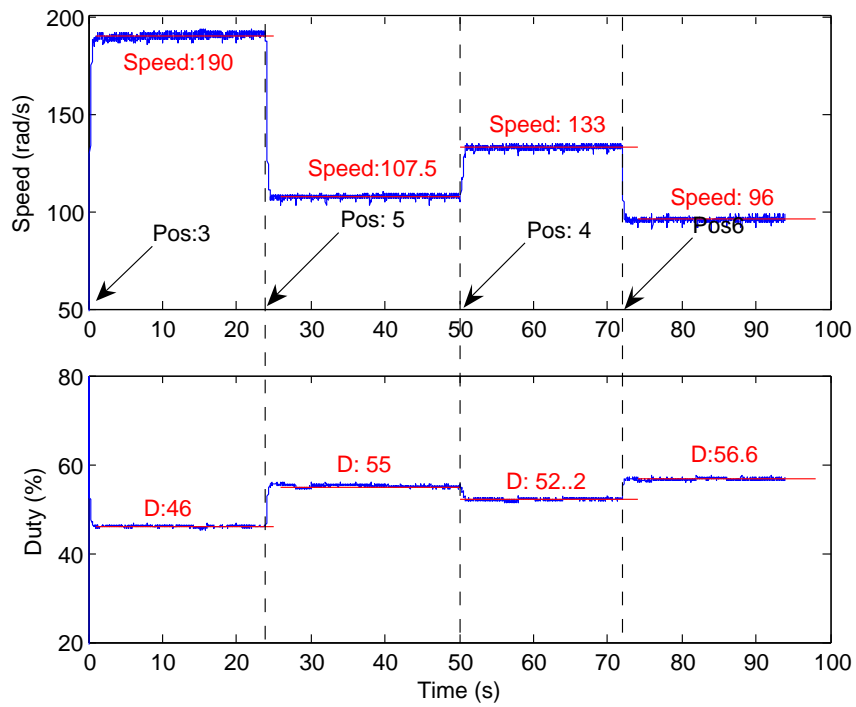
Figure 5–23: Experimental motor speed and duty ratio for LRCM
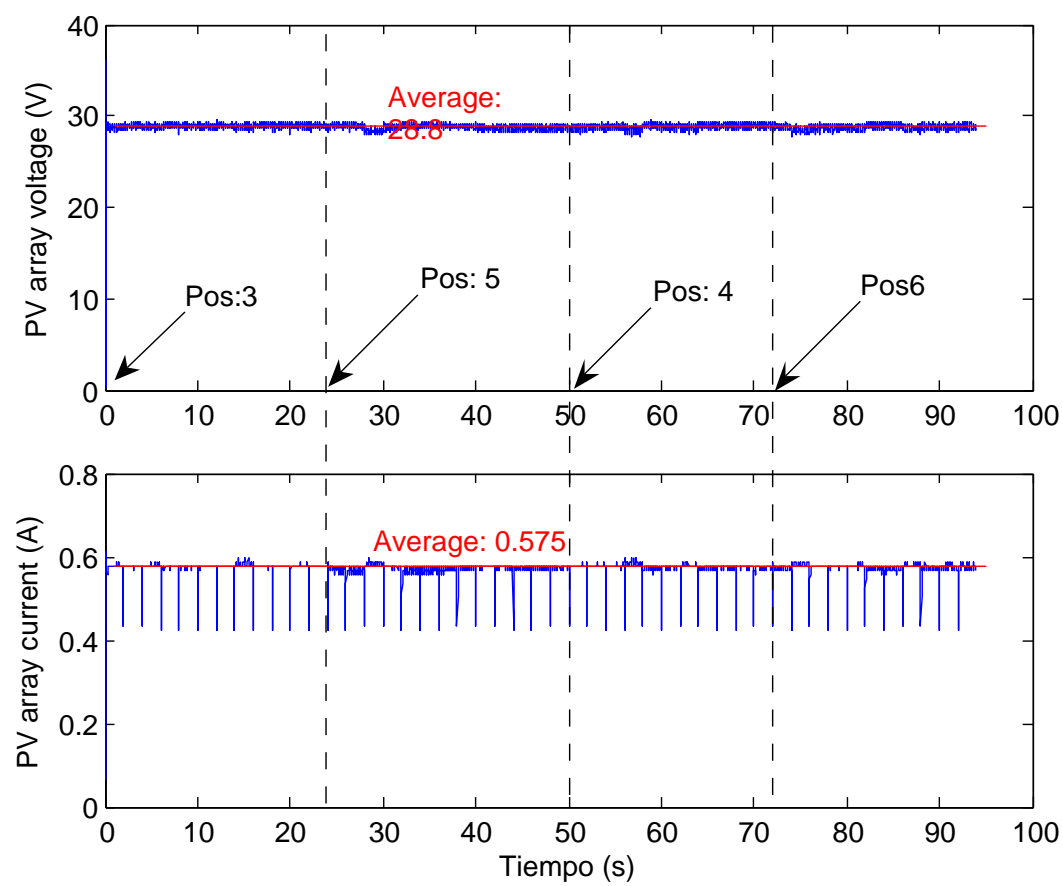
Figure 5–24: Experimental Voltage and Current of PV array with LRCM

5.5   Tracking of maximum power with searching algorithm

Searching algorithm as Perturbation and Observation (P&O) and INcremental Conductance (INC) were implemented and tested for different load variations and irradiance variations. Simulation and experimental results are presented below.

5.5.1   Simulation Results of P&O

The proposed scheme with Perturbation and Observation was simulated using Simulink. The block diagram developed is shown in figure 5–25, while figure 5–26 shows the details of the Perturbation and Observation block, which is based on [55].

The PVM, the DC motor and the power converter were modeled using the mathematical models described in the chapter 2. The parameters used are loaded running the *mfile*: `PVBuckBoostMotorPandOSim.m`, which is shown in appendix E.
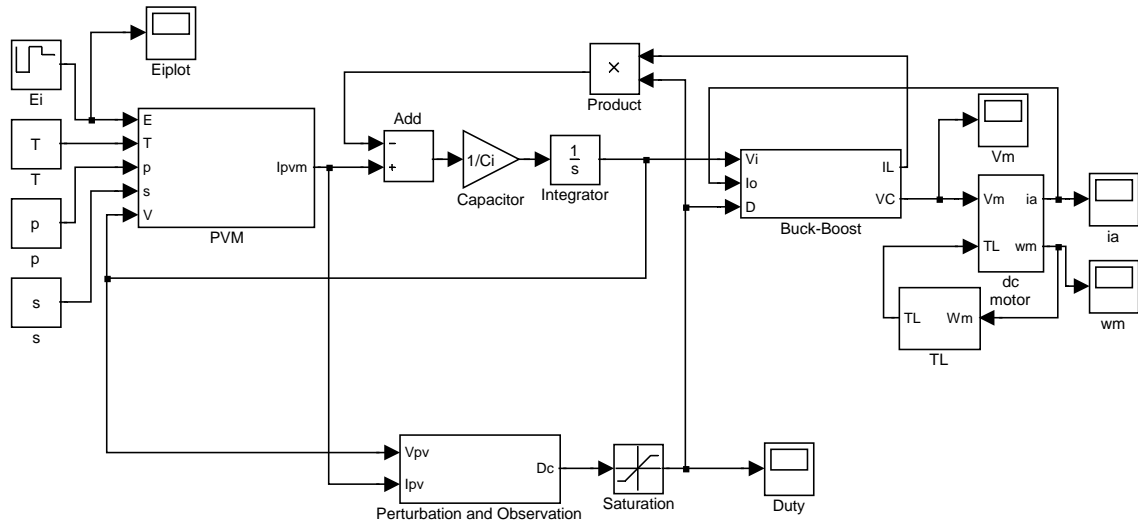
Figure 5–25: Simulink model of P & O method
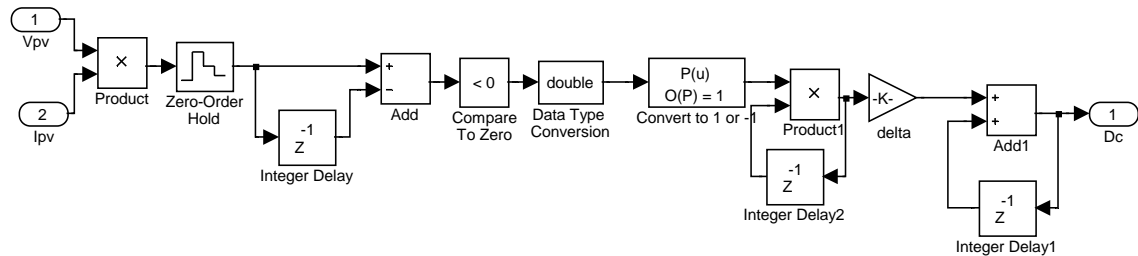
Figure 5–26: Details of Perturbation and Observation block

Figure 5–27 shows the simulation results considering variations of the irradiance; this simulation was carried out for the braking magnet in position 5 during 30 seconds, and the temperature value was 59°. The initial value of irradiance was $600W/m^2$; later, the irradiance changed at $t = 10s$ to $1050W/m^2$ and at $t = 20s$ to $900W/m^2$.

The P&O method tracked the maximum power successfully for all the irradiance values; however, the PV power had a small oscillation. Table 5–3 summarizes the results of P&O method, showing the minimum and maximum value of the fluctuation of PVM power. In order to evaluate the effectiveness of the method, the PVM power in the Maximum Power Point (MPP), for the two PVMs SX10M connected in series, at the same irradiance and temperature values.

Table 5–3: Simulation results of P&O method for different irradiance values

Irradiance	Min. PV power	Max. PV power	Power in MPP
$600W/m^2$	9.4	9.88	9.88
$900W/m^2$	14.5	15.6	15.6
$1050W/m^2$	17.4	18.68	18.68

5.5.2 Experimental Results of P&O

The Perturbation and Observation method was tested in real weather conditions under load variations. The irradiance was changing between $1100W/m^2$ and $1130W/m^2$. Different load characteristics were examined by modifying the position of the braking magnet. This position was changed every 30 seconds approximately, starting in the position 3, alternating to the position 5, later changing to the position 4 and finally moving toward the position 6.

Figure 5–28 shows the variations of the irradiance, PV array power, motor speed and duty ratio for the conditions explained. The PV array power is around $16.16W$ for all the load conditions. The duty ratio has a ripple of 4%; this is because the
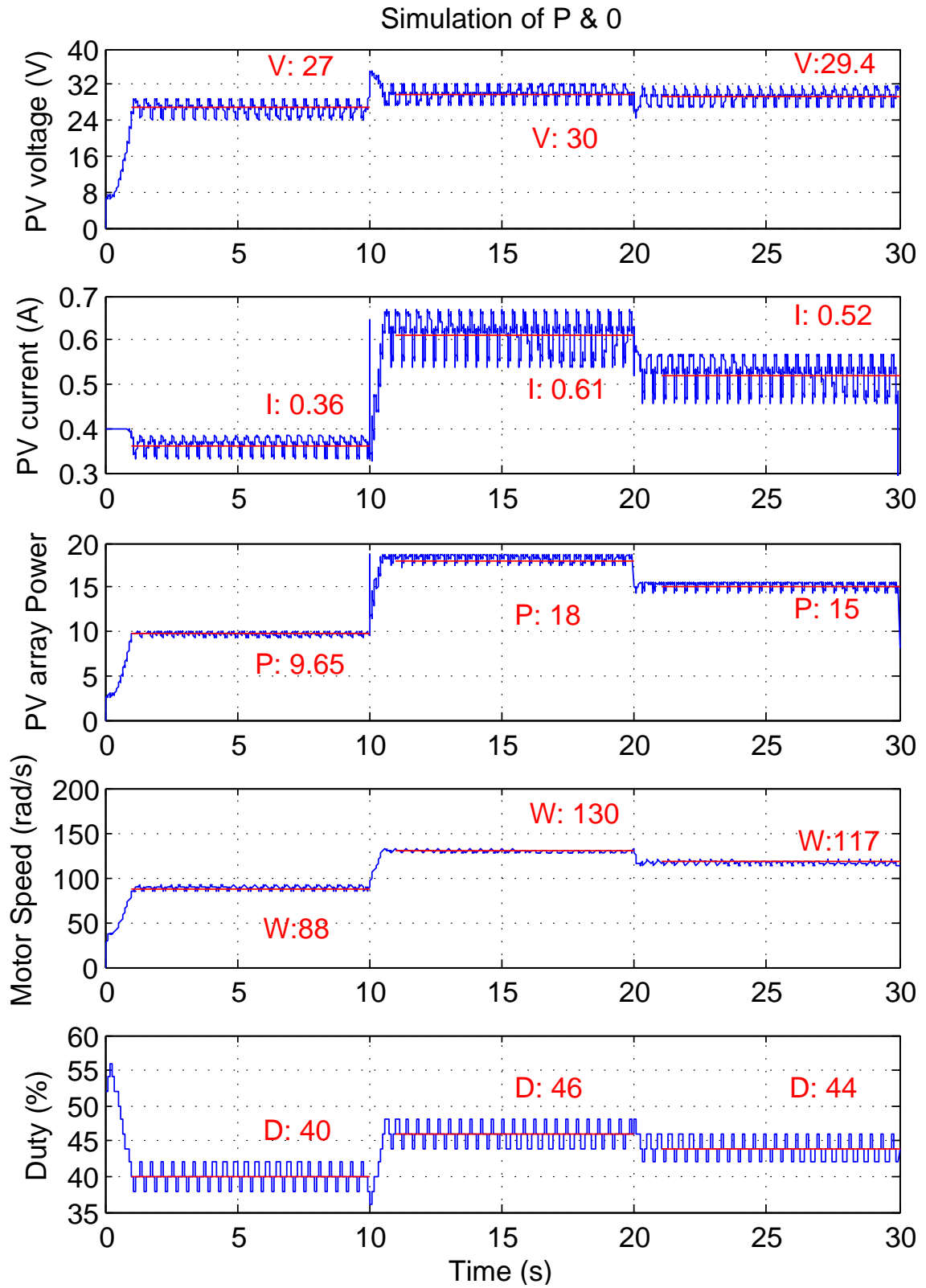
Figure 5–27: Simulations results for irradiance variations

step size was 2%. Figure 5–29 shows the motor speed and the duty ratio of the pwoer converter.

With the conditions described previously, the PV array voltage and the PV array current are shown in figure 5–30. The voltage oscillated between $26V$ and $29V$ with a small reduction between 30 seconds and 60 seconds. The current is also oscillatory, fluctuating between $0.54A$ and $0.6A$.
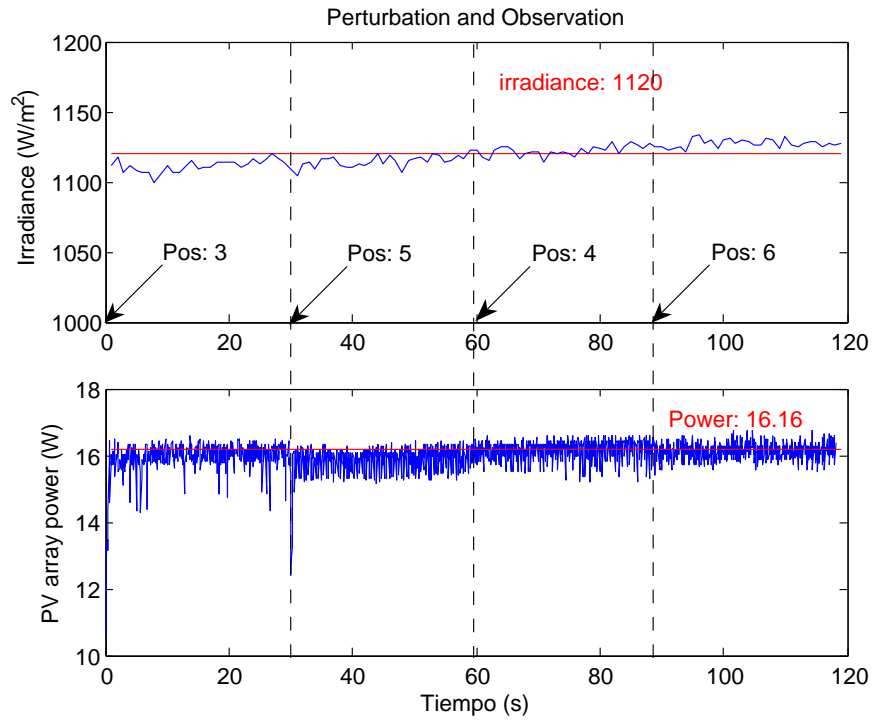
Figure 5–28: Experimental results of P&O
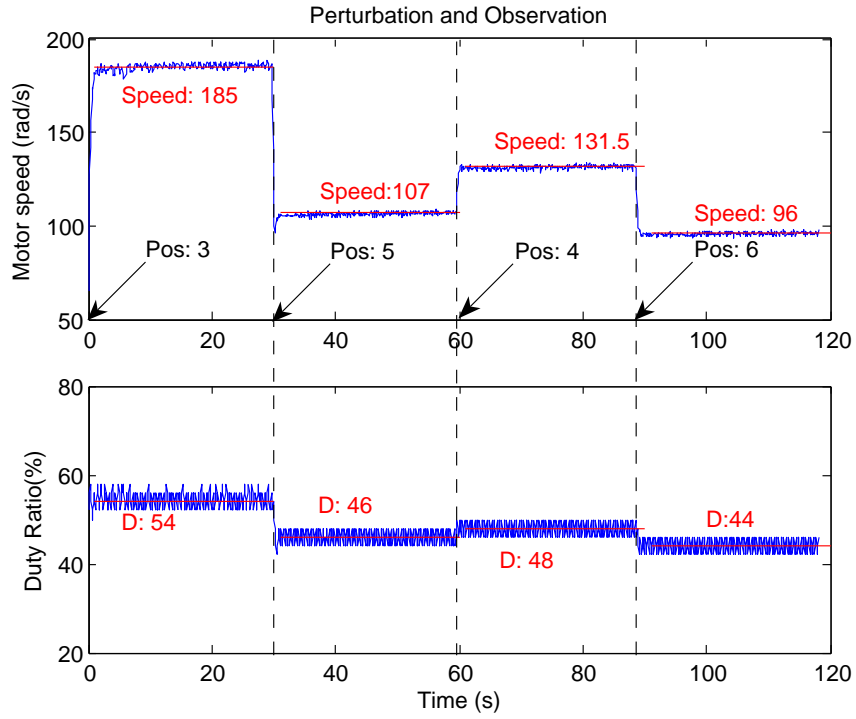
Figure 5–29: Experimental motor speed and duty ratio with P&O
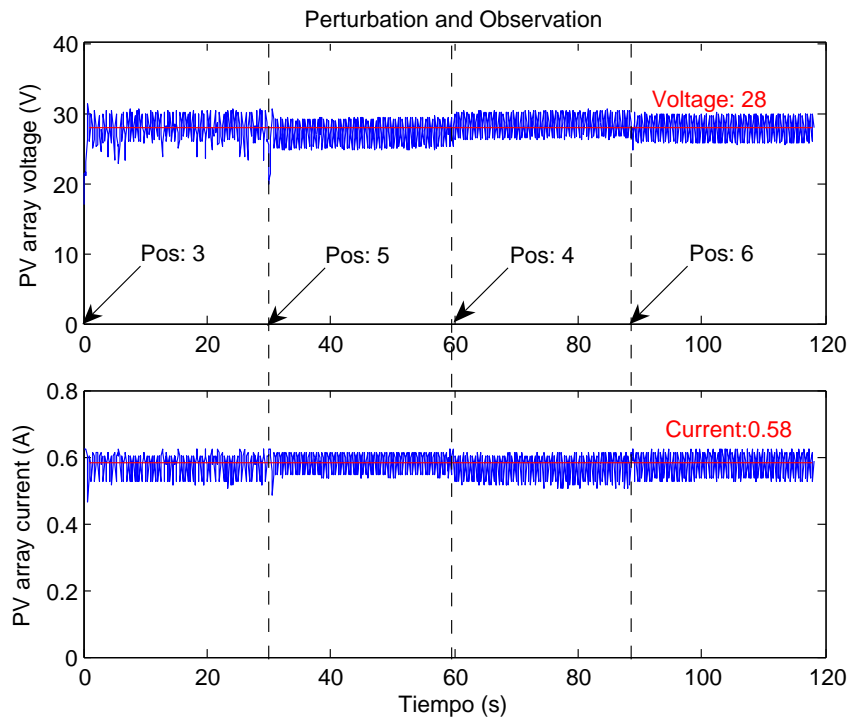
Figure 5–30: Experimental Voltage and Current of PV array with P&O

5.5.3   Experimental Results of INC

The INcremental Conductance (INC) method was also implemented using the developed system described formerly and shown in 5–12. Similarly to the LRCM and P&O methods, the INC method was tested in real weather conditions for different loads. The load was modify through the change of the braking magnet position, changing from the position 3 to the position 5, from there to the position 4 and finally to the position 6.

During the test the irradiance received by the PV array was changing from $1075W/m^2$ to $1060W/m^2$. Despite of the load variations, the PV array kept supplying $16.08W$ to the motor. The oscillations of the PV voltage and PV current are shown in figure 5–33. The irradiance and the PV array power, as well as the motor speed and the duty cycle are shown in figure 5–31. In this case the variations of the duty ratio also correspond the step size, a ripple of 2% and a step size of 1%.
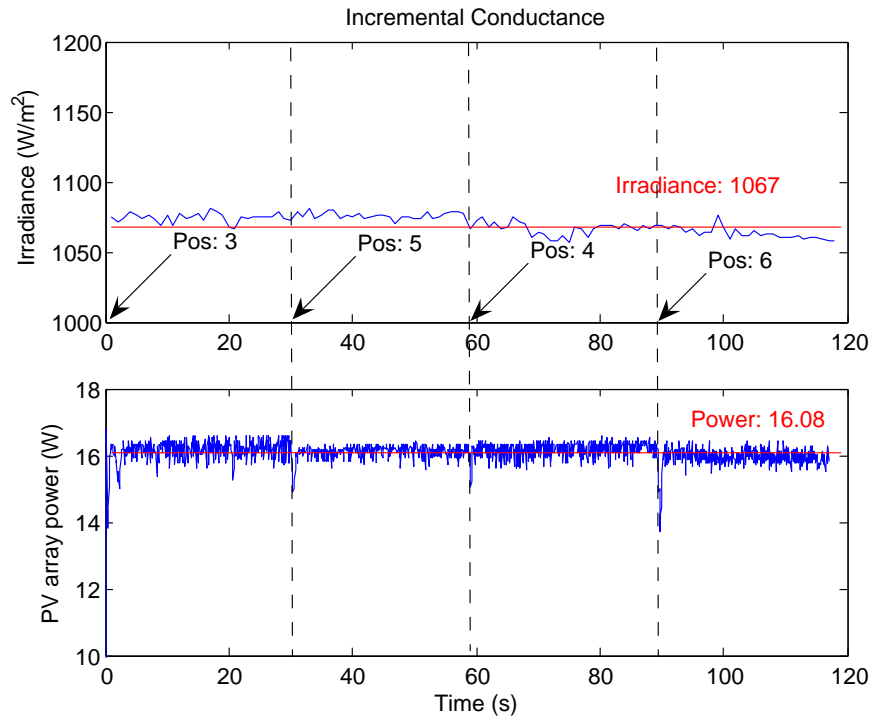
Figure 5–31: Experimental results of INC
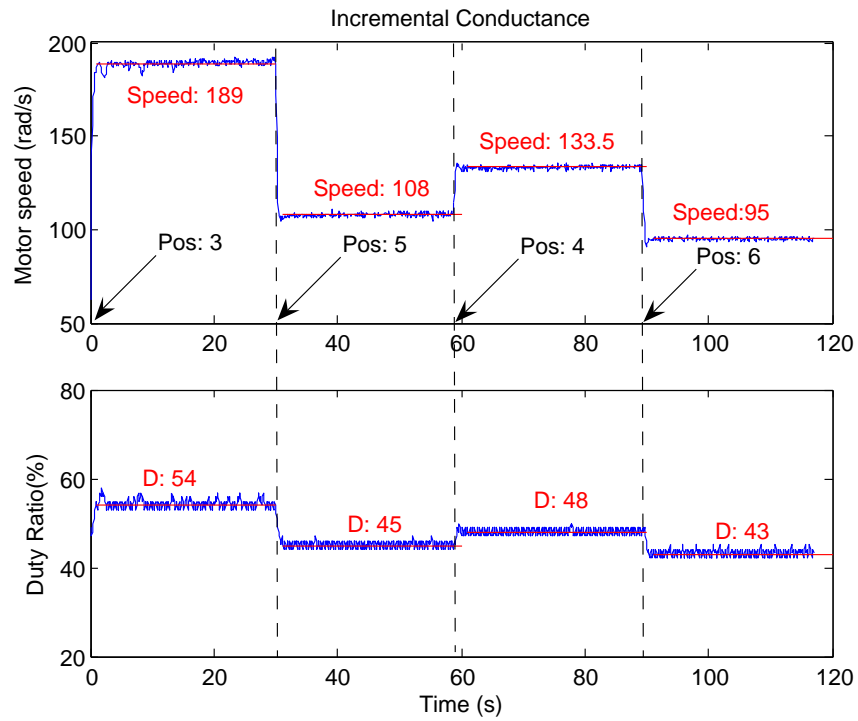
Figure 5–32: Experimental motor speed and duty ratio with INC
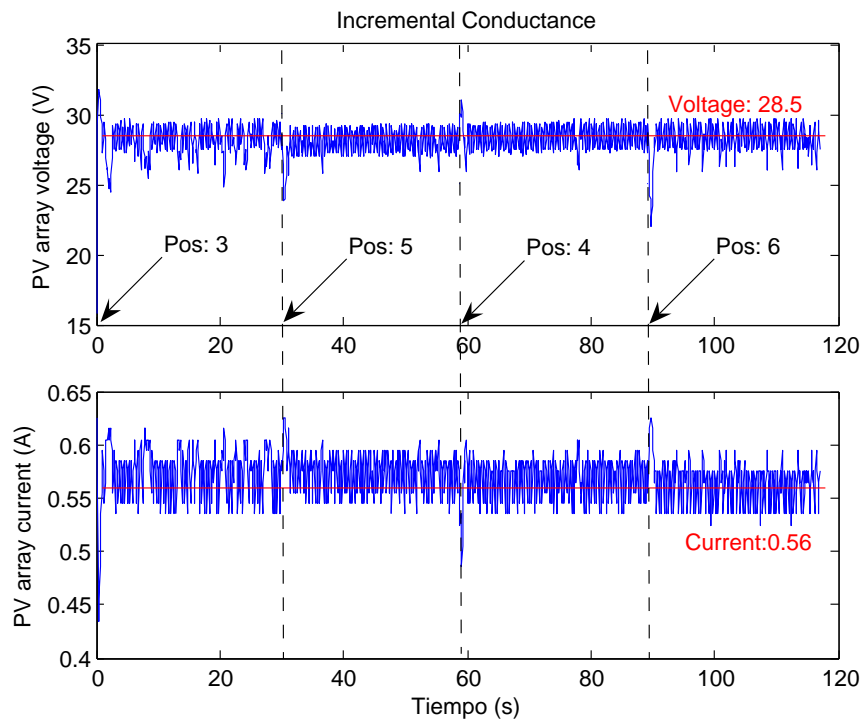
Figure 5–33: Experimental Voltage and Current of PV array with INC

5.6 Summary of results

A comparison between basic topologies of power converter was presented. The relationship between optimal duty ratio and maximum power was showed for the analyzed system. As a result, it was possible to determine the topologies that are suitable for extract the maximum power of the PVM for some load conditions.

An MPPT method based on the DC motor speed was designed, showing the simulations and the experimental results. These method used a step-down converter and had restriction with some load conditions, which was explained with the comparison of the topologies.

The designed system allowed the digital implementation of model-based MPPT methods and searching MPPT methods. These methods were tested in real weather conditions with different load variations, showing the experimental data that include voltage and current of the PV array, solar irradiance, DC motor speed and duty ratio of the power converter. In addition, software simulation was carried out.

Table 5–4 shows a summary of the main results of each method. In addition of the measured open-circuit voltage (V_x) and the short-circuit current (I_x), the estimated maximum power (P_{ap}), the approximated optimal voltage (V_{ap}) and the approximated optimal current (I_{ap}) are also shown.

In order to evaluate the performance of each MPPT method, the tracking efficiency is calculated and showed in Table 5–4. The tracking efficiency is defined as the ratio between the measured PVM output power (P_{PVM}) and the estimated PVM maximum power (P_{ap}), i.e. $\eta_{MP} = \dfrac{P_{PVM}}{P_{ap}}$.

Table 5–4: Summary of experimental results for MPPT methods

Method	V_x	I_x	P_{ap}	V_{ap}	I_{ap}	P_{PVM}	η_{MP}
LRCM	36.81	0.658	17.57	29.15	0.608	16.67	0.9487
P & O	37.13	0.639	17.21	29.41	0.58	16.16	0.9393
INC	37.42	0.624	16.94	29.64	0.571	16.06	0.9485

Chapter 6

Conclusions

A method to compare the power converters and to choose a suitable topology for obtaining the maximum power of a PVM feeding a DC motor has been presented. Step-down (Buck) power converters have some limitations for matching a PVM to a DC motor. These power converters only can extract the maximum power for small values of irradiance and for large values of load torque. Step-down/step-up (Buck-Boost) power converters have no restriction for matching a PVM to a DC motor. There is always a duty ratio for such topologies that can extract the maximum power of a PVM.

The positive speed feedback MPPT method does not work in the true maximum of the PVM; however, the mathematical relationship can easily be implemented with step-down power converters either an analog or digital form to track power closer to the maximum value.

The LRCM can achieve the maximum power point faster that MPPT searching algorithms. However, this method requires fine tuning due to changes on the PVM parameters.

MPPT searching algorithms are more practical than model-based MPPT methods. Such algorithms do not require tuning due to parameter variations by aging or dusty environment of the PVM. The fluctuation of the PVM voltage seems a disadvantage of searching method. However this fluctuation has little effect on the

DC motor speed. Thus, MPPT searching algorithms are recommended for real applications.

An inexpensive, modular and flexible system has been developed, which can be used to implement several Maximum Power Point Tracking methods by updating the microcontroller program. Both model-based MPPT methods and MPPT searching algorithms can track the maximum power point for load torque variations.

6.1   Future work

The MPPT methods could be simulated and implemented for centrifugal load, where the load torque is proportional to the speed. Moreover, speed regulation could be implemented, analyzing the power characteristic in order to determine which region of operation is more suitable.

Is recommended to design the power conditioning that allows to supply the field winding of a separately excited DC motor using a PV array. Thus, the characteristics of a permanent magnet could be achieved from a separately excited DC motor.

The relationship between optimal duty ratio and maximum power were obtained considering Continuous Conduction Mode (CCM); it would be useful to develop the analysis when the power converter works in Discontinuous Conduction Mode (DCM).

The MPPT method based on positive feedback of speed is based on 100% efficiency; therefore this assumption causes errors on the operation around the maximum power point. Thus, an evaluation of the efficiency of the power converter is recommended to explain this issue.

References

[1] Michaell Ropp. *Encyclopedia of Energy Engineering and Technology*, volume 3, chapter Photovoltaic Systems, pages 1147–1159. CRCPress: Taylor and Francis Group, LLC, 2007.

[2] Gilbert Masters. *Renewable and Efficient Electric Power Systems.* John Wiley & sons, Inc., 2004.

[3] S.M. Alghuwainem. Steady-state performance of dc motors supplied from photovoltaic generators with step-up converter. *Energy Conversion, IEEE Transaction on*, 7(2):267–272, Jun 1992.

[4] S.M. Alghuwainem. Matching of a dc motor to a photovoltaic generator using a step-up converter with a current-locked loop. *Energy Conversion, IEEE Transaction on*, 9(1):192–198, Mar 1994.

[5] W.Z. Fam and M.K. Balachander. Dynamic performance of a dc shunt motor connected to a photovoltaic array. *Energy Conversion, IEEE Transaction on*, 3(3):613–617, Sep 1988.

[6] M.M. Saied. Matching of dc motors to photovoltaic generators for maximum daily gross mechanical energy. *Energy Conversion, IEEE Transaction on*, 3(3):465–472, Sep 1988.

[7] M.M. Saied. A study on the matching of dc motors to photovoltaic solar arrays. *Electrical Machines and Systems, 2001. ICEMS 2001. Proceedings of the Fifth International Conference on*, 1:652–655 vol.1, 2001.

[8] J. Appelbaum and S. Singer. Magnification of starting torques of dc motors by maximum power point trackers in photovoltaic systems. *Energy Convers. Eng.*

Conf., IECEC-89., Proc. of 24th Intersociety, pages 749–754 vol.2, Aug 1989.

[9] S. Singer and J. Appelbaum. Starting characteristics of direct current motors powered by solar cells. *Energy Conversion, IEEE Transaction on*, 8(1):47–53, Mar 1993.

[10] T. Esram and P.L. Chapman. Comparison of photovoltaic array maximum power point tracking techniques. *Energy Conversion, IEEE Transaction on*, 22(2):439–449, June 2007.

[11] Weidong Xiao, William G. Dunford, Patrick R. Palmer, and Antoine Capel. Regulation of photovoltaic voltage. *Industrial Electronics, IEEE Transactions on*, 54(3):1365–1374, June 2007.

[12] Johan H. R. Enslin, Mario S. Wolf, Daniel B. Snyman, and Wernher Swiegers. Integrated photovoltaic maximum power point tracking converter. *Industrial Electronics, IEEE Transactions on*, 44, 1997.

[13] H. Patel and V. Agarwal. Maximum power point tracking scheme for pv systems operating under partially shaded conditions. *Industrial Electronics, IEEE Transactions on*, 55(4):1689–1698, April 2008.

[14] Omar Gil-Arias and Eduardo I. Ortiz-Rivera. A general purpose tool for simulating the behavior of pv solar cells, modules and arrays. *Control and Modeling for Power Electronics, 2008. COMPEL 2008. 11th Workshop on*, pages 1–5, Aug. 2008.

[15] M.G. Villalva, J.R. Gazoli, and E.R. Filho. Comprehensive approach to modeling and simulation of photovoltaic arrays. *Power Electronics, IEEE Transactions on*, 24(5):1198–1208, May 2009.

[16] E.I. Ortiz-Rivera and F.Z. Peng. Analytical model for a photovoltaic module using the electrical characteristics provided by the manufacturer data sheet. *Power Electronics Specialists Conf., 2005. PESC '05. IEEE 36th*, pages 2087–2091, Sept. 2005.

[17] E.I. Ortiz-Rivera. *Modeling and Analysis of solar Distributed Generation.* PhD thesis, Michigan State University, 2006.

[18] V. Scarpa, S. Buso, and G. Spiazzi. Low-complexity mppt technique exploiting the pv module mpp locus characterization. *Industrial Electronics, IEEE Transactions on*, 56(5):1531–1538, May 2009.

[19] Weidong Xiao, M.G.J. Lind, W.G. Dunford, and A. Capel. Real-time identification of optimal operating points in photovoltaic power systems. *Industrial Electronics, IEEE Transactions on*, 53(4):1017–1026, June 2006.

[20] Weidong Xiao, N. Ozog, and W.G. Dunford. Topology study of photovoltaic interface for maximum power point tracking. *Industrial Electronics, IEEE Transactions on*, 54(3):1696–1704, June 2007.

[21] M.A. Elgendy, B. Zahawi, and D.J. Atkinson. Analysis of the performance of dc photovoltaic pumping systems with maximum power point tracking. *Power Electronics, Machines and Drives, 2008. PEMD 2008. 4th IET Conference on*, pages 426–430, April 2008.

[22] E.I. rtiz Rivera and Fang Peng. A novel method to estimate the maximum power for a photovoltaic inverter system. *Power Electronics Specialists Conf., 2004. PESC 04. IEEE 35th Annual*, 3:2065–2069 Vol.3, 20-25 June 2004.

[23] E.I. Ortiz Rivera and F.Z. Peng. Linear reoriented coordinates method. In *Electro/information Technology, 2006 IEEE International Conference on*, pages 459–464, May 2006.

[24] M.A.S. Masoum, H. Dehbonei, and E.F. Fuchs. Theoretical and experimental analyses of photovoltaic systems with voltageand current-based maximum power-point tracking. *Energy Conversion, IEEE Transactions on*, 17(4):514–522, Dec 2002.

[25] T. Noguchi, S. Togashi, and R. Nakamoto. Short-current pulse-based maximum-power-point tracking method for multiple photovoltaic-and-converter module

system. *Industrial Electronics, IEEE Transactions on*, 49:217 – 223, 2002.

[26] A. Hussein, K. Hirasawa, Jinglu Hu, and J. Murata. The dynamic performance of photovoltaic supplied dc motor fed from dc-dc converter and controlled by neural networks. *Neural Networks, 2002. IJCNN '02. Proceedings of the 2002 International Joint Conference on*, 1:607–612, 2002.

[27] Chee Wei Tan, T.C. Green, and C.A. Hernandez-Aramburo. Analysis of perturb and observe maximum power point tracking algorithm for photovoltaic applications. *Power and Energy Conference, 2008. PECon 2008. IEEE 2nd International*, pages 237–242, Dec. 2008.

[28] Tae-Yeop Kim, Ho-Gyun Ahn, Seung Kyu Park, and Youn-Kyun Lee. A novel maximum power point tracking control for photovoltaic power system under rapidly changing solar radiation. In *Industrial Electronics, 2001. Proceedings. ISIE 2001. IEEE Inter. Symp. on*, volume 2, pages 1011–1014 vol.2, 2001.

[29] N. Femia, G. Petrone, G. Spagnuolo, and M. Vitelli. Optimization of perturb and observe maximum power point tracking method. *Power Electronics, IEEE Transactions on*, 20(4):963–973, July 2005.

[30] K.H. Hussein, I. Muta, T. Hoshino, and M. Osakada. Maximum photovoltaic power tracking: an algorithm for rapidly changing atmospheric conditions. *Generation, Transmission and Distribution, IEE Proceedings-*, 142(1):59–64, Jan 1995.

[31] Richard Wies, Bipin Satavalekar, Ashish Agrawal, Javad Mahdavi, Ali Agah, and Ali Emadi. *Power Electronics Handbook*, chapter DC-DC Converters. CRC Press, 2002.

[32] N. Mohan, T. Undeland, and W. Robbins. *Power Electronics: Converters, applications and design*. John Wiley & Sons, inc., 2nd edition, 2003.

[33] Hebertt Sira-Ramírez and Ramón Silva-Ortigoza. *Control Design Techniques in Power Electronics Devices*. Springer, 2006.

[34] R. Erickson and D. Maksimovic. *Fundamentals of Power Electronics.* Springer, 2nd edition, 2000.

[35] William Shepherd and Li Zhang. *Power converter circuits.* Marcel Dekker, Inc., 2004.

[36] A.M. Sharaf, E. Elbakush, and I.H. Altas. Novel control strategies for photovoltaic powered pmdc motor drives. *Electrical Power Conference, 2007. EPC 2007. IEEE Canada*, pages 461–466, Oct. 2007.

[37] R. Krishnan. *Electric Motor Drives, Modeling, analysis and control.* Prentice Hall, 2001.

[38] K.H. Hussein, I. Muta, T. Hoshino, and M. Osakada. Field and armature control for separately excited dc motors powered by photovoltaic cells. *Photovoltaic Energy Conversion, 1994., Conference Record of the Twenty Fourth. IEEE Photovoltaic Specialists Conference - 1994, 1994 IEEE First World Conference on*, 1:1169–1172 vol.1, Dec 1994.

[39] M. Akbaba. Optimization of the performance of solar powered permanent magnet dc motor drives. *Electrical Machines and Power Electronics, 2007. ACEMP '07. International Aegean Conference on*, pages 725–729, Sept. 2007.

[40] S.S. Shokrolla, N.T. Twieg, and A.M. Sharaf. A photovoltaic powered separately excited dc motor drive for rural/desert pump irrigation. *Electrical Machines and Drives, 1993. 6th International Conf. on*, pages 406–411, Sep 1993.

[41] K. Venkatesan and D. Cheverez-Gonzalez. Matching dc motors to photovoltaic generators for maximum power tracking. *Applied Power Electronics Conf. and Exp. APEC '97 Conf. Proc. 1997., 12th Annual*, 1:514–519 vol.1, Feb 1997.

[42] A. Tariq and M.S.J. Asghar. Matching of a separately excited dc motor to a photovoltaic panel using an analog maximum power point tracker. *Industrial Technology, 2006. ICIT 2006. IEEE International Conf. on*, pages 1020–1025, Dec. 2006.

[43] A.M. Sharaf and Liang Yang. A novel maximum power trecking controller for a stand-alone photovoltaic dc motor drive. *Electrical and Computer Engineering, 2006. CCECE '06. Canadian Conference on*, pages 450–453, May 2006.

[44] A.M. Sharaf, E. Elbakush, and I.H. Altas. An error driven pid controller for maximum utilization of photovoltaic powered pmdc motor drives. *Electrical and Computer Eng., 2007. CCECE 2007. Canadian Conf. on*, pages 129–132, April 2007.

[45] H.S.-H. Chung, K.K. Tse, S.Y.R. Hui, C.M. Mok, and M.T. Ho. A novel maximum power point tracking technique for solar panels using a sepic or cuk converter. *Power Electronics, IEEE Transactions on*, 18(3):717–724, May 2003.

[46] The Mathworks, MATLAB - the language of technical computing. http://www.mathworks.com/products/matlab/, Dec. 2009. [Online].

[47] The Mathworks, MATLAB - Simulink simulation and model-based design. http://www.mathworks.com/products/simulink/, Dec. 2009. [Online].

[48] E.I. Ortiz-Rivera. Maximum power point tracking using the optimal duty ratio for dc-dc converters and load matching in photovoltaic applications. In *Applied Power Electronics Conference and Exposition, 2008. APEC 2008. Twenty-Third Annual IEEE*, pages 987–991, Feb. 2008.

[49] Dogan Ibrahim. *Miconcontroller based applied digital control.* John Wiley & Sons, 2006.

[50] Antonio Visioli. *Practical PID control.* Advances in Industrial Control. Springer, October 2006.

[51] Simone Buso and Paolo Mattavelli. *Digital control in power electronics.* Lectures on Power Electronics. Morgan & Claypool Publishers, 2007.

[52] Datasheet: 8-bit avr microcontroller atmega48v/88v/168v.

[53] Steven F. Barrett and Daniel Pack. *Atmel AVR Microcontroller Primer: Programming and Interfacing.* Morgan & Claypool Publishers, 2008.

[54] Saber: Industry standard for multi-domain and mixed-signal simulation. http://www.synopsys.com/Tools/SLD/Mechatronics/Saber/Pages/default.aspx, Dec. 2009. [Online].

[55] M.E. Ropp and S. Gonzalez. Development of a matlab/simulink model of a single-phase grid-connected photovoltaic system. *Energy Conversion, IEEE Transactions on*, 24(1):195–202, March 2009.

APPENDICES

Appendix A

PV Module Characteristics

The current-voltage characteristics of two PV modules (PVMs) that are connected in series are shown in figure A–1. The power-voltage characteristics are shown in figure A–2.

These curves represent the behavior of the PV array consisted of two PVMs connected in series. The temperature is constant for all the curves, their value is $59°C$. The irradiance increases from $450W/m^2$ to $1200W/m^2$ with an increment of $150W/m^2$.

For an irradiance value, these characteristics can be obtained evaluating the open-circuit voltage and the short circuit current with equations (A.1) and (A.2), respectively[1] . After, the PV voltage is varied from zero to open-circuit voltage in order to calculate the PV current with equation (A.3)[2] .

$$V_x = s \cdot (T - T_N) \cdot TC_v + s \cdot A \left(\exp \left(B \cdot \frac{E_i}{E_{iN}} \right) - \exp \left(C \cdot \frac{E_i}{E_{iN}} \right) \right) \qquad \text{(A.1)}$$

$$I_x = \frac{Ei}{E_{in}} \cdot [I_{sc} + TC_i \cdot (T - T_N)] \qquad \text{(A.2)}$$

$$I(V) = \frac{p \cdot I_x}{1 - exp\left(\frac{-1}{b}\right)} \cdot \left[1 - \exp \left(\frac{V}{b \cdot s \cdot V_x} - \frac{1}{b} \right) \right] \qquad \text{(A.3)}$$

---

[1] For details see: O. Gil-Arias. Modelado y Simulación de Dispositivos Fotovoltaicos. MS thesis, University of Puerto Rico at Mayagüez, 2008

[2] For details of PV model see: E.I. Ortiz-Rivera. Modeling and Analysis of solar Distributed Generation. PhD thesis, Michigan State University, 2006.
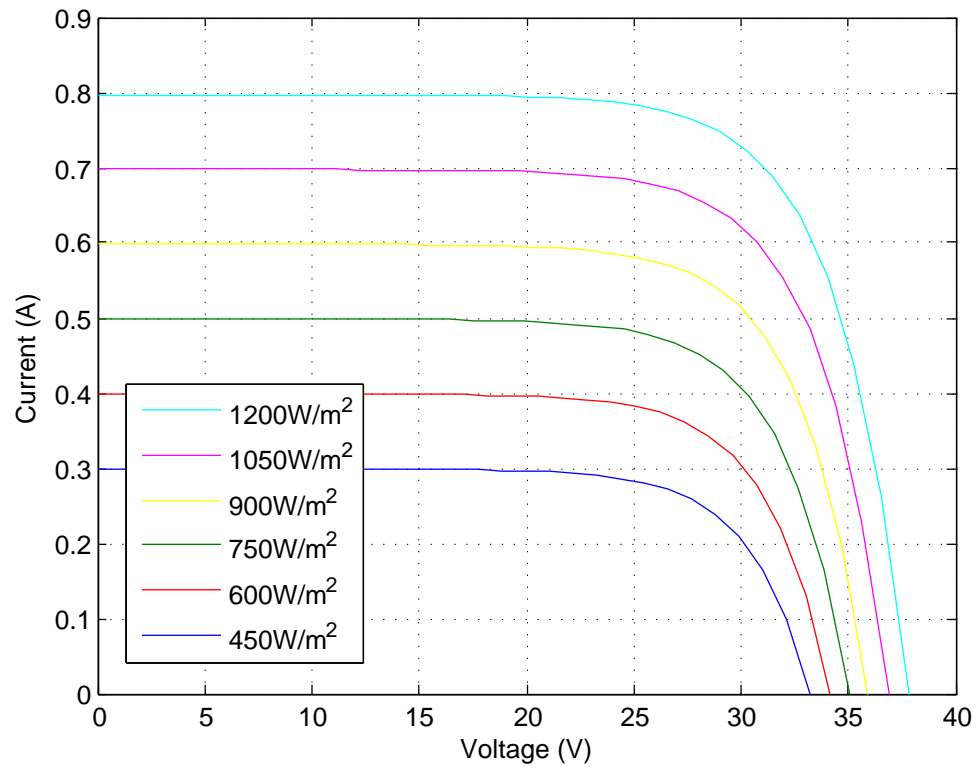
Figure A–1: I - V characteristics of two SX-10M connected in series
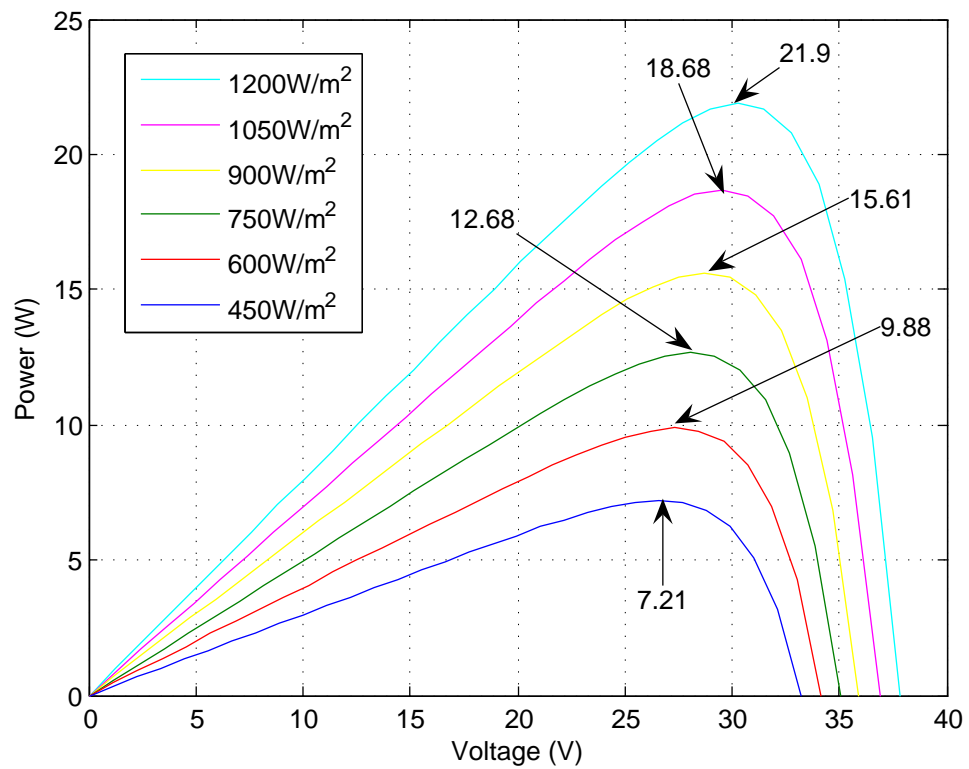
Figure A–2: P - V characteristics of two SX-10M connected in series

Appendix B

DC motor Characteristics

The parameters of DC motor are presented in [41] and these parameters are shown in table B–1.

Table B–1: Parameters for Permanent Magnet DC Motor

Symbol	Parameter	Value	Units
R_a	Armature resistance	8.57	Ω
L_a	Armature inductance	58.7	mH
K_e	Back emf constant	0.1485	$\frac{V}{rad/sec}$
J	Moment of inertia	45.5×10^{-6}	$Kg \cdot m^2$
B_m	Viscous friction coefficient	94.8×10^{-6}	$\frac{N \cdot m}{rad/seg}$

In order to validate the parameters, real data were registered and compared with the simulation results. Below, current vs. voltage and power vs. voltage are presented for each position in figure B–1 and B–2 respectively. In each figure discontinue blue lines show the real data for different positions as is shown in the label, while colored continuous lines show the simulation data. As can be seen from the graph, the characteristic curves of the DC motor are approximates using the parameters listed above.

The motor is loaded with an eddy current brake; then, in order to obtain the load torque characteristics, the armature voltage and current and the motor speed are registered for different positions. Since, the load torque is given by $T_L = K_e \cdot I_a - B_m \cdot \omega_m$, this torque is calculated and plotted versus the motor speed for each position, as is shown in figure B–3
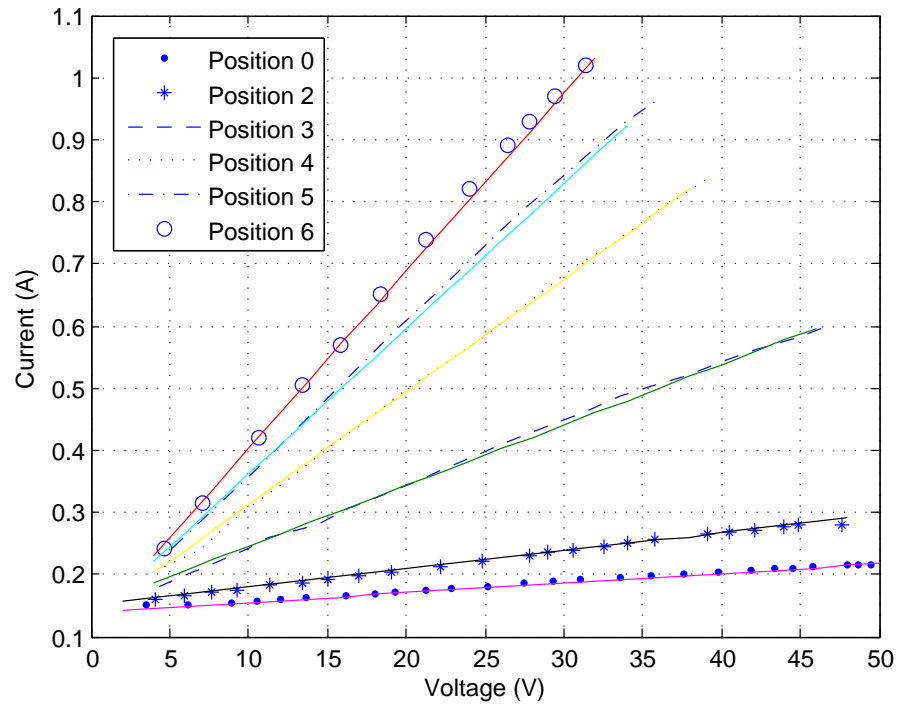
Figure B–1: Current vs Voltage for different positions
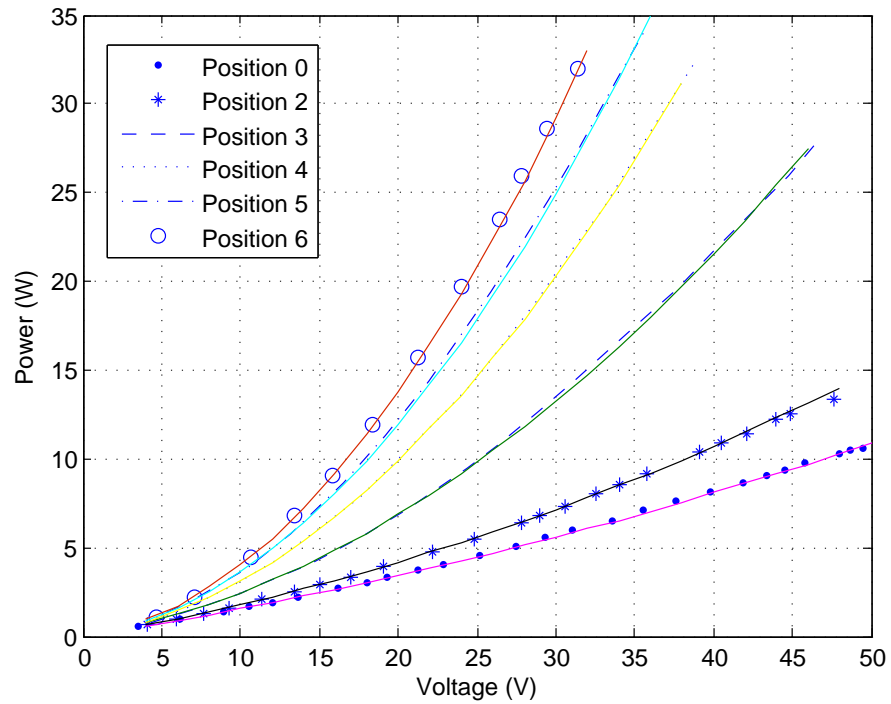
Figure B–2: Power vs voltage for different positions

The torque-speed characteristic has a linear relationship, this characteristic has the form $T_L = c_1 \cdot \omega_m + c_2$. Using fitting curve the constant c_1 and c_2 were derived for different position of the magnet. Theses values are shown in table B–2.
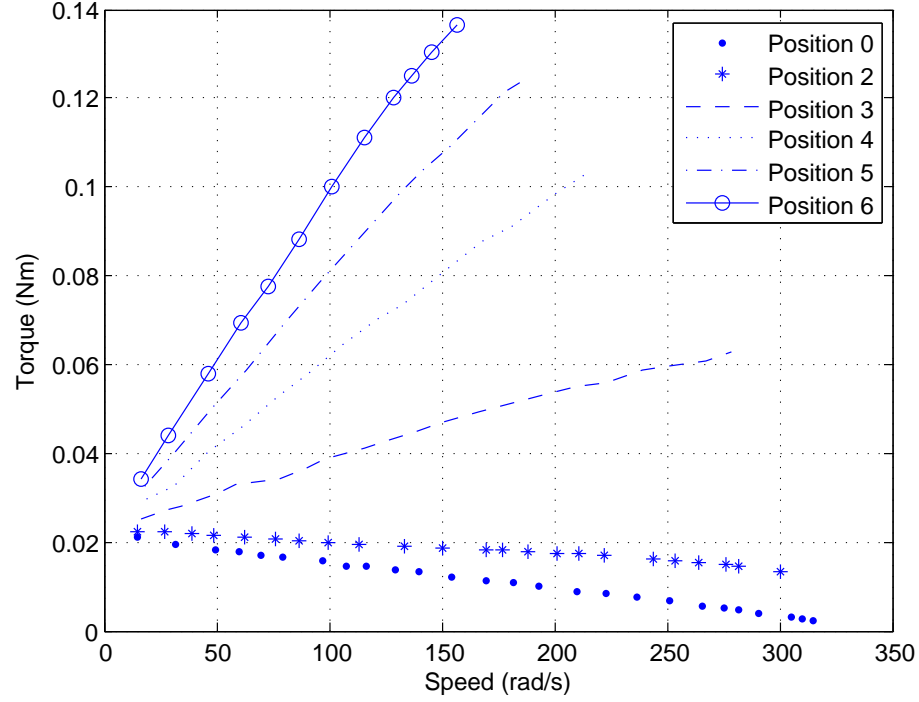
Figure B–3: Load Torque Characteristics

Position	Constant c_1	Constant c_2
0	-0.00006	0.021
2	-0.000029	0.023
3	0.00014	0.024
4	0.00038	0.023
5	0.00055	0.024
6	0.00074	0.023

Table B–2: Load torque characteristic for different positions, $T_L = c_1 \cdot \omega_m + c_2$

Appendix C

Simulink Models

PVM Model Volt
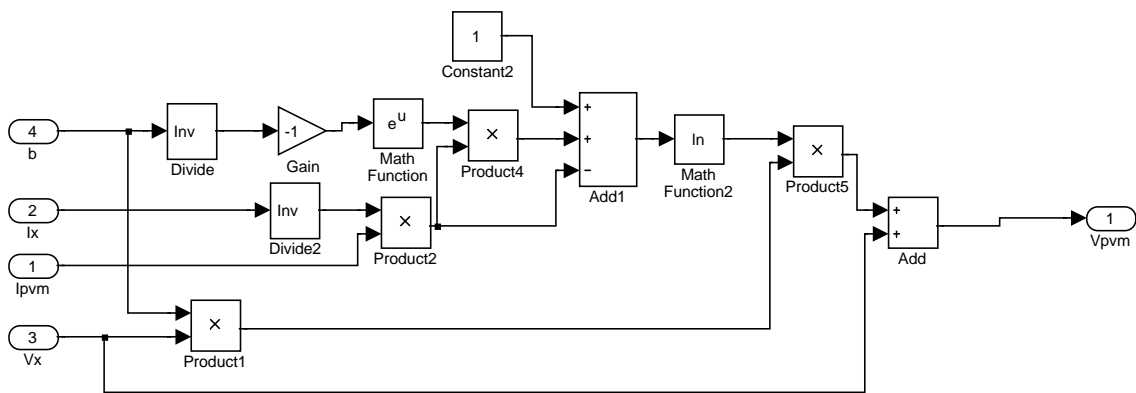
Figure C–1: Simulink Model of a PVM in voltage mode

DC Motor Model
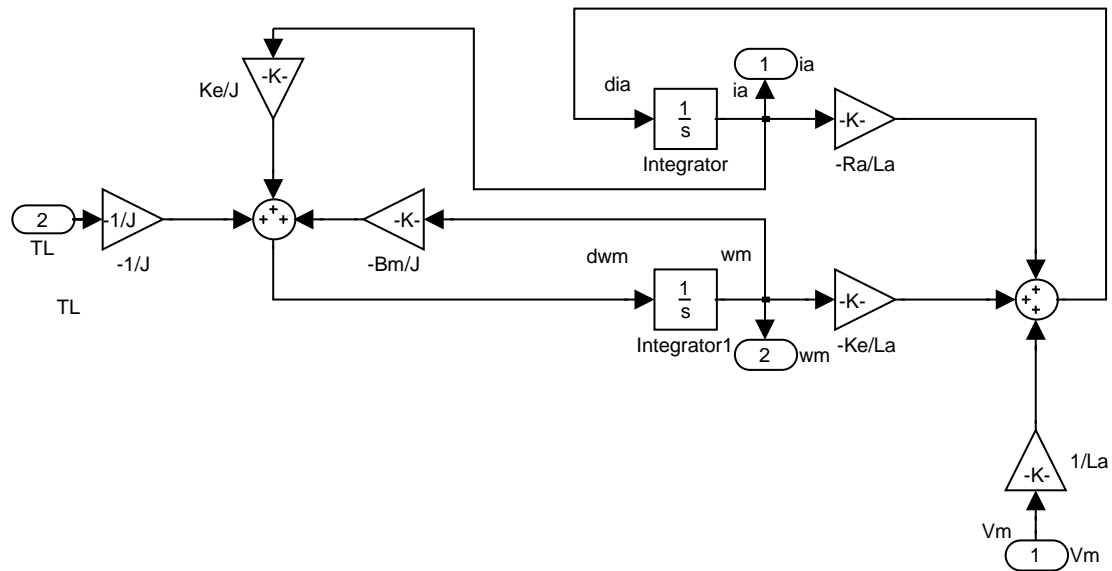
Figure C–2: Simulink Model of a DC motor

Load torque
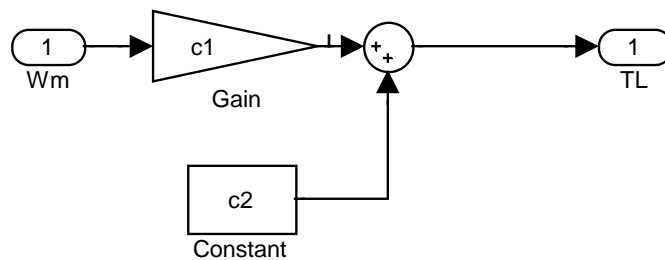
Figure C–3: Simulink Model of a load torque

Appendix D

Source Code for ATmega88

Initialization functions

```c
void TIMER0_init(void)
{
//Set Bit0-->  Enable Interrupt OV
TIMSK0=0x01;
//Operation Mode Normal WGM0=0
TCCR0A=0x00;
//Clock Select
TCCR0B=(1<<CS00);
}

void PWM1_init(void){
//-----------Timer 1--------------------
// Set non-inverting pwm mode::
  // Set Fast PWM 10-bit:: (3<<WGM10)
// Set Fast PWM 9-bit:: (2<<WGM10)
// No prescaling on clock::
TCCR1A=(2<<COM1A0)|(2<<COM1B0)|(2<<WGM10);
TCCR1B=(1<<CS10)|(1<<WGM12);
}

void ADC_init(void)
{//External AREF and select channel
ADMUX=0;
 //set ADC prescaler to 1MHz / 8 = 125kHz
ADCSRA=(1<<ADEN)|(1<<ADPS1)|(1<<ADPS0);
 //dummy conversion
ADCSRA|=1<<ADSC;
while(!(ADCSRA & 0x10))
;
ADCSRA|=0x10;  //clear conv rdy flag set the bit
}
```

Interrupt Service Routine for LRCM

```
ISR(TIMER0_OVF_vect)
{ char mystr[16];
unsigned int VxD;
counter++;
if((counter)==TIMEOK){
VoltPVM=(float) (ADC_Read(ADCvolt)*CTEVOLT);
error=VoltOpt-VoltPVM;
VxD = ADC_ReadAVG(ADCcurr);     //Read Ipvm
if (VxD <409) //For Volt < 2
CurrPVM= (float) (VxD*0.002246-0.59);
else
CurrPVM= (float) (VxD*0.005859-2.08);
u=control(error);
DUTY=pwmGen(u);
    counter=0;
    //Read Speed
    VxD = ADC_Read(1);
    sprintf(mystr,"%.2f\t%.2f\t%.2f\t%d\r",
            (double)VoltPVM,(double)CurrPVM,(double)u,(int)VxD);
    sendString(mystr);
     }
counterLRCM++;
if((counterLRCM)==TIME_LRCMOK){
VoltOpt=getLRCM();
counterLRCM=0;
sprintf(mystr,"Vap=%.2f\r",(double)VoltOpt); sendString(mystr);
}
}
```

Interrupt Service Routine for P&O

```
ISR(TIMER0_OVF_vect)
{  char mystr[25];
unsigned int VxD;
float dutyC; // Declaration for P&O method
counter++;
if((counter)==TIMEOK){
VoltPVM=(float) (ADC_Read(2)*CTEVOLT); //Read Vpvm
VxD = ADC_ReadAVG(3);       //Read Ipvm
if (VxD <409) //For Volt < 2
CurrPVM= (float) (VxD*0.002246-0.59);
else
CurrPVM= (float) (VxD*0.005859-2.08);

PowPVM= VoltPVM*CurrPVM; //P&O method
if (PowPVM < PowPVM_ant)
dDuty=-dDuty;
dutyC=dutyC_ant + dDuty;

DUTY=dutyC; //Update the duty cycle
dutyC_ant=dutyC;
PowPVM_ant=PowPVM;

   counter=0;
   //Read Tachometer Voltage
    VxD = ADC_ReadAVG(1);
    sprintf(mystr,"%.2f\t%.2f\t%.2f\t%d\r",
     (double)VoltPVM,(double)CurrPVM,(double)dutyC),VxD;
    sendString(mystr);
    }
}
```

Serial Communications functions

```
/*
 * serial.c
 *
 *  Routine for serial communications
 *
 */
#include "serial.h"
#include <avr/io.h>

char isCharAvailable()
{
// Does the RX0 bit of the USART Status and Control Register
// indicate a char has been received?
```

```
if ( (UCSR0A & (0x80)) ) return 1;
else return 0;
}


char receiveChar()
{
// Return the char in the UDR0 register
return UDR0;
}


void sendChar(char data)
{
    int i = 0;

    // To send data with the USART put the data in the USART data register
    UDR0 = data;

    // Check to see if the global interrupts are enabled
    if(SREG & 0x80)
    {
// Wait until the byte is sent or we count out
while ( !(UCSR0A&0x40) && (i<10000) )
{
i++;
}
    }
    else  // Wait until the byte is sent
        while( !(UCSR0A&0x40) );

      // Clear the TXCflag
UCSR0A=UCSR0A|0x40;
}


void sendString(char s[])
{
int i = 0;

while(i < 64) // don't get stuck if it is a bad string
{
if( s[i] == '\0' ) break; // quit on string terminator
sendChar(s[i++]);
}
}


void USART_init()
{
```

```
    // Set the USART baudrate registers for xxxxx bps with xxMHz
    UBRR0H = 0;//(unsigned char)(baudrate>>8);
    UBRR0L = BAUDRATEREG;//(unsigned char)baudrate;

    /*-------No se usa--------JDGL 2009-03-28
// Enable 2x speed change
    UCSR0A = (1<<U2X0);*/

    // Enable receiver and transmitter
    UCSR0B = (1<<RXEN0)|(1<<TXEN0)|(0<<RXCIE0)|(0<<UDRIE0);

    // Set the USART to asynchronous at 8 bits no parity and 1 stop bit
    UCSR0C = (0<<UMSEL00)|(0<<UPM00)|(0<<USBS0)|(3<<UCSZ00)|(0<<UCPOL0);
}
```

Appendix E

Matlab Files

Parameters of simulation of MPPT using Simulink for LRCM

mfile: PVBuckBoostMotorSim.m

```
%PVBUCKBOOSTMOTOR Load components and simulation parametes
%   Use the file BPSX10M from MyPVMlib folder and the PE482bParam
%   Input: file BPSX10M.m, PE482bParam.m
%   Output: Ipvm, Vpvm, Ix_sc, Vx_sc, Vap, Wm
%% PVM parameteres
BPSX10M
s=2; p=1;
Ci=470e-6;
%% DC/DC parameteres
L=1000e-6;
C=56e-6;
%% DC Motor parameters
PE482bParam
c1=0.00014;
c2=0.024;
%% Controller Parameters
Kp=0.0;
Ki=5;
Vamp=5;
%% Simulation parameters
%Ei=600; % The model is using a repeating stair sequence
T=59;
clear Ipvm Vpvm  Ix_sc Vx_sc  Vap Wm
 sim('PVBuckBoostMotorLRCM',2)
%% Graph
figure
subplot(2,1,2), plot(Vpvm(:,1),Vpvm(:,2)), ylabel('PV array Voltage (V)')
hold on, plot(Vap(:,1),Vap(:,2),'r'), xlabel('Time'), grid on
subplot(2,1,1), plot(Ipvm(:,1),Ipvm(:,2)), ylabel('PV array Current (A)')
grid on
figure
subplot(2,1,1), plot(Vpvm(:,1),Ipvm(:,2).*Vpvm(:,2))
ylabel('PV array Power'), grid on
subplot(2,1,2), plot(Wm(:,1),Wm(:,2)), ylabel('Motor Speed (rad/s)')
xlabel('Time'), grid on
figure
plot(Duty(:,1),Duty(:,2)), ylabel('Duty Ratio'), xlabel('Time'), grid on
```

Parameters of Photovoltaic Modules

<p align="center"><i>mfile</i>: BPSX10M.m</p>

```
%BPSX10M Load and calculate the PV Module parameters
%    Input: none
%    Output: Vop, Voc, Iop, Isc, TCv, TCi, b, Vmax, Vmin, Ap, Bp, Cp
disp('Module BPSX10M')
%%  PVM Datasheet Parameters
Vop = 16.8;
Voc = 21;
Iop = 0.59;
Isc = 0.65;
TCv = -80e-3;
TCi = 0.4225e-3;
% Constantes para el panel
b=bPanel( Vop, Voc, Iop, Isc, 1, 1e-2);
Vmax = Voc*1.03;
Vmin = Voc*0.85;
% Standard Test Condition
Tn = 25;
Ein = 1000;
%constant OmarGil, se pueden calcular con ABCPanel(), pero se debe escoger de
%entre los múltiples valores que arroja
Ap=18.1148; Bp=0.1478; Cp=-15.5481;
```

Parameters of DC motors

<p align="center"><i>mfile</i>: PE482bParam.m</p>

```
%PE482bPARAM Load the DC motor parameters
%    Input: none
%    Ouput: Variables La, Ra, J, Bm, Ke
%---------------DC Motor----------------------
La=0.0587; %Motor inductance [H]
Ra=8.57;     %Armature resitance [Ohm]
J=0.0455e-3; %[Kg-m^2]
Bm=0.0948e-3; %[Nm/(rad/s)]
Ke=0.1485;   %V/(rad/sec)
```

Parameters of simulation of MPPT using Simulink for P&O

mfile: `PVBuckBoostMotorPandOSim.m`

```
    %PVBUCKBOOSTMOTORPANDO Load components and simulation parametes
%    Use the file BPSX10M from MyPVMlib folder
%    Input: file BPSX10M.m
%    Output: Ipvm, Vpvm, Ix_sc, Vx_sc, Vap, Wm
%% PVM parameteres
BPSX10M
s=2;
p=1;
Ci=470e-6;
%% DC/DC parameteres
L=1000e-6;
C=56e-6;
%% DC Motor parameters
PE482bParam
c1=0.00055;
c2=0.024;
%% Controller Parameters
DUTYINI=0.5;
STEPSIZE=0.02;
TS=0.1;
%% Simulation parameters
%Ei=600; % The model is using a repeating stair sequence
T=59;
clear Ipvm Vpvm  Ix_sc Vx_sc  Vap Wm
 sim('PVBuckBoostMotorPandO',30)
%% Graph
figure %Position 482,670
subplot(5,1,1), plot(Vpvm(:,1),Vpvm(:,2)), ylabel('PV voltage (V)')
title('Simulation of P & 0'), grid on
% hold on, plot(Vap(:,1),Vap(:,2),'r'),
subplot(5,1,2), plot(Ipvm(:,1),Ipvm(:,2)), ylabel('PV current (A)')
grid on
subplot(5,1,3), plot(Vpvm(:,1),Ipvm(:,2).*Vpvm(:,2))
ylabel('PV array Power'), grid on
subplot(5,1,4), plot(Wm(:,1),Wm(:,2)), ylabel('Motor Speed (rad/s)')
grid on
subplot(5,1,5), plot(Duty(:,1),Duty(:,2)*100), ylabel('Duty Ratio (%)')
xlabel('Time (s)'), grid on
```

Appendix F

Schematic and PCB Layout
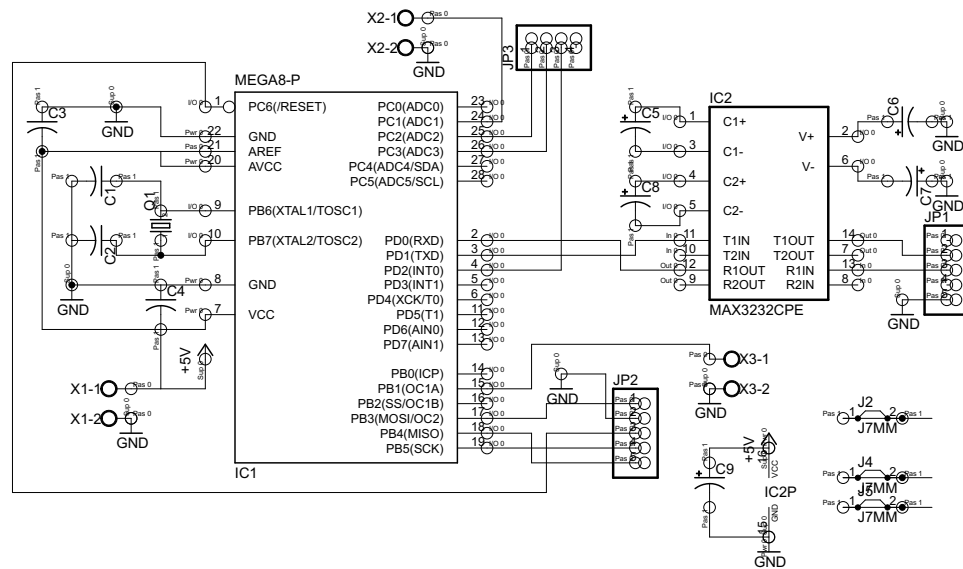
Figure F–1: Schematic of ATmega88 board
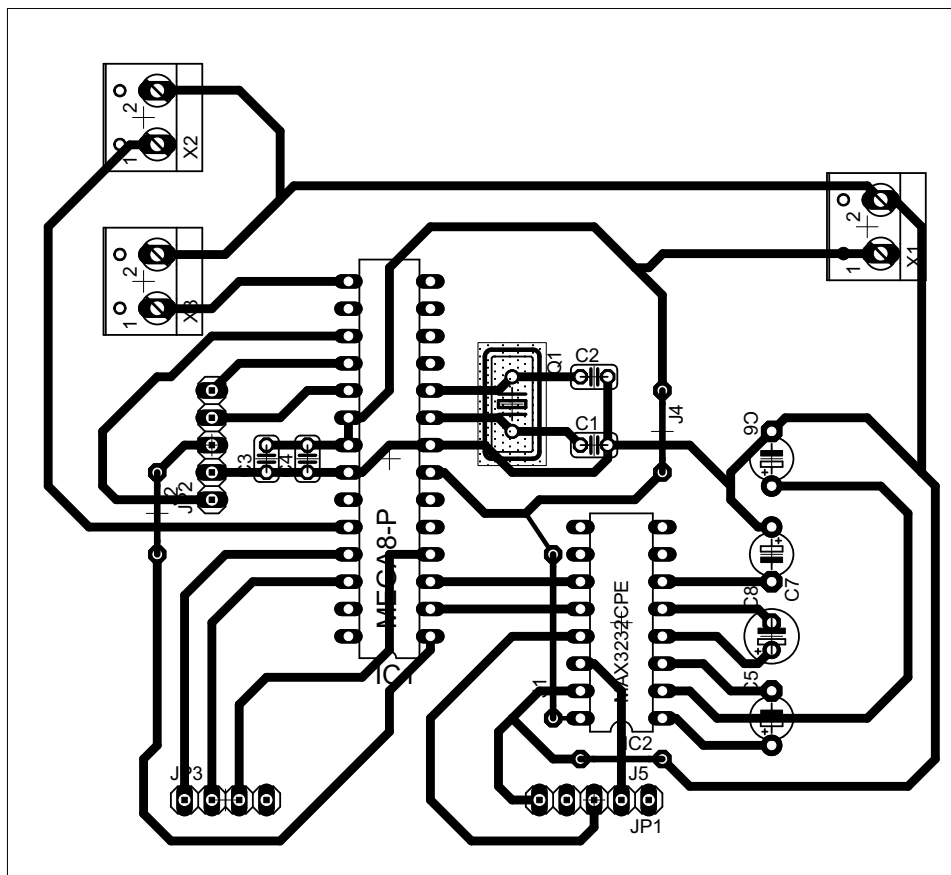
Figure F–2: PCB of ATmega88 board
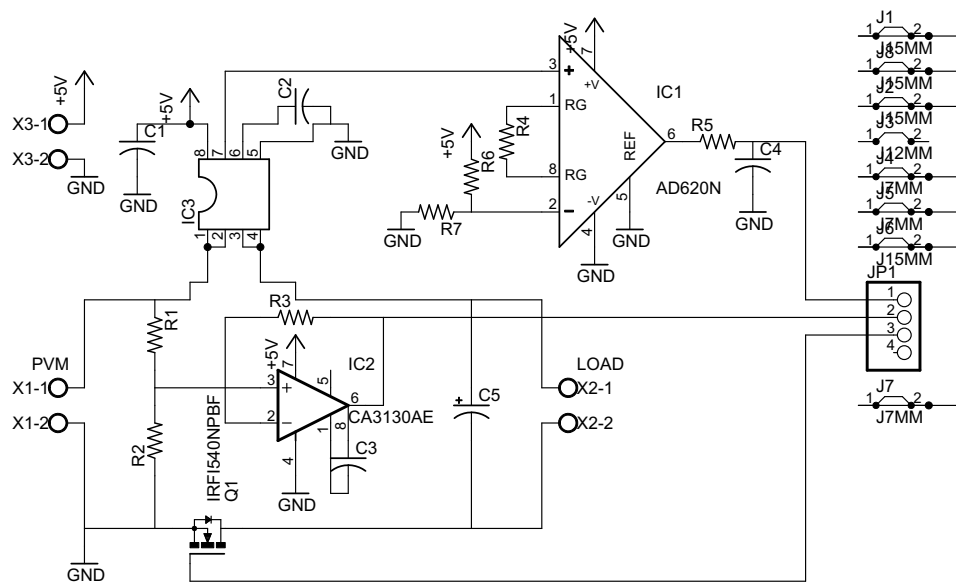
Figure F–3: Schematic of Sensing Board
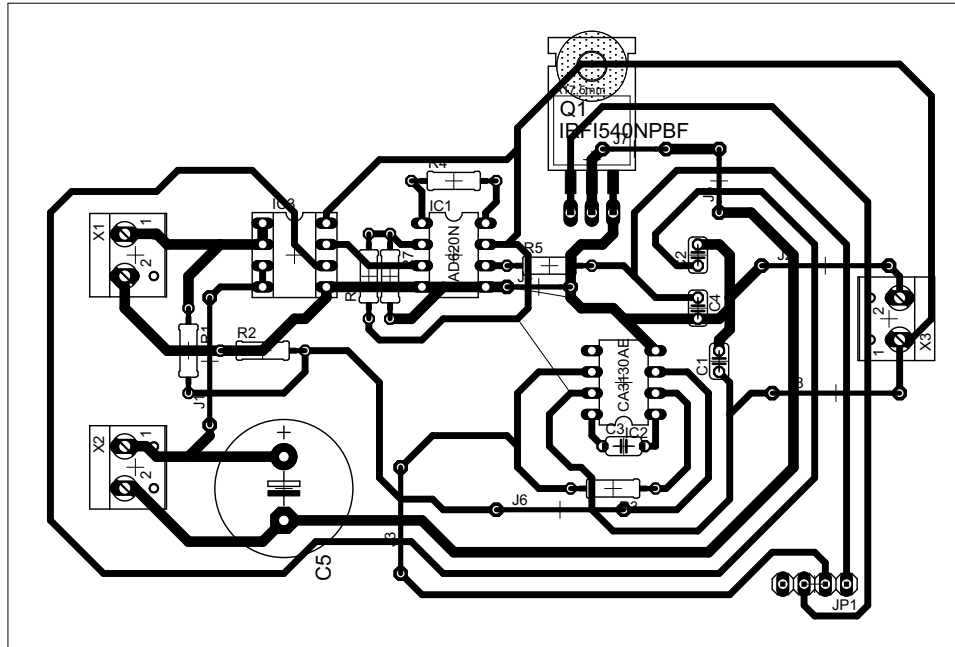
Figure F–4: PCB Sensing Board
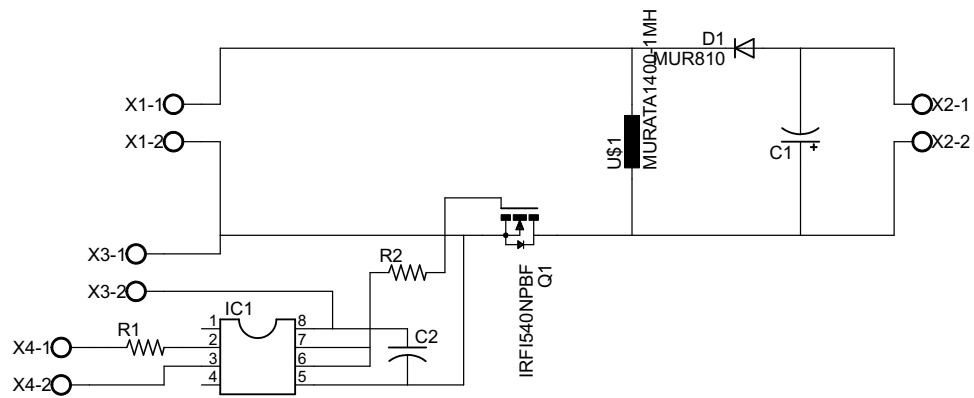
Figure F–5: Schematic of Power converter board
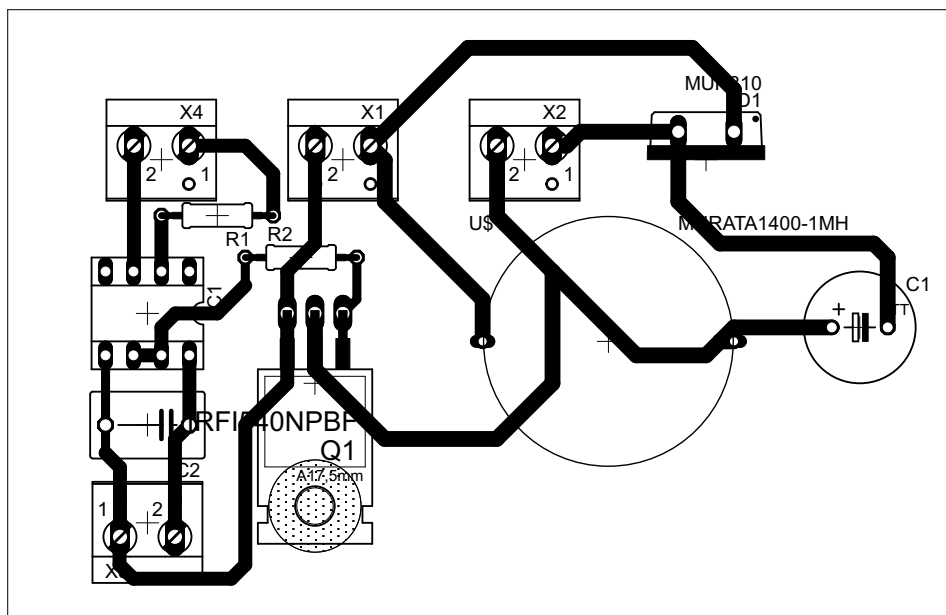
Figure F–6: PCB of Power converter board

Appendix G

Publications

The paper in this list have been accepted for presentation and publication at international conferences, during the development of this research, being part of the Minds^{2}CREATE group.

- Gonzalez-Llorente, J.; Ortiz-Rivera, E. I. and Salazar-Llinas, A. "Analyzing the Optimal Matching of DC Motors to Photovoltaic Modules via DC-DC converters" in *Applied Power Electronics Conference and Exposition, 2010. APEC 2010. Twenty-Fifth Annual IEEE*, Feb. 2010

  Abstract: *Because to the nonlinear behavior of the photovoltaic (PV) cells, dc/dc power converters are added for matching the load to the photovoltaic generators. In this paper, we use mathematical models in order to examine the behavior of the off-grid photovoltaic system composed by: PV generator, dc/dc converter and dc motor. We compare different converter topologies (step-up, step-down and step-down/step-up) and evaluate the feasibility of being used as interface to attain operation around of the maximum power point (MPP). Our analysis found the relationships between the optimal duty ratio and the maximum power, and between the optimal duty ratio and the motor speed; using these relationships, the simplest topology to meet the requirement can be selected as interface. Moreover, a simple but reliable maximum power point tracking (MPPT) method and a controller are implemented on a microcontroller and tested in real weather conditions. The MPPT provides an approximation to the optimal voltage or to the optimal current in a straightforward way, and the controller adjusts the duty ratio of the power converter, improving the matching of the PVM supplying a dc motor, when operation around MPP is obtained.*

- Gonzalez-Llorente, J.; Ortiz-Rivera, E. I. and Diaz, A. "A maximum power point tracker using positive feedforward control based on the DC motor dynamics and PVM mathematical model" in *Electric Machines and Drives Conf. IEMDC '09. IEEE International*, 2009, 259-264

  Abstract: *This paper presents a maximum power tracking method for DC motor fed from photovoltaic modules (PVM) through step-down power converter. This method employs positive feedback of motor speed; therefore, only DC motor speed measurements are required. The designed control law is based on mathematical model of DC motor and power converter, and also, variations of optimal maximum power point (MPP) are considered at different values of irradiance. Optimal MPP is approximated by method known as linear reoriented coordinates method (LRCM). Finally, a simple analog circuit is designed and implemented, which calculates optimal duty ratio for power converter according to DC motor speed.*

- Ortiz-Rivera, E. I.; Gonzalez-Llorente, J. and Salazar-Llinas, A. "Bringing Renewable Energy to the Electrical Engineering Undergraduate Education and Research At UPRM" *Frontiers in Education Conference, 2009. FIE 2009. 39th Annual*, 2009

  Abstract: *The development of systems implementing renewable energy sources is essential to society's evolution and survival. Currently the major source for electric energy is the burning of fossil fuels; thus, it is a problem because of two reasons: it increases the emission of harmful gases to our atmosphere and it is an energy source that will not last forever. In our present time the amount of energy produced by a single renewable source is considerably smaller that the amount produced by the burning of fossil fuels. Therefore, it is necessary to develop energy systems that will use various type of renewable energy in parallel, all contributing to a large complex system. It is the purpose of this paper to attract undergraduate students to the area of renewable energy by bringing them with a research experience. The student had the experience to study three alternative sources: photovoltaic systems, fuel cells, and thermoelectric generators. The student had the opportunity to use electrical models describing the performance of each renewable source. The mathematical models were developed by the mentor in different software like Matlab, Saber, P-Spice, and Simulink. Circuit analysis, simulations and experiments are presented in the paper.*

Appendix H

Manufacturer datasheets

- Multicrystalline Photovoltaic Modules BP SX 5M and SX 10M.

- ATmega 88, 8-bit Microcontroller with 8K Bytes Flash

- AD620, Low Cost Low Power Instrumentation Amplifier.

- CA3130, 15MHz, BiMOS OpAmp with MOSFET Input/CMOS Output.

- ACS712, Fully Integrated, Hall Effect-Based Linear Current Sensor.

- MAX232, Dual EIA-232 Drivers/Receivers.

- LM324, Low power quad operational amplifiers.

- UC3526, Regulating pulse width modulator.

- 1410516C, Bobbin type inductors 1400 series.

bp solar

The smallest of BP Solar's SX™ module series, BP SX 5 and BP SX 10 photovoltaic modules operate DC loads with small to moderate energy requirements. With 36 multicrystalline cells in series, they charge 12V batteries efficiently in virtually any climate. Typical commercial applications of these modules, which generate nominal maximum power of 4.5 watts and 10 watts respectively, include remote telemetry, instrumentation systems, security sensors, and signals.

SX 5M and SX 10M

The versatile Multimount™ frame of the SX 5M and SX 10M provides great flexibility in mounting approach. Oriented parallel to the edge and back of the module, its dual channels accept the heads of 8mm or 5/16" hex bolts, allowing the module to be mounted from the side or back. Bolts may be located anywhere along the channels, a configuration which prevents them from turning during tightening and allows installation with just one wrench.

Multimount™ Frame
(shown with end caps removed)

Output of the SX 5M and SX 10M is via a 4.6m (15 foot) PVC-jacketed 1mm^2 (AWG 18-2) cable which terminates in a low-profile junction box on the module back. Epoxy-potted in the box, module electrical connections are sealed against corrosion and effectively strain-relieved. The modules are intended for single-module applications with DC system voltage not exceeding 30 volts, and may be ordered in either 6V or 12V nominal voltage.

Universal Frame

SX 10U

The SX 10U includes a heavy-duty Universal frame and a high-capacity junction box which accepts cable or conduit and provides field-selectable dual voltage output. Optionally, this junction box can be fitted with:
- blocking and bypass diodes;
- an oversize terminal block which accepts conductors up to 25mm^2 (AWG #4); standard terminals accept up to 6mm^2 (AWG #10);
- a Solarstate™ charge regulator.

The SX 10U junction box may be field-wired to provide 12V or 6V nominal output. Six-volt modules are intended to support 6V loads, and are not recommended as series elements in higher voltage arrays. The SX 10U meets NEC requirements for use in systems up to 600 VDC, and is approved by Factory Mutual Research for application in NEC Class 1, Division 2, Groups C & D hazardous locations.

Limited Warranties
- Power output for 12 years;
- Freedom from defects in materials and workmanship for 2 years.

See our website or your local representative for full terms of these warranties.
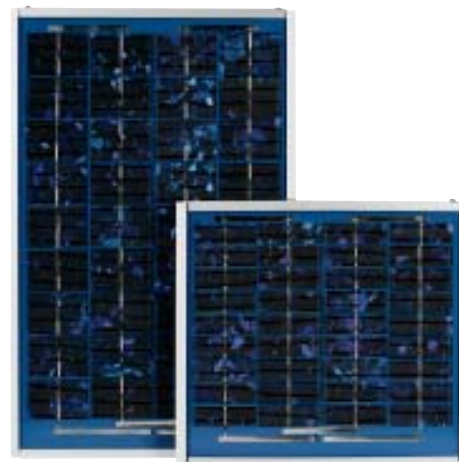
SX 10M and 5M

Quality and Safety

All SX 5 and 10 modules are manufactured in ISO 9001-certified factories and are:
- listed by Underwriter's Laboratories for electrical and fire safety (Class C fire rating);
- certified by TÜV Rheinland as Class II equipment.
- compliant with the requirements of IEC 61215 and including:
  ◦ repetitive cycling between -40°C and 85°C at 85% relative humidity;
  ◦ simulated impact of 25mm (one-inch) hail at terminal velocity;
  ◦ a "damp heat" test, consisting of 1000 hours of exposure to 85°C and 85% relative humidity;
  ◦ a "hot-spot" test, which determines a module's ability to tolerate localized shadowing (which can cause reverse-biased operation and localized heating); static loading, front and back, of 2400 pascals (50 psf); front loading (e.g. snow, U only) of 5400 pascals (113 psf).

Electrical Characteristics[1]

	SX 10	SX 5
Maximum Power (P_{max})[2]	10W	4.5W
Voltage at P_{max} (V_{mp})	16.8V	16.5V
Current at P_{max} (I_{mp})	0.59A	0.27A
Warranted minimum P_{max}	9W	4W
Short-circuit current (I_{SC})	0.65A	0.3A
Open-circuit voltage (V_{OC})	21.0V	20.5V
Temperature coefficient of I_{SC}	(0.065±0.015)%/°C	
Temperature coefficient of V_{OC}	-(80±10)mV/°C	
Temperature coefficient of power	-(0.5±0.05)%/°C	
NOCT[3]	47±2°C	

Notes

1. These data represent the performance of typical modules in 12V configuration as measured at their output, and do not include the effect of such additional equipment as diodes. The data are based on measurements made in accordance with ASTM E1036 corrected to SRC (Standard Reporting Conditions, also known as STC or Standard Test Conditions), which are:
   • illumination of 1 kW/m²(1 sun) at spectral distribution of AM 1.5 (ASTM E892 global spectral irradiance);
   • cell temperature of 25°C.

2. During the stabilization process which occurs during the first few months of deployment, module power may decrease approximately 3% from typical P_{max}.

3. The cells in an illuminated module operate hotter than the ambient temperature. NOCT (Nominal Operating Cell Temperature) is an indicator of this temperature differential, and is the cell temperature under Standard Operating Conditions: ambient temperature of 20°C, solar irradiation of 0.8 kW/m², and wind speed of 1m/s.

SX 5 and 10 I-V Curves

SX-10
T=0°C
T=25°C
T=50°C
T=75°C

SX-5
T=0°C
T=25°C
T=50°C
T=75°C
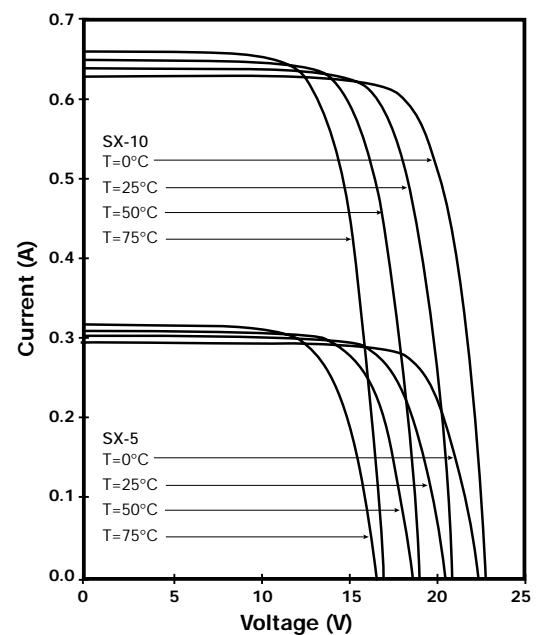
Features

- **High Performance, Low Power AVR® 8-Bit Microcontroller**
- **Advanced RISC Architecture**
  - **131 Powerful Instructions – Most Single Clock Cycle Execution**
  - **32 x 8 General Purpose Working Registers**
  - **Fully Static Operation**
  - **Up to 20 MIPS Throughput at 20 MHz**
  - **On-chip 2-cycle Multiplier**
- **High Endurance Non-volatile Memory segments**
  - **4/8/16K Bytes of In-System Self-programmable Flash program memory**
  - **256/512/512 Bytes EEPROM**
  - **512/1K/1K Bytes Internal SRAM**
  - **Write/Erase cyles: 10,000 Flash/100,000 EEPROM** [1][3]
  - **Data retention: 20 years at 85°C/100 years at 25°C** [2][3]
  - **Optional Boot Code Section with Independent Lock Bits**
    In-System Programming by On-chip Boot Program
    True Read-While-Write Operation
  - **Programming Lock for Software Security**
- **Peripheral Features**
  - **Two 8-bit Timer/Counters with Separate Prescaler and Compare Mode**
  - **One 16-bit Timer/Counter with Separate Prescaler, Compare Mode, and Capture Mode**
  - **Real Time Counter with Separate Oscillator**
  - **Six PWM Channels**
  - **8-channel 10-bit ADC in TQFP and QFN/MLF package**
  - **6-channel 10-bit ADC in PDIP Package**
  - **Programmable Serial USART**
  - **Master/Slave SPI Serial Interface**
  - **Byte-oriented 2-wire Serial Interface (Philips I²C compatible)**
  - **Programmable Watchdog Timer with Separate On-chip Oscillator**
  - **On-chip Analog Comparator**
  - **Interrupt and Wake-up on Pin Change**
- **Special Microcontroller Features**
  - **Power-on Reset and Programmable Brown-out Detection**
  - **Internal Calibrated Oscillator**
  - **External and Internal Interrupt Sources**
  - **Five Sleep Modes: Idle, ADC Noise Reduction, Power-save, Power-down, and Standby**
- **I/O and Packages**
  - **23 Programmable I/O Lines**
  - **28-pin PDIP, 32-lead TQFP, 28-pad QFN/MLF and 32-pad QFN/MLF**
- **Operating Voltage:**
  - **1.8 - 5.5V for ATmega48V/88V/168V**
  - **2.7 - 5.5V for ATmega48/88/168**
- **Temperature Range:**
  - **-40°C to 85°C**
- **Speed Grade:**
  - **ATmega48V/88V/168V: 0 - 4 MHz @ 1.8 - 5.5V, 0 - 10 MHz @ 2.7 - 5.5V**
  - **ATmega48/88/168: 0 - 10 MHz @ 2.7 - 5.5V, 0 - 20 MHz @ 4.5 - 5.5V**
- **Low Power Consumption**
  - **Active Mode:**
    250 µA at 1 MHz, 1.8V
    15 µA at 32 kHz, 1.8V (including Oscillator)
  - **Power-down Mode:**
    0.1µA at 1.8V

Notes: 1. Worst case temperature. Guaranteed after last write cycle.
2. Failure rate less than 1 ppm.
3. Characterized through accelerated tests.

**8-bit AVR®
Microcontroller
with 8K Bytes
In-System
Programmable
Flash**

**ATmega48/V
ATmega88/V
ATmega168/V**

Summary

1. Pin Configurations

Figure 1-1. Pinout ATmega48/88/1682545LS

TQFP Top View

PDIP

28 MLF Top View

NOTE: Bottom pad should be soldered to ground.

32 MLF Top View

NOTE: Bottom pad should be soldered to ground.
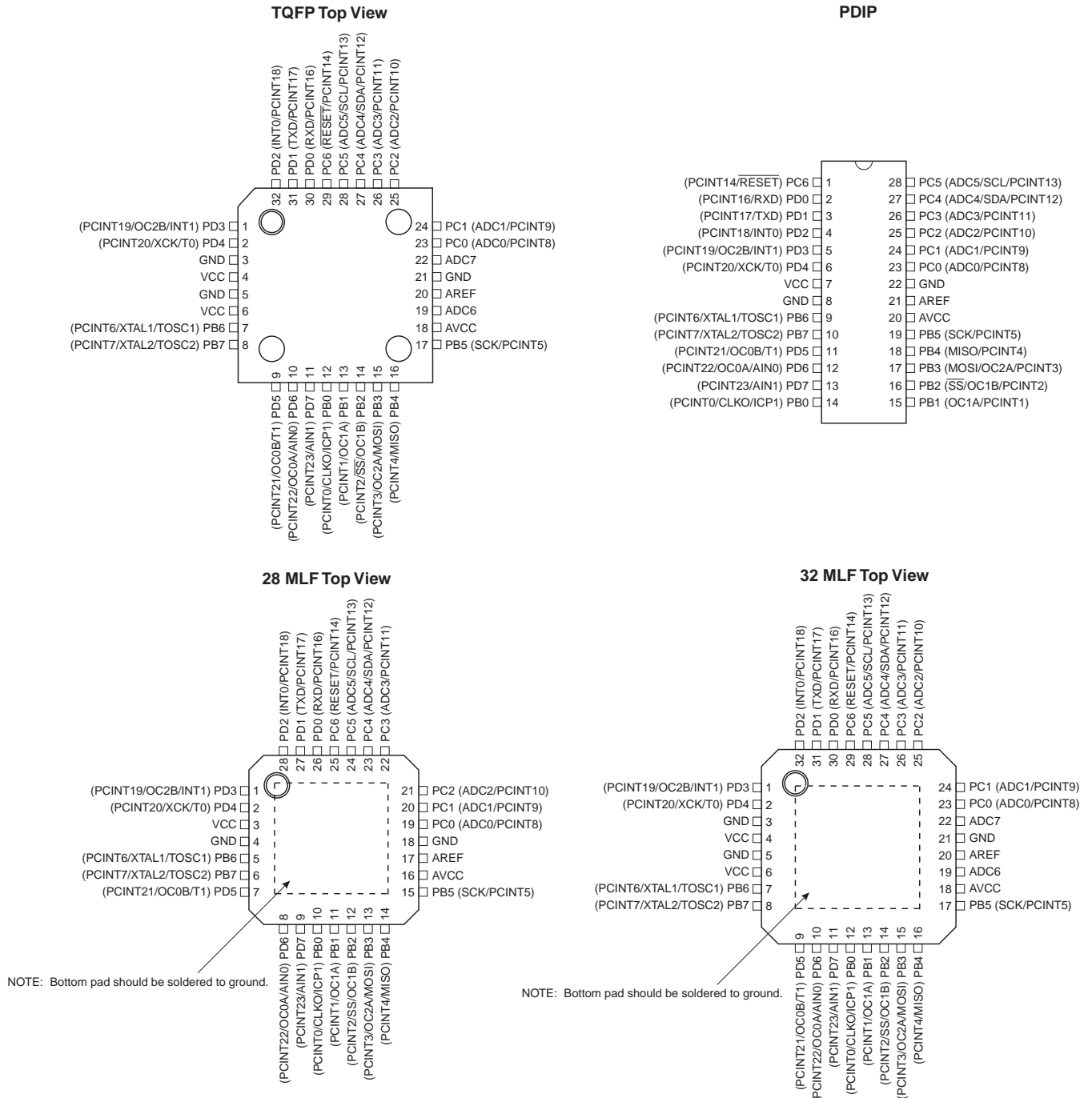
1.1 Pin Descriptions

1.1.1 VCC

Digital supply voltage.

1.1.2 GND

Ground.

1.1.3 Port B (PB7:0) XTAL1/XTAL2/TOSC1/TOSC2

Port B is an 8-bit bi-directional I/O port with internal pull-up resistors (selected for each bit). The Port B output buffers have symmetrical drive characteristics with both high sink and source capability. As inputs, Port B pins that are externally pulled low will source current if the pull-up resistors are activated. The Port B pins are tri-stated when a reset condition becomes active, even if the clock is not running.

Depending on the clock selection fuse settings, PB6 can be used as input to the inverting Oscillator amplifier and input to the internal clock operating circuit.

Depending on the clock selection fuse settings, PB7 can be used as output from the inverting Oscillator amplifier.

If the Internal Calibrated RC Oscillator is used as chip clock source, PB7..6 is used as TOSC2..1 input for the Asynchronous Timer/Counter2 if the AS2 bit in ASSR is set.

The various special features of Port B are elaborated in "Alternate Functions of Port B" on page 78 and "System Clock and Clock Options" on page 27.

1.1.4 Port C (PC5:0)

Port C is a 7-bit bi-directional I/O port with internal pull-up resistors (selected for each bit). The PC5..0 output buffers have symmetrical drive characteristics with both high sink and source capability. As inputs, Port C pins that are externally pulled low will source current if the pull-up resistors are activated. The Port C pins are tri-stated when a reset condition becomes active, even if the clock is not running.

1.1.5 PC6/$\overline{\text{RESET}}$

If the RSTDISBL Fuse is programmed, PC6 is used as an I/O pin. Note that the electrical characteristics of PC6 differ from those of the other pins of Port C.

If the RSTDISBL Fuse is unprogrammed, PC6 is used as a Reset input. A low level on this pin for longer than the minimum pulse length will generate a Reset, even if the clock is not running. The minimum pulse length is given in Table 27-3 on page 307. Shorter pulses are not guaranteed to generate a Reset.

The various special features of Port C are elaborated in "Alternate Functions of Port C" on page 81.

1.1.6 Port D (PD7:0)

Port D is an 8-bit bi-directional I/O port with internal pull-up resistors (selected for each bit). The Port D output buffers have symmetrical drive characteristics with both high sink and source capability. As inputs, Port D pins that are externally pulled low will source current if the pull-up

Low Cost Low Power Instrumentation Amplifier
AD620

FEATURES
Easy to use
    Gain set with one external resistor
      (Gain range 1 to 10,000)
    Wide power supply range (±2.3 V to ±18 V)
    Higher performance than 3 op amp IA designs
    Available in 8-lead DIP and SOIC packaging
    Low power, 1.3 mA max supply current
Excellent dc performance (B grade)
    50 μV max, input offset voltage
    0.6 μV/°C max, input offset drift
    1.0 nA max, input bias current
    100 dB min common-mode rejection ratio (G = 10)
Low noise
    9 nV/√Hz @ 1 kHz, input voltage noise
    0.28 μV p-p noise (0.1 Hz to 10 Hz)
Excellent ac specifications
    120 kHz bandwidth (G = 100)
    15 μs settling time to 0.01%

APPLICATIONS
Weigh scales
ECG and medical instrumentation
Transducer interface
Data acquisition systems
Industrial process controls
Battery-powered and portable equipment

CONNECTION DIAGRAM
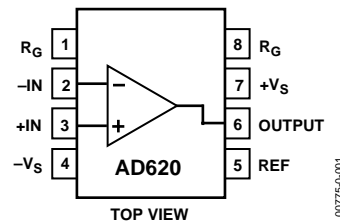
Figure 1. 8-Lead PDIP (N), CERDIP (Q), and SOIC (R) Packages

PRODUCT DESCRIPTION
The AD620 is a low cost, high accuracy instrumentation amplifier that requires only one external resistor to set gains of 1 to 10,000. Furthermore, the AD620 features 8-lead SOIC and DIP packaging that is smaller than discrete designs and offers lower power (only 1.3 mA max supply current), making it a good fit for battery-powered, portable (or remote) applications.

The AD620, with its high accuracy of 40 ppm maximum nonlinearity, low offset voltage of 50 μV max, and offset drift of 0.6 μV/°C max, is ideal for use in precision data acquisition systems, such as weigh scales and transducer interfaces. Furthermore, the low noise, low input bias current, and low power of the AD620 make it well suited for medical applications, such as ECG and noninvasive blood pressure monitors.

The low input bias current of 1.0 nA max is made possible with the use of Superβeta processing in the input stage. The AD620 works well as a preamplifier due to its low input voltage noise of 9 nV/√Hz at 1 kHz, 0.28 μV p-p in the 0.1 Hz to 10 Hz band, and 0.1 pA/√Hz input current noise. Also, the AD620 is well suited for multiplexed applications with its settling time of 15 μs to 0.01%, and its cost is low enough to enable designs with one in-amp per channel.
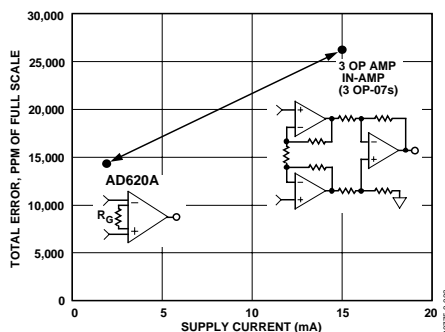
Figure 2. Three Op Amp IA Designs vs. AD620

Figure 3. Total Voltage Noise vs. Source Resistance

Rev. G

15MHz, BiMOS Operational Amplifier with MOSFET Input/CMOS Output

CA3130A and CA3130 are op amps that combine the advantage of both CMOS and bipolar transistors.

Gate-protected P-Channel MOSFET (PMOS) transistors are used in the input circuit to provide very-high-input impedance, very-low-input current, and exceptional speed performance. The use of PMOS transistors in the input stage results in common-mode input-voltage capability down to 0.5V below the negative-supply terminal, an important attribute in single-supply applications.

A CMOS transistor-pair, capable of swinging the output voltage to within 10mV of either supply-voltage terminal (at very high values of load impedance), is employed as the output circuit.

The CA3130 Series circuits operate at supply voltages ranging from 5V to 16V, (±2.5V to ±8V). They can be phase compensated with a single external capacitor, and have terminals for adjustment of offset voltage for applications requiring offset-null capability. Terminal provisions are also made to permit strobing of the output stage.

- The CA3130A offers superior input characteristics over those of the CA3130.
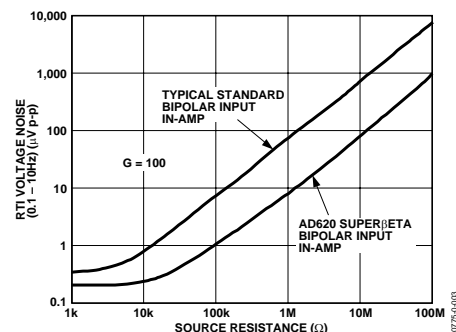
Ordering Information

PART NO. (BRAND)	TEMP. RANGE (^{O}C)	PACKAGE	PKG. DWG. #
CA3130AE	-55 to 125	8 Ld PDIP	E8.3
CA3130AM (3130A)	-55 to 125	8 Ld SOIC	M8.15
CA3130AM96 (3130A)	-55 to 125	8 Ld SOIC Tape and Reel	M8.15
CA3130AMZ (3130AZ) (Note)	-55 to 125	8 Ld SOIC (Pb-free)	M8.15
CA3130AMZ96 (3130AZ) (Note)	-55 to 125	8 Ld SOIC Tape and Reel (Pb-free)	M8.15
CA3130E	-55 to 125	8 Ld PDIP	E8.3
CA3130EZ (Note)	-55 to 125	8 Ld PDIP* (Pb-free)	E8.3
CA3130M (3130)	-55 to 125	8 Ld SOIC	M8.15
CA3130M96 (3130)	-55 to 125	8 Ld SOIC Tape and Reel	M8.15
CA3130MZ (3130MZ) (Note)	-55 to 125	8 Ld SOIC (Pb-free)	M8.15
CA3130MZ96 (3130MZ)	-55 to 125	8 Ld SOIC Tape and Reel (Pb-free)	M8.15

*Pb-free PDIPs can be used for through hole wave solder processing only. They are not intended for use in Reflow solder processing applications.

NOTE: Intersil Pb-free plus anneal products employ special Pb-free material sets; molding compounds/die attach materials and 100% matte tin plate termination finish, which are RoHS compliant and compatible with both SnPb and Pb-free soldering operations. Intersil Pb-free products are MSL classified at Pb-free peak reflow temperatures that meet or exceed the Pb-free requirements of IPC/JEDEC J STD-020.

Features

- MOSFET Input Stage Provides:
  - Very High Z_I = 1.5 TΩ (1.5 x $10^{12}\Omega$) (Typ)
  - Very Low I_I . . . . 5pA (Typ) at 15V Operation
    . . . .= 2pA (Typ) at 5V Operation
- Ideal for Single-Supply Applications
- Common-Mode Input-Voltage Range Includes Negative Supply Rail; Input Terminals can be Swung 0.5V Below Negative Supply Rail
- CMOS Output Stage Permits Signal Swing to Either (or both) Supply Rails
- Pb-Free Plus Anneal Available (RoHS Compliant)

Applications

- Ground-Referenced Single Supply Amplifiers
- Fast Sample-Hold Amplifiers
- Long-Duration Timers/Monostables
- High-Input-Impedance Comparators (Ideal Interface with Digital CMOS)
- High-Input-Impedance Wideband Amplifiers
- Voltage Followers (e.g. Follower for Single-Supply D/A Converter)
- Voltage Regulators (Permits Control of Output Voltage Down to 0V)
- Peak Detectors
- Single-Supply Full-Wave Precision Rectifiers
- Photo-Diode Sensor Amplifiers

Pinout

**CA3130, CA3130A
(PDIP, SOIC)**
TOP VIEW

OFFSET NULL	1	8 STROBE
INV. INPUT	2	7 V+
NON-INV. INPUT	3	6 OUTPUT
V-	4	5 OFFSET NULL
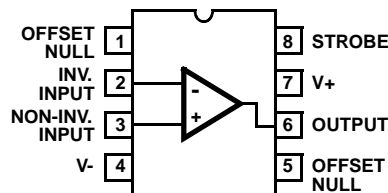
Fully Integrated, Hall Effect-Based Linear Current Sensor with 2.1 kVRMS Isolation and a Low-Resistance Current Conductor

Features and Benefits

- Low-noise analog signal path
- Device bandwidth is set via the new FILTER pin
- 5 µs output rise time in response to step input current
- 80 kHz bandwidth
- Total output error 1.5% at $T_A = 25°C$
- Small footprint, low-profile SOIC8 package
- 1.2 mΩ internal conductor resistance
- 2.1 kVRMS minimum isolation voltage from pins 1-4 to pins 5-8
- 5.0 V, single supply operation
- 66 to 185 mV/A output sensitivity
- Output voltage proportional to AC or DC currents
- Factory-trimmed for accuracy
- Extremely stable output offset voltage
- Nearly zero magnetic hysteresis
- Ratiometric output from supply voltage

TÜV America
Certificate Number:
U8V 06 05 54214 010

Package: 8 Lead SOIC (suffix LC)
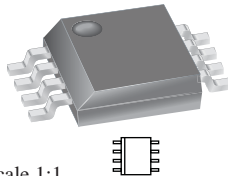
Approximate Scale 1:1

Description

The Allegro® ACS712 provides economical and precise solutions for AC or DC current sensing in industrial, commercial, and communications systems. The device package allows for easy implementation by the customer. Typical applications include motor control, load detection and management, switched-mode power supplies, and overcurrent fault protection.

The device consists of a precise, low-offset, linear Hall sensor circuit with a copper conduction path located near the surface of the die. Applied current flowing through this copper conduction path generates a magnetic field which is sensed by the integrated Hall IC and converted into a proportional voltage. Device accuracy is optimized through the close proximity of the magnetic signal to the Hall transducer. A precise, proportional voltage is provided by the low-offset, chopper-stabilized BiCMOS Hall IC, which is programmed for accuracy after packaging.

The output of the device has a positive slope ($>V_{IOUT(Q)}$) when an increasing current flows through the primary copper conduction path (from pins 1 and 2, to pins 3 and 4), which is the path used for current sensing. The internal resistance of this conductive path is 1.2 mΩ typical, providing low power

Continued on the next page…

Typical Application
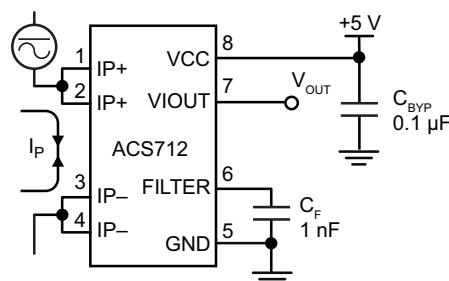
Application 1. The ACS712 outputs an analog signal, V_{OUT}. that varies linearly with the uni- or bi-directional AC or DC primary sensed current, I_P, within the range specified. C_F is recommended for noise management, with values that depend on the application.

- **Meets or Exceeds TIA/EIA-232-F and ITU Recommendation V.28**
- **Operates From a Single 5-V Power Supply With 1.0-μF Charge-Pump Capacitors**
- **Operates Up To 120 kbit/s**
- **Two Drivers and Two Receivers**
- **$\pm$30-V Input Levels**
- **Low Supply Current . . . 8 mA Typical**
- **ESD Protection Exceeds JESD 22**
  – 2000-V Human-Body Model (A114-A)
- **Upgrade With Improved ESD (15-kV HBM) and 0.1-μF Charge-Pump Capacitors is Available With the MAX202**
- **Applications**
  – TIA/EIA-232-F, Battery-Powered Systems, Terminals, Modems, and Computers

MAX232 . . . D, DW, N, OR NS PACKAGE
MAX232I . . . D, DW, OR N PACKAGE
(TOP VIEW)

C1+	1	16	V_{CC}
V_{S+}	2	15	GND
C1–	3	14	T1OUT
C2+	4	13	R1IN
C2–	5	12	R1OUT
V_{S-}	6	11	T1IN
T2OUT	7	10	T2IN
R2IN	8	9	R2OUT
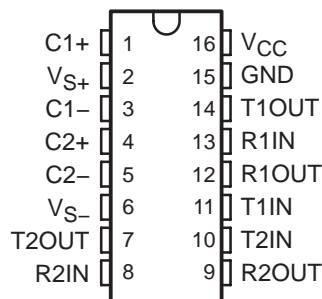
description/ordering information

The MAX232 is a dual driver/receiver that includes a capacitive voltage generator to supply TIA/EIA-232-F voltage levels from a single 5-V supply. Each receiver converts TIA/EIA-232-F inputs to 5-V TTL/CMOS levels. These receivers have a typical threshold of 1.3 V, a typical hysteresis of 0.5 V, and can accept $\pm$30-V inputs. Each driver converts TTL/CMOS input levels into TIA/EIA-232-F levels. The driver, receiver, and voltage-generator functions are available as cells in the Texas Instruments LinASIC™ library.

ORDERING INFORMATION

T_A	PACKAGE†		ORDERABLE PART NUMBER	TOP-SIDE MARKING
0°C to 70°C	PDIP (N)	Tube of 25	MAX232N	MAX232N
	SOIC (D)	Tube of 40	MAX232D	MAX232
		Reel of 2500	MAX232DR	
	SOIC (DW)	Tube of 40	MAX232DW	MAX232
		Reel of 2000	MAX232DWR	
	SOP (NS)	Reel of 2000	MAX232NSR	MAX232
−40°C to 85°C	PDIP (N)	Tube of 25	MAX232IN	MAX232IN
	SOIC (D)	Tube of 40	MAX232ID	MAX232I
		Reel of 2500	MAX232IDR	
	SOIC (DW)	Tube of 40	MAX232IDW	MAX232I
		Reel of 2000	MAX232IDWR	

† Package drawings, standard packing quantities, thermal data, symbolization, and PCB design guidelines are available at www.ti.com/sc/package.

Please be aware that an important notice concerning availability, standard warranty, and use in critical applications of Texas Instruments semiconductor products and disclaimers thereto appears at the end of this data sheet.

LinASIC is a trademark of Texas Instruments.

TEXAS
INSTRUMENTS

POST OFFICE BOX 655303 ● DALLAS, TEXAS 75265

Function Tables

EACH DRIVER

INPUT TIN	OUTPUT TOUT
L	H
H	L

H = high level, L = low level

EACH RECEIVER

INPUT RIN	OUTPUT ROUT
L	H
H	L

H = high level, L = low level

logic diagram (positive logic)
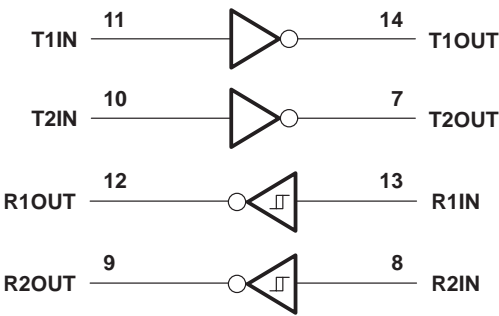
APPLICATION INFORMATION
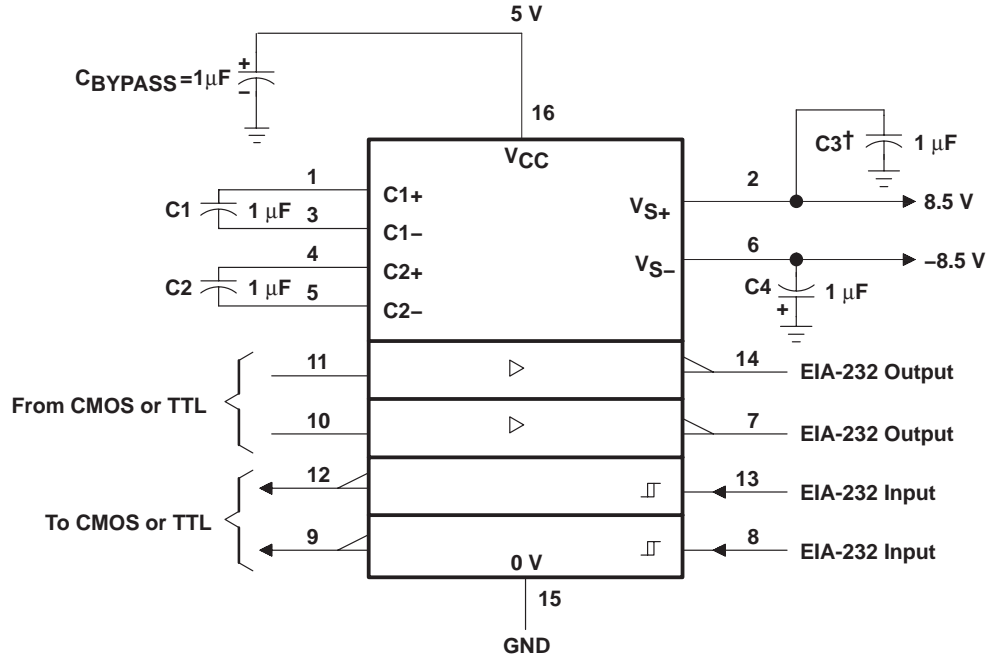
† C3 can be connected to V$_{CC}$ or GND.

NOTES: A. Resistor values shown are nominal.

B. Nonpolarized ceramic capacitors are acceptable. If polarized tantalum or electrolytic capacitors are used, they should be connected as shown. In addition to the 1-µF capacitors shown, the MAX202 can operate with 0.1-µF capacitors.

Figure 4. Typical Operating Circuit

National Semiconductor

August 2000

LM124/LM224/LM324/LM2902
Low Power Quad Operational Amplifiers

General Description

The LM124 series consists of four independent, high gain, internally frequency compensated operational amplifiers which were designed specifically to operate from a single power supply over a wide range of voltages. Operation from split power supplies is also possible and the low power supply current drain is independent of the magnitude of the power supply voltage.

Application areas include transducer amplifiers, DC gain blocks and all the conventional op amp circuits which now can be more easily implemented in single power supply systems. For example, the LM124 series can be directly operated off of the standard +5V power supply voltage which is used in digital systems and will easily provide the required interface electronics without requiring the additional ±15V power supplies.

Unique Characteristics

- In the linear mode the input common-mode voltage range includes ground and the output voltage can also swing to ground, even though operated from only a single power supply voltage
- The unity gain cross frequency is temperature compensated
- The input bias current is also temperature compensated

Advantages

- Eliminates need for dual supplies
- Four internally compensated op amps in a single package
- Allows directly sensing near GND and V_{OUT} also goes to GND
- Compatible with all forms of logic
- Power drain suitable for battery operation

Features

- Internally frequency compensated for unity gain
- Large DC voltage gain 100 dB
- Wide bandwidth (unity gain) 1 MHz (temperature compensated)
- Wide power supply range:
    Single supply 3V to 32V
    or dual supplies ±1.5V to ±16V
- Very low supply current drain (700 µA) — essentially independent of supply voltage
- Low input biasing current 45 nA (temperature compensated)
- Low input offset voltage 2 mV and offset current: 5 nA
- Input common-mode voltage range includes ground
- Differential input voltage range equal to the power supply voltage
- Large output voltage swing 0V to $V^+ - 1.5V$

Connection Diagrams

Dual-In-Line Package

00929901
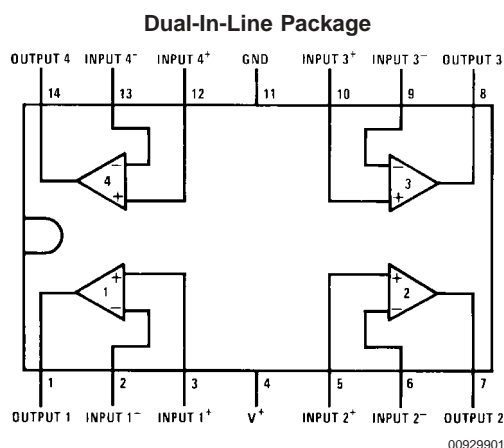
Top View
Order Number LM124J, LM124AJ, LM124J/883 (Note 2)**, LM124AJ/883** (Note 1)**, LM224J, LM224AJ, LM324J, LM324M, LM324MX, LM324AM, LM324AMX, LM2902M, LM2902MX, LM324N, LM324AN, LM324MT, LM324MTX or LM2902N LM124AJRQML and LM124AJRQMLV**(Note 3)
See NS Package Number J14A, M14A or N14A

Regulating Pulse Width Modulator

FEATURES

- 8 To 35V Operation

- 5V Reference Trimmed To ±1%

- 1Hz To 400kHz Oscillator Range

- Dual 100mA Source/Sink Outputs

- Digital Current Limiting

- Double Pulse Suppression

- Programmable Deadtime

- Under-Voltage Lockout

- Single Pulse Metering

- Programmable Soft-Start

- Wide Current Limit Common Mode Range

- TTL/CMOS Compatible Logic Ports

- Symmetry Correction Capability

- Guaranteed 6 Unit Synchronization

DESCRIPTION

The UC1526 is a high performance monolithic pulse width modulator circuit designed for fixed-frequency switching regulators and other power control applications. Included in an 18-pin dual-in-line package are a temperature compensated voltage reference, sawtooth oscillator, error amplifier, pulse width modulator, pulse metering and setting logic, and two low impedance power drivers. Also included are protective features such as soft-start and under-voltage lockout, digital current limiting, double pulse inhibit, a data latch for single pulse metering, adjustable deadtime, and provision for symmetry correction inputs. For ease of interface, all digital control ports are TTL and B-series CMOS compatible. Active LOW logic design allows wired-OR connections for maximum flexibility. This versatile device can be used to implement single-ended or push-pull switching regulators of either polarity, both transformerless and transformer coupled. The UC1526 is characterized for operation over the full military temperature range of -55°C to +125°C. The UC2526 is characterized for operation from -25°C to +85°C, and the UC3526 is characterized for operation from 0° to +70°C.

BLOCK DIAGRAM
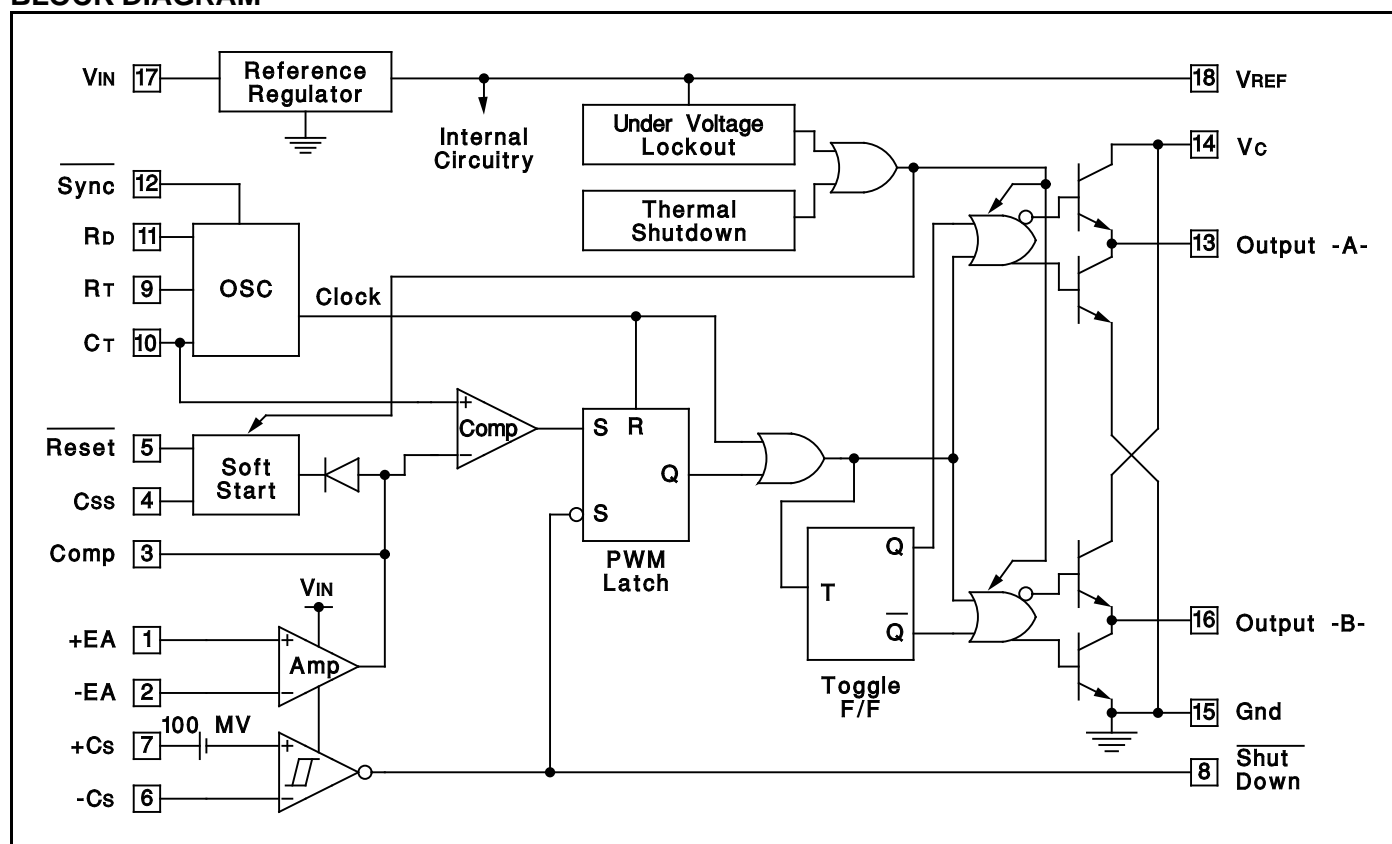
ABSOLUTE MAXIMUM RATINGS (Note 1, 2)

Input Voltage (+V$_{IN}$) . . . . +40V
Collector Supply Voltage (+V$_C$) . . . . +40V
Logic Inputs . . . . -0.3V to +5.5V
Analog Inputs . . . . -0.3V to +V$_{IN}$
Source/Sink Load Current (each output) 200mA
Reference Load Current. 50mA
Logic Sink Current 15mA
Power Dissipation at T$_A$ = +25°C (Note 2) 1000mW
Power Dissipation at T$_C$ = +25°C (Note 2) 3000mW
Operating Junction Temperature . . . . +150°C
Storage Temperature Range . . . . -65°C to +150°C
Lead Temperature (soldering, 10 seconds) . . . . +300°C
Note 1: Values beyond which damage may occur.
Note 2: Consult packaging section of databook for thermal
limitations and considerations of package.

RECOMMENDED OPERATING CONDITIONS (Note 3)

Input Voltage . . . . +8V to +35V
Collector Supply Voltage . . . . +4.5V to +35V
Sink/Source Load Current (each output) . . . . 0 to 100mA
Reference Load Current . . . . 0 to 20mA
Oscillator Frequency Range . . . . 1Hz to 400kHz
Oscillator Timing Resistor . . . . 2kΩ to 150kΩ
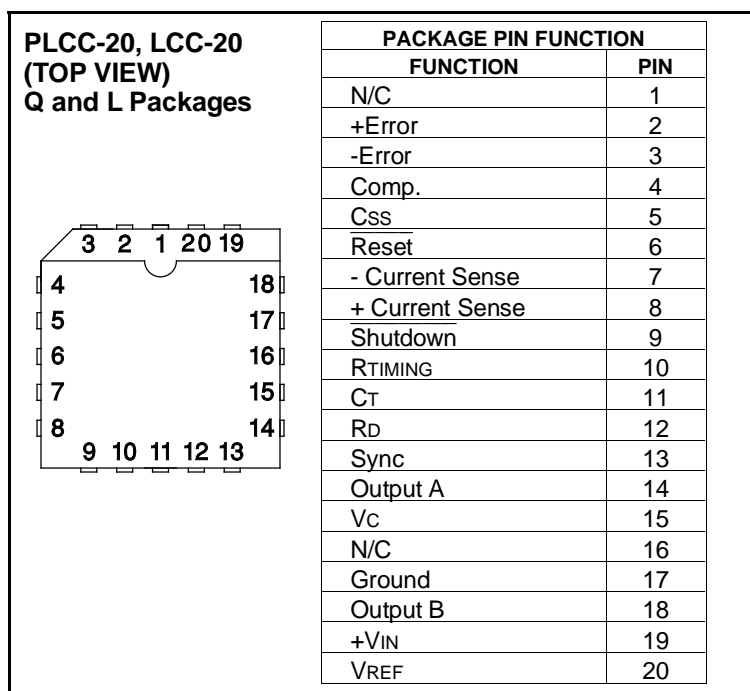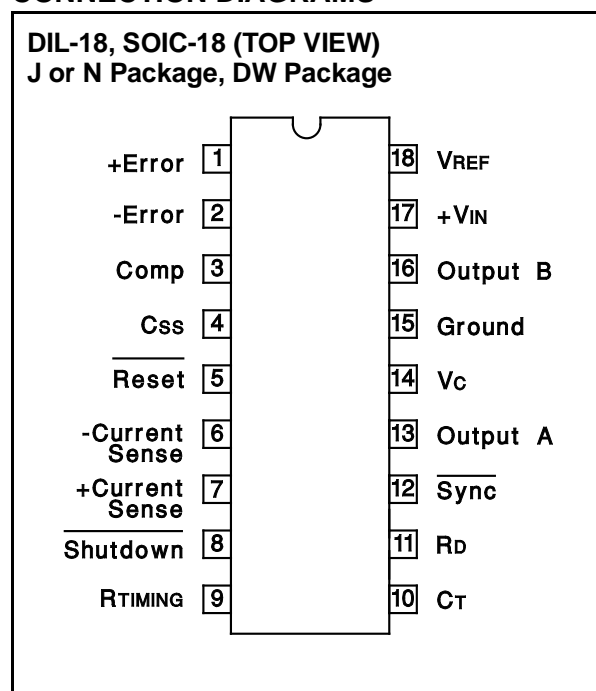Oscillator Timing Capacitor . . . . 1nF to 20µF
Available Deadtime Range at 40kHz . . . . 3% to 50%
Operating Ambient Temperature Range
　UC1526 . . . . -55°C to +125°C
　UC2526 . . . . -25°C to +85°C
　UC3526 . . . . -0°C to +70°C
Note 3: Range over which the device is functional and
parameter limits are guaranteed.

CONNECTION DIAGRAMS

DIL-18, SOIC-18 (TOP VIEW)
J or N Package, DW Package

Pin	Function		Pin	Function
1	+Error		18	V$_{REF}$
2	-Error		17	+V$_{IN}$
3	Comp		16	Output B
4	Css		15	Ground
5	$\overline{Reset}$		14	V$_C$
6	-Current Sense		13	Output A
7	+Current Sense		12	$\overline{Sync}$
8	$\overline{Shutdown}$		11	R$_D$
9	R$_{TIMING}$		10	C$_T$

PLCC-20, LCC-20
(TOP VIEW)
Q and L Packages

PACKAGE PIN FUNCTION	
FUNCTION	PIN
N/C	1
+Error	2
-Error	3
Comp.	4
C$_{SS}$	5
$\overline{Reset}$	6
- Current Sense	7
+ Current Sense	8
$\overline{Shutdown}$	9
R$_{TIMING}$	10
C$_T$	11
R$_D$	12
$\overline{Sync}$	13
Output A	14
V$_C$	15
N/C	16
Ground	17
Output B	18
+V$_{IN}$	19
V$_{REF}$	20

ELECTRICAL CHARACTERISTICS: +V$_{IN}$ = 15V, and over operating ambient temperature, unless otherwise specified, T$_A$ = T$_J$.

PARAMETER	TEST CONDITIONS	UC1526 / UC2526			UC3526			UNITS
		MIN	TYP	MAX	MIN	TYP	MAX	
Reference Section (Note 4)								
Output Voltage	T$_J$ = + 25°C	4.95	5.00	5.05	4.90	5.00	5.10	V
Line Regulation	+V$_{IN}$ = 8 to 35V		10	20		10	30	mV
Load Regulation	I$_L$ = 0 to 20mA		10	30		10	50	mV
Temperature Stability	Over Operating T$_J$		15	50		15	50	mV
Total Output Voltage Range	Over Recommended Operating Conditions	4.90	5.00	5.10	4.85	5.00	5.15	V
Short Circuit Current	V$_{REF}$ = 0V	25	50	100	25	50	100	mA
Under -Voltage Lockout								
$\overline{RESET}$ Output Voltage	V$_{REF}$ = 3.8V		0.2	0.4		0.2	0.4	V
	V$_{REF}$ = 4.8V	2.4	4.8		2.4	4.8		V

Note 4: I$_L$ = 0mA.

2

muRata Ps
Murata Power Solutions

FEATURES

- RoHS compliant
- Radial format
- -40°C to 85°C operating temperature
- Up to 13A I$_{DC}$
- 10µH to 22mH
- Low DC resistance
- Fully tinned leads
- PCB mounting hole
- Low temperature dependence
- Backward compatible with Sn/Pb soldering systems
- Custom parts available

DESCRIPTION

The 1400 Series is suitable for many power supply and other general purpose filtering applications. The use of a non-magnetic screw will ensure mechanical stability.

SELECTION GUIDE

Order Code	Inductance, (1kHz, 0.1V$_{AC}$) ±10% µH	DC Current[1] Max. A	DC Resistance Max. Ω	Q at f kHz Nom. Q	Q at f kHz Nom. f	SRF Nom. MHz	Mechanical Dimensions a mm	b mm	c mm	d mm	Øe mm	Footprint f mm	Øg mm
1410313C	10	13	0.007	54	50	20.7	27.0	24.4	14.0	1.30	4.5	23.9	2.6
1415312C	15	12	0.009	42	50	12.7	27.0	24.4	14.0	1.30	4.5	23.9	2.6
1422311C	22	11	0.011	64	100	9.3	27.0	24.4	14.0	1.30	4.5	23.9	2.6
1433393C	33	9.3	0.015	27	50	9.1	27.0	24.4	14.0	1.30	4.5	23.9	2.6
1447383C	47	8.3	0.019	40	100	6.0	27.0	24.4	18.5	1.30	4.5	23.9	2.6
1447385C	47	8.5	0.021	33	100	6.7	26.8	24.4	14.0	1.20	4.5	23.8	2.4
1468362C	68	6.2	0.032	32	100	5.3	26.5	24.4	14.0	1.08	4.5	23.7	2.1
1468373C	68	7.3	0.022	45	100	5.3	27.0	24.4	18.5	1.30	4.5	23.9	2.6
1410454C	100	5.4	0.042	24	100	4.6	26.4	24.4	14.0	1.02	4.5	23.6	2.0
1410460C	100	6.0	0.033	37	100	3.9	26.8	24.4	18.5	1.20	4.5	23.8	2.4
1410478C	100	7.8	0.040	34	50	3.3	32.4	29.8	21.8	1.30	5.1	29.3	2.6
1415440C	150	4.0	0.069	24	50	3.4	26.2	24.4	14.0	0.90	4.5	23.5	1.8
1415449C	150	4.9	0.051	34	50	2.9	26.4	24.4	18.5	1.02	4.5	23.6	2.0
1415465C	150	6.5	0.042	46	100	2.4	32.2	29.8	21.8	1.20	5.1	29.2	2.4
1422435C	220	3.5	0.096	22	50	2.8	26.1	24.4	14.0	0.85	4.5	23.5	1.7
1422441C	220	4.1	0.073	33	100	2.3	26.3	24.4	18.5	0.97	4.5	23.6	1.9
1422455C	220	5.5	0.062	30	50	2.2	32.1	29.8	21.8	1.14	5.1	29.1	2.2
1430430C	300	3.0	0.140	26	50	2.6	25.9	24.4	14.0	0.75	4.5	23.4	1.5
1430433C	300	3.3	0.100	37	50	2.2	26.2	24.4	18.5	0.90	4.5	23.5	1.8
1430450C	300	5.0	0.080	28	50	1.7	31.8	29.8	21.8	1.02	5.1	29.0	2.0
1433428C	330	2.8	0.150	22	50	2.5	25.9	24.4	14.0	0.76	4.5	23.4	1.5
1433433C	330	3.3	0.107	29	50	2.0	26.2	24.4	18.5	0.90	4.5	23.5	1.8
1433445C	330	4.5	0.091	25	50	1.6	31.8	29.8	21.8	1.02	5.1	29.0	2.0
1447423C	470	2.3	0.222	34	50	2.0	25.7	24.4	14.0	0.67	4.5	23.3	1.3
1447427C	470	2.7	0.149	25	50	1.6	26.1	24.4	18.5	0.85	4.5	23.5	1.7
1447440C	470	4.0	0.125	24	50	1.4	31.7	29.8	21.8	0.97	5.1	29.0	1.9
1468420C	680	2.0	0.276	23	50	1.6	25.7	24.4	14.0	0.67	4.5	23.3	1.3
1468422C	680	2.2	0.226	28	50	1.3	25.9	24.4	18.5	0.75	4.5	23.4	1.5
1468431C	680	3.1	0.173	60	10	1.0	31.6	29.8	21.8	0.90	5.1	28.9	1.8
1410516C	1.0mH	1.6	0.419	30	50	1.4	25.6	24.4	14.0	0.60	4.5	23.2	1.2
1410517C	1.0mH	1.7	0.336	35	50	1.2	25.7	24.4	18.5	0.67	4.5	23.3	1.3
1410524C	1.0mH	2.4	0.277	33	50	1.0	31.4	29.8	21.8	0.79	5.1	28.8	1.5
1415513C	1.5mH	1.3	0.630	34	50	1.0	25.5	24.4	14.0	0.54	4.5	23.1	1.0
1415514C	1.5mH	1.4	0.518	47	50	0.8	25.6	24.4	18.5	0.60	4.5	23.2	1.2
1415517C	1.5mH	1.7	0.374	28	50	0.7	31.3	29.8	21.8	0.75	5.1	28.8	1.5
1422509C	2.2mH	0.9	0.916	43	50	0.9	25.3	24.4	14.0	0.48	4.5	23.1	0.9
1422512C	2.2mH	1.2	0.649	33	50	0.7	25.6	24.4	18.5	0.60	4.5	23.2	1.2
1422514C	2.2mH	1.4	0.622	33	50	0.6	31.1	29.8	21.8	0.67	5.1	28.7	1.3
1433507C	3.3mH	0.7	1.428	45	50	0.8	25.2	24.4	14.0	0.43	4.5	23.0	0.8
1433510C	3.3mH	1.0	1.992	20	50	0.7	25.5	24.4	18.5	0.54	4.5	23.1	1.0
1433512C	3.3mH	1.2	0.861	20	50	0.5	31.0	29.8	21.8	0.60	5.1	28.6	1.2
1447506C	4.7mH	0.6	2.200	60	50	0.6	25.2	24.4	14.0	0.39	4.5	23.0	0.7
1447508C	4.7mH	0.8	1.436	65	50	0.5	25.3	24.4	18.5	0.48	4.5	23.1	0.9
1447509C	4.7mH	0.9	1.250	57	10	0.5	30.9	29.8	21.8	0.54	5.1	28.5	1.0
1468505C	6.8mH	0.5	2.810	50	50	0.5	25.2	24.4	14.0	0.39	4.5	23.0	0.7
1468507C	6.8mH	0.7	2.214	47	50	0.4	25.2	24.4	18.5	0.43	4.5	23.0	0.8
1468508C	6.8mH	0.8	1.884	30	50	0.4	30.7	29.8	21.8	0.48	5.1	28.5	0.9
1410604C	10mH	0.4	4.340	51	50	0.4	25.1	24.4	14.0	0.34	4.5	22.9	0.6
1410605C	10mH	0.5	3.394	48	50	0.3	25.2	24.4	18.5	0.39	4.5	23.0	0.7
1410606C	10mH	0.6	2.294	48	50	0.2	30.9	29.8	21.8	0.54	5.1	28.5	1.0
1415604C	15mH	0.4	4.912	61	10	0.2	25.1	24.4	18.5	0.34	4.5	22.9	0.6
1415605C	15mH	0.5	3.740	55	10	0.2	30.6	29.8	21.8	0.43	5.1	28.4	0.8
1422604C	22mH	0.4	6.962	30	50	0.2	30.5	29.8	21.8	0.34	5.1	28.3	0.6

1 Maximum DC current occurs when either the inductance falls to 60% of its nominal value or when its temperature rise reaches 50°C, whichever is sooner.

SOLDERING INFORMATION[2]

Peak wave solder temperature	300°C for 10 seconds
Pin finish	Pure tin dip

ABSOLUTE MAXIMUM RATINGS

Operating free air temperature range	-40°C to 85°C
Storage temperature range	-55°C to 125°C

TYPICAL CORE/WIRE CHARACTERISTICS

Inductance Temperature Coefficient	Resistance Temperature Coefficient	Curie Temperature (T_C)	Saturation Flux (B_{SAT})
215ppm	3900ppm	130°C	240mT

All specifications typical at T_A=25°C
2   For further information, please visit www.murata-ps.com/rohs
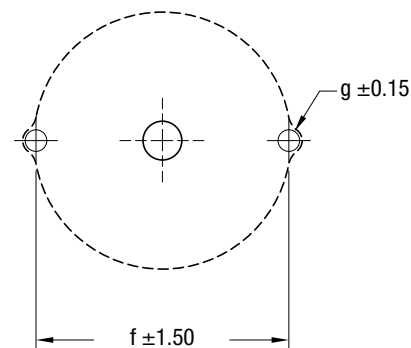
PACKAGE SPECIFICATIONS

MECHANICAL DIMENSIONS

1422455C
XYYWW
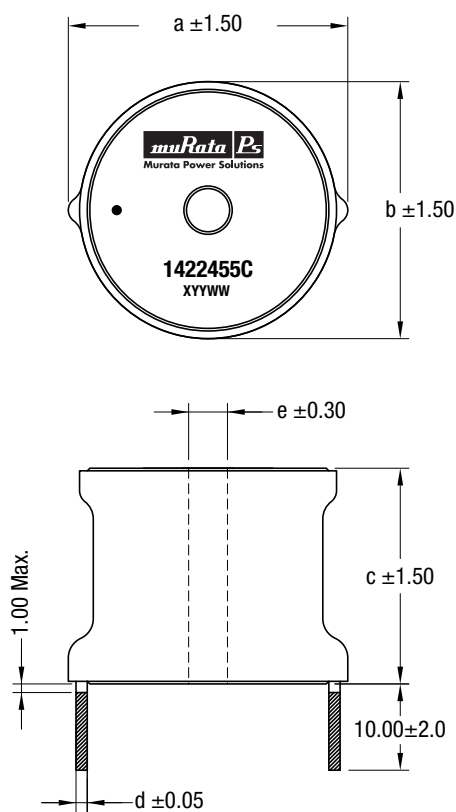
All dimensions in mm.
Package weight: 30-65g Typ.
Marking indicates start of winding.

RECOMMENDED FOOTPRINT DETAILS

All dimensions in mm

USA:	Mansfield (MA), Tel: (800) 233 2765, email: sales@murata-ps.com
Canada:	Toronto, Tel: (866) 740 1232, email: toronto@murata-ps.com
UK:	Milton Keynes, Tel: +44 (0)1908 615232, email: mk@murata-ps.com
France:	Montigny Le Bretonneux, Tel: +33 (0)1 34 60 01 01, email: france@murata-ps.com
Germany:	München, Tel: +49 (0)89-544334-0, email: ped.munich@murata-ps.com
Japan:	Tokyo, Tel: 3-3779-1031, email: sales_tokyo@murata-ps.com Osaka, Tel: 6-6354-2025, email: sales_osaka@murata-ps.com **Website: www.murata-ps.jp**
China:	Shanghai, Tel: +86 215 027 3678, email: shanghai@murata-ps.com Guangzhou, Tel: +86 208 221 8066, email: guangzhou@murata-ps.com